University of Alberta
Department of Civil &
Environmental Engineering

Structural Engineering Report No. 228

CYCLIC BEHAVIOR OF MASONRY WALLS WITH GFRP

by
Marc D. Kuzik
Alaa E. Elwi
and
J.J. Roger Cheng

August, 1999

OUT-OF-PLANE CYCLIC BEHAVIOR OF MASONRY WALLS REINFORCED EXTERNALLY WITH GFRP

by

Marc D. Kuzik

Alaa E. Elwi

and

J.J. Roger Cheng

Structural Engineering Report 228

Department of Civil and Environmental Engineering
University of Alberta
Edmonton, Alberta, Canada

August, 1999

ABSTRACT

The research work reported here investigates the out-of-plane cyclic behavior of masonry walls reinforced externally with GFRP. A full-scale testing program consisting of eight wall specimens was conducted. Nine tests were performed in which three parameters were studied: level of compressive axial load, amount of internal steel reinforcement, and amount of externally bonded GFRP.

The hysteretic behavior was analyzed and discussed both qualitatively and quantitatively. An analytical model was proposed to predict the bending moment versus centerline deflection hysteretic response incorporating a stiffness degradation model. This mechanistic model includes the parameters of axial load, masonry properties, steel reinforcement properties, and GFRP properties in addition to considering the limits of bond and development between the GFRP and masonry. Finally, a comparison between the predicted and actual hysteresis envelopes was performed.

The GFRP reinforced masonry walls were highly successful under flexural loads. The tests showed stable, predictable behavior with highly enhanced strength and stiffness. The system also remarkably maintained its integrity under repetitive high stress fully reversed cycles of load and large flexural deformations. Therefore, the system could be advantageously used to rehabilitate older masonry structures that are inadequately reinforced to withstand seismic events.

ACKNOWLEDGEMENTS

Financial support for the research was provided by the Canadian Masonry Research Institute (CMRI) and the Network of Intelligent Sensing for Innovative Structures (ISIS). The authors also acknowledge the donation of the concrete masonry units from EDCON, mortar from IXL, and grout from MANSTAR Distributors, all located in Edmonton, Alberta.

The first author wishes to acknowledge personal financial support in the form of scholarships from the Natural Sciences and Engineering Research Council of Canada (NSERC) and the University of Alberta.

TABLE OF CONTENTS

LIST OF TABLES

LIST OF FIGURES

Figure **Page**

List of Abbreviations and Symbols

Abbreviations

ASTM	American Society for Testing and Materials
ATC	Applied Technology Council
CFRP	Carbon Fibre Reinforced Polymer
CSA	Canadian Standards Association
GFRP	Glass Fibre Reinforced Polymer
gpm	Gallon per minute
HAM	Hydraulic Accessory Module
HSS	Hollow Structural Section
kip	one thousand pounds
kN	kiloNewton
ksi	kips per square inch
L	Litre
LVDT	Linear Variable Differential Transformer
m	meter
min	minute
mm	millimeter
MPa	MegaPascal
MTS	Material Testing System
N	Newton
psig	pounds per square inch gauge
UBC	Uniform Building Code
W	Wide Flange Beam Designation
WWF	Welded Wide Flange Beam Designation

Symbols

A_e = effective area of uncracked masonry cross-section, (mm^2)

A_{GFRP} = area of GFRP on the tension face, (mm^2)

A_s = area of tension steel reinforcement, (mm^2)

a = depth of the equivalent rectangular stress block, (mm)

b = width of the compression zone, (mm)

d = distance from the extreme compression fibre to the centroid of the tension steel, (mm)

E = modulus of elasticity, (MPa)

E_{GFRP} = modulus of elasticity of the GFRP, (MPa)

E_m = modulus of elasticity of masonry, (MPa)

E_s = modulus of elasticity of the reinforcing steel, (MPa)

f'_c = compressive strength of concrete, (MPa)

f'_m = compressive strength of masonry, (MPa)

f_y = yield strength of the steel reinforcement, (MPa)

f_t = tensile masonry strength, (MPa)

h = depth of the wall, (mm)

I = moment of inertia, (mm^4)

I_{cr} = cracked moment of inertia, (mm^4)

I_g^f = modified moment of inertia calculated with one face shell only, (mm^4)

I_o = moment of inertia of the uncracked section about its centroidal axis, (mm^4)

k = constant used to calculate compressive strength of concrete

k_1 = factor used to approximate the depth of the compressive stress block

k_2 = factor used to locate the centroid of the compressive stress block

k_3 = factor used to approximate the height of the compressive stress block

L = wall height, (mm)

L = length, (mm)

M = bending moment, (Nmm)

M_a = current level of bending moment, (Nmm)

M_{cr} = cracking moment, (Nmm)

M_{cr}^f = modified cracking moment, (Nmm)

M_f = factored moment, (Nmm)

Mn = nominal moment, (Nmm)

M_T = transition moment, (Nmm)

M_u = ultimate moment, (Nmm)

P = compressive axial load, (N)

P = tensile axial load, (N)

R = stiffness interpolation factor

R^2 = coefficient of determination in regression analysis

S = section modulus, (mm^3)

S_{cr} = spacing of horizontal cracks, (mm)

t_{GFRP} = nominal GFRP thickness, (mm)

V_f = factored shear force, (N)

V_r = shear force resistance, (N)

x = length of shear span, (mm)

y_t = distance from the centroid to the extreme fibre, (mm)

α = reduction factor

β_1 = factor used to approximate k_1

Δ_a = wall centerline deflection at service moment M_a, (mm)

Δ_{cr} = wall centerline deflection at the cracking moment, (mm)

Δ_{cr}^{f} = wall centerline deflection at the transition moment, (mm)

Δ_{MAX} = maximum centerline deflection, (mm)

Δ_T = centerline deflection at the transition moment, (mm)

Δ_u = centerline deflection at the ultimate moment, (mm)

δ = change in length, (mm)

$\varepsilon_{u\,GFRP}$ = maximum GFRP strain at the ultimate moment, (mm/mm)

θ = angle, (radians)

ϕ_s = resistance factor for reinforcing bars, typically 0.85

ϕ_m = resistance factor for masonry, typically 0.55

ρ = curvature, (1/mm)

ρ_T = GFRP reinforcement ratio

σ_u = ultimate tensile strength

σ_y = yield strength

1. INTRODUCTION

1.1 Foreword

As one of the oldest building materials, many structures throughout the world have been constructed either partially or entirely of various types of masonry. Early masonry structures were constructed using simple rules of thumb which resulted in overly conservative estimates of structural capacity. Throughout the twentieth century, both economic factors and increased understanding of the mechanics of masonry led to less conservative designs by reducing the amount of material used. Today, load bearing – free standing walls of high slenderness ratios are common place. Many older masonry walls were designed with little or no vertical steel reinforcement, thus relying on each structural element to remain in compression under the combined effects of axial, flexural, and shear forces. This design philosophy is still employed today; however, it is inadequate in regions of high seismicity.

1.2 Statement of the Problem

Many older masonry structures located in zones of high seismicity would perform poorly or perhaps even fail during a substantial earthquake. At equal risk are non-masonry structures which use unreinforced or lightly reinforced masonry for in-fill and partition walls. These components perform well under service loads but may fail catastrophically due to inertial forces generated during a seismic event.

In recent years, many techniques have been proposed to strengthen existing masonry structures to withstand seismic loading. However, most of the proposed techniques prove to be excessively disruptive to the use and occupancy or too cost prohibitive for practical application. An attractive approach is to strengthen structural members with externally bonded Fibre Reinforced Polymers (FRP). Extensive work of this type has been studied for reinforced concrete beams and columns with much success. However, little similar research has been performed on concrete and/or masonry wall systems. To validate this retrofitting technique, an understanding of the internal mechanics of the composite wall system and the response of the system to cyclic loading is required.

1.3 Motivation for the Research

The work reported in this thesis was performed as the second phase in a research program at the University of Alberta investigating the application of FRP to masonry walls. Promising results were obtained in the initial work by Albert *et al.* (1998) who performed out-of-plane monotonic tests on twelve masonry block walls reinforced externally with various types of FRP in different layout schemes. The types of FRP included: Glass Sheet (SEH 51 fabric with TYFO S epoxy supplied by FYFE LLC Co.), Carbon Strap (CarboDur carbon strips with Type S epoxy supplied by Sika Canada Inc.), and Carbon Sheets (Replark 20 carbon pre-impregnated sheets supplied by Mitsubishi Chemicals). Albert *et al.* (1998) identified a bilinear load versus deflection response where the initial slope was a function of the properties of both the masonry and FRP whereas the second slope was dominated by the FRP properties. In addition, both the type and amount of FRP used determined the stiffness of the second slope; however, the general behavior between each type of FRP was the same. Albert *et al.* (1998) also identified three failure modes: mortar debonding or sliding shear, flexure-shear, and rupture of the fibre reinforcement. An analytical model for predicting the load versus deflection response was proposed but was highly simplistic. The model did not account for each parameter individually resulting in varying accuracy between each predicted response.

By identifying significant strength and ductility gains in walls retrofit with FRP, a promising alternative to conventional rehabilitation methods was established. In assessing the general behavior, Albert *et al.* (1998) identified the important parameters and thus formed the basis from which to continue research in this area.

1.4 Objective and Scope

Albert *et al.* (1998) concluded that the behavior of masonry walls externally reinforced with different types of FRP was more or less identical. Carbon fibre plates and carbon fibre sheets are considerably more expensive than glass fibre sheets.

Therefore, this work is primarily focussed on Glass Fibre Reinforced Polymers (GFRP) reinforced masonry walls.

The objective of the research reported in this manuscript was to study the out-of-plane hysteretic response of masonry walls with externally bonded GFRP under fully reversed cyclic loading. The scope of the research involved the testing and analysis of eight concrete block masonry wall specimens. A self-equilibrating load frame was built to allow fully reversed, out-of-plane lateral loading in addition to compressive axial loading. Various combinations of internal steel reinforcement, externally bonded GFRP, and level of axial load were used to define the test matrix. This resulted in the execution of nine tests to study all the parameters.

1.5 Organization of the Thesis

Chapter 2 presents an overview of the relevant research performed to date on members reinforced with FRP to improve flexural performance.

Chapter 3 is divided into two major sections. First, the testing program is described in detail. This includes a description of the test specimens, load frame, instrumentation, and testing procedures. The second area of discussion focuses on the observations during testing which includes figures presenting the significant raw data.

In Chapter 4, a qualitative discussion is presented on the general behavior of the bending moment versus deflection hysteretic response. Here, the response is segmented into different regions and described in detail.

A quantitative analysis and analytical model are presented in Chapter 5. A rational mechanics approach is used to successfully describe both the strength and stiffness behavior. In addition, a comparison between the analytically predicted and actual testing hysteretic response is presented.

Finally, in Chapter 6, a summary and conclusions of the research are given. In addition, some recommendations for further research on this topic are discussed.

2. LITERATURE SURVEY

2.1 Introduction

Fibre reinforced polymers (FRPs) were introduced into the fields of aerospace and mechanical engineering in the 1940's. By the late 1970's, the use of composites had expanded to include applications in the automotive, sporting goods, and biomedical industries. Not until about 1985, did researchers in structural engineering begin to investigate the application of FRPs to strengthen existing structures. Neale (1999) provides an extensive survey of recent work in structural rehabilitation.

Ladner and Weder (1981) were among the first researchers to investigate the post-strengthening of existing concrete structures by bonding steel plates to the tension face of reinforced concrete girders. Although successful at increasing both flexural strength and ductility, the two major disadvantages of using heavy steel plates were the difficulty of handling in the field and corrosion. These problems prompted Meier (1987) and Kaiser (1989) to begin a research program at the EMPA in Dübendorf, Switzerland, in 1985 entitled "Strengthening of reinforced concrete with carbon fiber reinforced epoxy resins." The goal of this research was to see if a high strength, light weight material such as carbon fibre could replace the steel plates. Meier and Kaiser (1991) performed a simple economic comparison between the steel plate versus carbon fibre reinforced polymers (CFRPs) post-strengthening techniques. The CFRP material costs roughly ten times more than steel but the weight is reduced to one-twentieth of the required steel weight. Considering that material costs are only about 20% versus labour costs of about 80% for this type of work, the overall cost is comparable for both systems. However, the advantages of using FRPs over steel, besides the high strength to weight ratio, include: outstanding corrosion resistance, excellent fatigue properties, very high axial stiffness, and light weight for easy on-site application.

2.2 Flexural Behavior in Concrete

Much of the research done on post-strengthening of structures with FRPs has been focused on reinforced concrete applications. The early work by Meier and Kaiser (1991) investigated the use of externally bonded carbon fibre plates to the tension face of reinforced concrete beams as a means of increasing the flexural capacity. Twenty-six beams were constructed. Each had a span of 2 m and a cross section of 150 mm deep by 250 mm wide. The results from two specimens were compared, one reinforced with a 0.3 mm thick by 200 mm wide carbon fibre sheet and one with no externally applied fibre. The post-strengthened beam carried twice the ultimate load with one-half of the centerline deflection of the beam with no fibre. In addition, four failure mechanisms were identified with two being classified as brittle modes. One of these modes was the sudden peel off of the CFRP during loading due to the development of shear cracks. Of more importance for the purposes of the current study, Meyer and Kaiser (1991) observed a tri-linear load versus centerline deflection relationship.

Saadatmanesh and Ehsani (1991a) studied the effect of varying the amount of flexural steel reinforcement in five rectangular concrete beam specimens having cross sections of 455 mm deep by 205 mm wide and a clear span of 4.57 m. All the specimens were fit with GFRP plates measuring 152 mm wide by 6 mm thick bonded along the entire length. The results showed that beams with lower steel reinforcing ratios had a more significant increase in ultimate flexural capacity than those with higher ratios. Reduced crack size was also observed at all levels of load due to the plating. In addition to the experimental study, Saadatmanesh and Ehsani (1991b) performed the analysis and parametric study. The analysis presented is based on strain compatibility and balancing the forces within the cross section. Good analytical and experimental agreement was found when the epoxy was able to transfer the forces into the bonded plate.

Since the early work, several papers have been written on the post-strengthening of reinforced concrete beams with FRPs, many of which are repetitive and lack good analytical content. Recently, the research focus has shifted towards developing analytical and numerical models which describe the behavior up to the ultimate load. Chaallal *et al.* (1998) proposed design equations for both flexure and shear strengthening using FRPs

based on the CSA A23.3-94 concrete code. The design procedure for flexure addresses issues such as failure type and interfacial stresses between the concrete and FRP. In addition, a flow chart is provided to guide designers through the procedure. Chaallal *et al.* (1998) based the FRP dimensions in their flexural design on results obtained by Sharif *et al.* (1994) to ensure a ductile failure mode. Insight in controlling the failure modes is provided by Sharif *et al.* (1994). Results from testing ten reinforced concrete beams showed that the thickness of the bonded FRP had an impact on the ductility. As the thickness of the bonded FRP increased, the ductility of the beam decreased.

Recently, some researchers have targeted the application of FRPs to pre-cracked concrete beams. One of the findings of Sharif *et al.* (1994) was that sufficient ductility was provided by repairing damaged reinforced concrete beams with FRPs. Buyukozturk and Hearing (1998) outline the need for further research into the various failure mechanisms of pre-cracked beams repaired with FRPs. Their review of current work shows that the performance of retrofit systems is still not completely understood. Buyukozturk and Hearing (1998) believe that although the flexural strength is increased, the failure mechanism of the pre-cracked systems may become more brittle. Buyukozturk and Hearing (1998) also suggest that future topics of study should include material compatibility and degradation due both to environmental and cyclic loads.

2.3 Masonry Retrofit with FRP

The use of FRPs to post-strengthen masonry structures is beginning to gain acceptance in the engineering community. Much of the research done in retrofitting reinforced concrete elements has formed the basis for beginning research in masonry structures. Although concrete and masonry materials are similar in certain aspects, the behavior of structures built of either material differs in substantive ways. This is due in part to the different placement location and typical ratio of steel reinforcement. Typically, older masonry structures are very lightly reinforced — if at all. More importantly, masonry structures have well defined joint patterns that provide readily available failure planes.

Ehsani *et al.* (1993) were the first group to study the flexural behavior of masonry walls strengthened with FRPs. Six masonry beams were each constructed from 19 burned clay bricks in stack bond. FRP was bonded to the tension face of the beams and the load was applied at two points to create a region of zero shear. The parameters studied were the type of epoxy (two types), type of mortar (S and W), type of fabric (fibreglass and unidirectional E-Glass), surface finish, and brick age. The results (Ehsani, 1995) showed a dramatic increase in both flexural capacity and ductility. Considering an unreinforced specimen would fail under its own self weight, some FRP reinforced beams carried more than 20 times their own self weight and were able to accommodate deflections in excess of $1/50^{th}$ of the span. Another important observation was that the fibre strength controlled the mode of failure. For specimens retrofitted with weaker fibre, failure occurred by the rupturing of the fibre. Where stronger fibre was used to retrofit the specimens, failure occurred as a result of the masonry crushing. A more in depth discussion of this work (Ehsani and Saadatmanesh, 1996) also included the post-strengthening of unreinforced masonry for shear in addition to some field applications.

Probably the first research conducted on shear strengthening was performed by Schwegler (1994) on large-scale shear walls. These walls were constructed from concrete masonry units and two reinforcement strategies were used to strengthen them. First, CFRP sheets were bonded diagonally and anchored to the adjoining floor and ceiling. Second, a conventional polyester woven fabric was applied to the entire surface but not anchored to the floor or ceiling. The walls were then loaded in-plane through fully reversed cycles. The walls strengthened with the CFRP sheets and alternatively with woven polyester fabric exhibited an increase in earthquake resistance by a factor of 4.3 and 1.4 respectively. However, fibre debonding and a highly non uniform crack distribution were observed; and thus, a recommendation that a more elastic epoxy should be sought was stated.

Seible (1995) conducted full-scale, in-plane re-tests on a five storey reinforced masonry building retrofit with CFRP. The structure was subjected to a pseudo-dynamic lateral load until ultimate failure was reached. Results showed that the inelastic deformation capacity was doubled and that the shear deformations were reduced to half of the original values obtained from the building when tested with no CFRP. Seible

(1995) also commented on the key design aspects for out-of-plane retrofitting: first, "the development [of force transfer] of the overlay material [to the masonry] in regions of high moment gradients," and second, "the potential for buckling and delamination of the thin and stiff overlays on the compression side of the flexural member."

Triantafillou (1998) tested six clay brick masonry walls externally reinforced with unidirectional CFRP laminates in the out-of-plane direction. The walls had a cross section of 400 mm wide by 120 mm thick and a clear span of 780 mm. The CFRP was bonded on one side only and the loading was monotonic. The mid-span load versus deflection response obtained was linear almost to the point of failure. All the failures were caused by crushing of the bricks which had a compressive strength of 3 MPa. The ultimate mid-span deflections were in the order of L/150. Also presented are some guidelines for limiting the FRP ratio to ensure a flexure failure occurs.

The most comprehensive, to date, full-scale out-of-plane flexural test program on unreinforced masonry walls fitted external FRPs was performed by Albert *et al.* (1998) in the I.F. Morrison Structural Engineering Laboratory at the University of Alberta. A total of ten 4.0 m tall walls were constructed, six with 8 inch standard concrete blocks and four with 200 mm standard concrete blocks. A brief description of the parameters studied is discussed in the introductory chapter of this document. Results from this testing program showed a substantial increase in both the out-of-plane moment capacity and ultimate mid-span deflection as compared to a wall with no externally applied FRP.

A slightly different external reinforcing system incorporating carbon fibre was performed by Kolsch (1998). A carbon fibre cement matrix (CFCM) overlay system was applied to the entire face of several sand-lime brick walls measuring either 3 m by 3 m by 0.24 m (l by w by t) or 2 m by 2 m by 0.24 m (l by w by t). The load was cycled monotonically using an air bag on one side of the wall. The load versus mid-height deflection hysteresis presented, shows a tri-linear behavior with very little stiffness degradation between successive loading cycles. In addition, the wall systems were typically able to withstand lateral loads equivalent to the inertial forces generated from 3g (gravity) acceleration.

Bonding of CFRP to natural stone was investigated by Kurtis and Dharan (1997). Flexural tests were performed on marble and limestone panels using a three point loading

scheme. A ten fold increase in flexural capacity of specimens reinforced with CFRP was observed. All the specimens exhibited a linear load versus mid-span deflection relationship until failure.

2.4 Composite-to-Concrete Bond

The behavior in the interface region between the FRP and cementicious materials is not fully understood. It is typically difficult to develop the complete composite action between the FRPs and the concrete due to premature failures such as peel-off initiated by shear cracking. To predict the out-of-plane flexural response of walls strengthened with external FRPs, a clear understanding of the force transfer mechanics through the bond interface must be defined.

To the authors' knowledge, the first testing of bond between composite materials and concrete was performed by Chajes *et al.* (1996). This highly significant work employed a single-lap shear test specimen to study both bond strength and force transfer. Six-ply unidirectional pre-impregnated graphite fibres having a total thickness of 1.016 mm (0.040 in.) were bonded to concrete blocks. A constant bond length was used for all the specimens so the parameters of concrete surface preparation, type of adhesive, and effects of concrete strengths could be studied. For all but a few specimens, the failure mechanism was shearing of the concrete directly beneath the bonded surface. Three surface preparations were tested: as-formed surfaces, surfaces ground with a stone wheel, and surfaces mechanically abraded with a wire wheel. The second and third surface preparation methods showed, respectively, a 3 % and 10 % increase in ultimate shear strength over the first. For the four different epoxy types tested, no significant difference in average bond shear stress at failure was observed. A linear correlation between increased concrete strength and increased bond strength was observed. Also noted was that the concrete quality at the bond surface may not be indicative of that throughout the structure. To assess the load transfer, the bonded length was varied and a series of strain gauges were placed along the bonded length. Plots of the strain profiles along the bonded length for increasing load levels showed a relatively linear decrease in

strain from high values at the free edge to low values at distances of about 75 mm (3 in.) from the free edge.

Bizindavyi and Neale (1999) recently concluded an experimental and analytical program focussed on the transfer mechanisms between concrete and bonded composite laminates. Two types of composites were used: TYFO® SEH 51 glass fabric with TYFO® S epoxy resin, and REPLARK™ unidirectional carbon sheet with L 700S epotherm resin.* The fibres were bonded to 150x150x400 mm normal density concrete blocks and tested in direct shear by a specially built loading device. Preliminary test results revealed that the width of the bonded laminate had little effect on the strain distribution along the bonded length; and thus, only a 25.4 mm width was used for the remainder of the testing. The results of the strain profiles along the bonded lengths show three distinct trends depending entirely on level of load. First, when the load was initially applied, the strains decreased exponentially from high values at the edge to zero within a short distance. This distance is referred to as the initial transfer length. Upon further loading, a crack perpendicular to the direction of loading appeared within the initial transfer length causing the transfer region to propagate towards the unloaded end. At this stage, the strain profile obtained along the bonded length showed a well defined decreasing bilinear slope with a kink appearing around the crack location. In the final stages of loading before failure, the strain profile became entirely linear, decreasing from the loaded edge to the unloaded edge. Finally, both empirical equations derived from the data and theoretical equations based on shear lag theory are presented for the transfer lengths.

2.5 Load-Deflection Behavior

Masonry wall systems are typically composed of masonry units, mortar, reinforcing steel (both horizontal and vertical), and grout. This combination of materials creates a system which is anisotropic and typically behaves with a nonlinear response to out-of-plane flexure. Various models for lateral load displacement relationships have been

* The TYFO® brand of GFRP was the same composite used by the author and discussed within this document in the following chapters.

proposed for masonry structures (Bernardidi *et al.*, 1984; Tassios, 1984; Wakabayashi and Nakamura, 1984). For reinforced masonry walls, Hamid *et al.* (1989) and Abboud *et al.* (1996) showed typical load versus deflection response for out-of-plane monotonic loading. These responses typically consisted of four regions. Starting at the origin, the response was linear with a positive slope until the point of first cracking. At this point, the stiffness reduced, then continued to be more or less constant. The slope of the response gradually decreased to zero, the point of maximum load, and continued to decrease as the deformations increased and the load decreased. Results showed that the transition points of the various regions were affected by different parameters. The initial cracking moment and wall ductility were largely affected by the extent of grouting. Increased grouting resulted in a higher cracking moment and improved ductility. An increased percentage of vertical steel reinforcement affected the ultimate load capacity, the shape of the load versus deflection response, and the displacement ductility ratio.

A unique scheme to model hysteresis envelopes for masonry block walls, by obtaining data from a monotonic in-plane lateral load versus deflection envelope, was studied by Tomaževič and Lutman (1996). A fictitious input energy approach was considered to correlate the monotonic and cyclic hysteresis envelopes based on the test data from 32 masonry block wall specimens. The fundamental response was a symmetric, trilinear hysteresis envelope. Three critical points were defined: first cracking, maximum lateral load resistance, and the ultimate failure or limit state. Degradation of stiffness was incorporated on the unloading branch after the point of maximum lateral resistance was reached. Strength degradation was based on the dissipated hysteretic energy and degradation of stiffness at each lateral load reversal.

Hamid *et al.* (1990) conducted fully reversed cyclic testing on six, 6 inch masonry block walls. Each wall was three blocks wide and thirteen courses high laid in running bond. The parameters studied were the percentage of vertical reinforcing steel and staggered versus centered placement of the reinforcement. For the walls with centrally located reinforcement, the shape of the hysteresis loop deviated drastically from the typical parallelogram shape observed in reinforced concrete elements. Beyond the point of first yielding, the unloading branch was parallel to the loading branch until near zero load. At this point, the curve flattened out and shadowed the horizontal axis resulting in a

large narrow region of zero stiffness. The walls with staggered reinforcement did not exhibit this pinching effect. Rather, the typical parallelogram shaped hysteresis envelope was observed and thus the area under the hysteresis loops was greater than that obtained from specimens with centered reinforcement. It was also noted that the walls behaved in a very stable manner for the load paths within each cycle group loaded and unloaded along similar paths. In addition, the slope of the hysteresis was found to be a function of the cracked section.

One cyclic test was performed by Albert *et al.* (1998) in which the wall specimen, reinforced with external GFRP, was successively loaded and unloaded in the same quadrant of the load versus deflection hysteresis. The resulting shape of the hysteresis envelope defined a new type of behavior. The shape of the envelope is bilinear in the loading region and linear in the unloading region with no degradation in strength until failure. The same behavior was observed by the author and is explained in detail in chapter 5 of this document.

In summary, the use of FRPs as a means of strengthening existing structures has been shown to be effective. However, very limited testing in the field of masonry reinforced with FRPs has been conducted. Thus, continued research is required to observe all the behavior types and perhaps more importantly, to reliably describe and understand the mechanics involved to predict these behavior types.

3. EXPERIMENTAL PROGRAM AND TEST OBSERVATIONS

3.1 Introduction

A full-scale testing program consisting of eight masonry walls reinforced externally with GFRP sheets on both face shells was conducted. Each wall was 4 m tall and 1.2 m wide. The walls were tested in a vertical position under constant compressive axial load and increasing fully reversed cyclic out-of-plane lateral load. The lateral load was applied at two lines: 1200 mm from the top support and 1200 mm from the bottom support. The parameters investigated were: amount of GFRP, amount of steel reinforcement, level of axial load, and the behavior of GFRP under cyclic loading. This chapter describes the material properties, the test specimens, the test setup, and a brief overview of the test results. A full discussion follows in chapter 4.

3.2 Material Properties

In conjunction with the full-scale testing program, a complete set of ancillary material tests was conducted to obtain the mechanical properties of the masonry, steel reinforcement, and the GFRP.

3.2.1 Masonry Prisms

Two series of masonry prisms were constructed in conjunction with the construction of the wall specimens. Five grouted and five ungrouted prisms were built using 200 mm concrete masonry units and type S mortar to determine f'_m. Each prism was five courses high and one standard block wide. Before the prisms were aligned in the testing machine, a 10 mm (3/8 inch) thick piece of fibreboard was placed beneath and on top of each prism. This served as a means to ensure a uniform load transfer between the testing machine platens and the prisms. Testing was performed using a Material Testing System (MTS) 6000 test machine and load data were recorded manually from the MTS display module. The loading rates for both series were performed in accordance

with CAN3-A369.1-M84 (1984). The typical failure mode for the ungrouted prisms was vertical splitting through the webs followed by buckling of the face shells. The typical failure mechanism in the fully grouted prisms was diagonal cracking through the face shell followed by spalling. The masonry prism test results are summarized in Table 3.1.

3.2.2 Steel Reinforcement

Tension tests were performed on both the 10M and 15M reinforcing steel bars. The coupons were tested using an MTS 1000 testing machine. An extensometer was attached to the specimens to measure elongation while the MTS load cell measured the applied load. Table 3.2 contains the following material properties: static yield strength (σ_y), static ultimate tensile strength (σ_u), and the modulus of elasticity (E).

3.2.3 Glass Fibre Reinforced Polymer

In determining the GFRP material properties, the cross-sectional area is required. The width is very easily measured but the thickness is not. Coupons can be made with the same amount of fibre but different amounts of epoxy. Thus, the width of each specimen can be the same but the thickness of each will be different. To eliminate this problem, two methods can be used to standardize results. First, all thickness dimensions can be taken as the manufacturer's nominal reported fibre thickness. This may not give the most accurate results, but all results will be consistent between testing programs. This is similar to the philosophy employed when testing deformed steel reinforcing bars except the variations in the rebar diamters are much smaller than those in the composites. Second, the thickness dimension can simply be ignored. Instead of reporting a modulus of elasticity E, the force per unit width per unit strain, E* is reported. This modified modulus can then be incorporated into a strain compatibility or transformed section model yielding consistent results.

The GFRP used was SEH-51 with Tyfo® S epoxy supplied by FYFE Co. LLC. This glass fibre is sold in 1200 mm wide rolls where the individual fibres are oriented uniaxially in the longitudinal direction with perpendicular cross weaves used to hold the

longitudinal fibres in place. The SEH-51 is not pre-impregnated and is thus very flexible at the time of application. Table 3.3 lists the material properties determined from two GFRP tension coupons made in accordance with ASTM D 3039-95a (1995). Both tension coupon specimens successfully failed within the gauge length. Again, an MTS 1000 testing machine was used to apply the tensile load. Foil strain gauges were bonded to the coupons to provide strain readings and the load was measured through the MTS load cell.

3.3 Test Specimens

3.3.1 Description

Eight masonry wall specimens were constructed by professional masons using 15 MPa, 200 mm standard concrete block and type S mortar. Each wall was 4.0 m (20 courses) tall and 1.2 m (two full blocks and one half block) wide. Horizontal joint reinforcement consisted of #9 gauge ladder type located at every third course. All specimens were built on 1200 mm x 200 mm x 51 mm steel plates for two purposes: to ensure an even load distribution at the bottom support, and to facilitate the attachment of a lifting device.

The primary variables of concern, listed in Table 3.4, were level of axial load, amount of steel reinforcement, and amount of GFRP. After the walls were constructed, seven walls were each fitted with either two 10M or two 15M vertical reinforcing steel bars. One bar was placed in the second core from each side of the wall yielding a spacing of 600 mm on-center. The cores containing the vertical steel were then filled with grout. One wall specimen did not contain reinforcing steel and was not grouted.

3.3.2 External GFRP Reinforcement

The decision to use GFRP over CFRP was based largely on cost. The CFRP is about ten times more expensive than GFRP. In addition, Albert *et al.* (1998) showed that the out-of-plane flexural strength, deflection, and failure mechanisms of masonry walls

retrofitted with GFRP and CFRP were the same. Although the GFRP and CFRP have different elastic moduli, the specific glass fibre and carbon fibre sheets used had different thickness. By chance, the axial stiffness, the product of the cross-sectional area and modulus of elasticity, was the same for both materials which explains the similar behavior.

The reinforcement strategy was to apply GFRP sheets having equal cross-sectional area to both faces of a wall using the two-part, high strength, high modulus epoxy supplied with the GFRP. All the GFRP was oriented in the same direction with the fibres spanning vertically. Figure 3.1 shows the typical GFRP layout pattern.

3.3.3 Application of GFRP

The application of the GFRP is a three stage process. First, a primer coat of epoxy is applied to the masonry in the regions where the GFRP will be bonded and is allowed 24 hours to cure. Second, after the primer coat is dry, a tack coat of epoxy is applied to the walls and the GFRP is impregnated with epoxy. Third, the GFRP is positioned on the wall by hand and a paint roller is used to work the GFRP against the masonry to ensure a good bond. All the operations involving the application of epoxy and GFRP are done using a standard 240 mm paint roller frame with a 3 mm *Pile Depth* foam roller cover. To impregnate the fibre with epoxy, a 1200 mm x 2400 mm (4 ft x 8 ft) sheet of 19 mm (3/4 inch) plywood covered with heavy-duty clear polyurethane was used as a horizontal work surface. The strips of fibre were laid out on the polyurethane at which time a paint roller saturated with epoxy was used to impregnate the fibre. Since the fibre strips were about 4.0 m long, the strips were continuously rolled up after a convenient length was impregnated on the work surface. This not only prevented the fibre from falling off the work surface, but also made handling and transporting much easier.

Any mortar protruding beyond the face shell of the blocks was ground flush to ensure no premature de-bonding of the GFRP on the compression face of the wall. The primer coat acts to seal the masonry and provides a good bonding surface.

3.4 Full Scale Test Program

3.4.1 Load Frame Description

Figure 3.2 shows the test frame built to conduct the experiments. There are two loading systems incorporated into the setup, one to provide lateral load and one to provide axial load.

The lateral load system is self-equilibrating using a two point loading scheme. The reaction frame of the lateral loading system consists of two W310x129 columns and two WWF350x137 cross beams. Because of the full cycle lateral loading pattern, all load transferring components are able to accommodate both tensile and compressive forces. In addition, all the components were designed to remain stable during the entire test, i.e. no pre-load could be used to hold boundary conditions or loading components in place. Thus, four special "clamps" were designed and fabricated to: distribute a point load from a hydraulic ram or reaction arm into a line load, allow out-of-plane loading in either direction, and ensure all tolerances remain "tight" throughout the entire loading range. The clamps are essentially two W150x22 beams connected by one 19 mm thick plate on each end. A strip of 6 mm thick compressible foam was sandwiched between the inside facing flange and corresponding face shell of the masonry units. The foam prevents vertical slippage of the clamping arrangement, prevents the steel flange from bearing directly on the masonry and GFRP, and compensates for minor geometric imperfections in wall construction. Once located at the correct height on each side of the wall, the two wide flange components are drawn together using a screw type arrangement. This procedure serves to pre-load the clamping arrangement by compressing the foam. End plates are then bolted across each end of the assembly using slip critical connections to ensure proper load transfer through the system.

3.4.2 Lateral Load System

Lateral load was applied through two 90 kN hydraulic jacks located 1192 mm from the top and bottom lateral reactions. One end of each jack was pinned to the cross-beam

between the columns and the other end was pinned to its respective loading clamp. The lateral reaction forces were transferred from the bottom and top reaction clamps to the columns through HSS 76x51x4.8 rigid links. Four reaction links were used, one on each side at the top and bottom. Each end of the reaction links was fitted with a rod-end bearing to allow for minor longitudinal adjustment, accommodate slight misalignment, and provide a low friction, pin type connection.

3.4.3 Axial Load System

The axial load was applied via a W150x22 distributing beam located at the top of the specimen. Sandwiched between the lower flange of the distributing beam and the upper face of the top course of the wall was a piece of fibreboard. This piece of fibreboard served as a crush zone to allow for uniform bearing on the top course of the wall. A hydraulic jack and coil spring arrangement were placed against the underside of the laboratory strong floor. High strength steel rods were connected between the axial load distributing beam and the jack-spring arrangement to transfer the axial load. Coil springs were included to maintain a constant axial load when the wall height changed due to large lateral deflections. The boundary conditions at the bottom of the wall included both a set of rollers and a knife edge. Typically, only a knife edge is required when testing walls under flexure; however, the center of rotation for the vertical and lower lateral reaction points did not coincide. Thus, a set of rollers was required under the steel base plate to release the lateral degree of freedom to ensure no undesirable restraint at the bottom of the wall.

The axial load capacity of the system was based upon design dead and live loads from a one storey warehouse type building in Vancouver, British Columbia, Canada. Rain and snow loads were chosen from this city since it is located in a zone of potentially high seismic activity along the west coast of North America.

3.4.4 Hydraulic and Controls System

The hydraulic and controls system used to apply the lateral load consisted of many components. An MTS 76 L/min (20 gpm) pump supplied a constant hydraulic system pressure of 20.7 MPa (3000 psig). The hydraulic loop started at the pump, flow then proceeded to a Hydraulic Accessory Module (HAM) unit, next to the servo valve manifold, then back to the HAM unit and finally back to the reservoir. The HAM unit serves two purposes. First, it is fitted with a filter to remove particulate and second, it has two accumulators which buffer any sudden changes in hydraulic supply pressure. The servo valve acts as the bridge between the hydraulic system and the controls system. Upon receiving a signal from the control loop, the servo valve directs flow to either the head or rod end of the jack to change the position of the ram.

The control system originates with a program in a micro profiler. The micro profiler converts a loading rate into an electrical signal which is sent to a signal conditioner. The signal conditioner interfaces with a hydraulic servo valve and a Linear Variable Displacement Transducer (LVDT) attached to the hydraulic jack ram in order to monitor its position. Thus, a feedback loop is created which controls the position and movement of the hydraulic ram.

In this testing program, stroke control was used during testing. Because two jacks were used, two identical hydraulic and control systems were required. The signal from the micro profiler was directed to both signal conditioners simultaneously. The objective was to move both hydraulic rams in unison to obtain a relatively even loading in both jacks. This required that both systems be calibrated in-phase with each other. An oscilloscope was connected to both systems and each was adjusted until the two superimposed waveforms matched. This procedure was performed only once during the initial test setup and no adjustments were made thereafter.

3.4.5 Instrumentation

The objective of the instrumentation scheme for each test was to measure loads, changes in wall geometry, and strain profiles in both the GFRP and steel reinforcement.

This was achieved using load cells, LVDTs, cable transducers, rotation meters, and foil strain gauges. All data were recorded through an electronic data acquisition system.

Six load cells were used in the lateral loading system. One load cell was connected to each of the two hydraulic jacks and one load cell was integrated into each of the four reaction links. Figure 3.3 shows the arrangement of the loading and reaction load cells. Each was designed and fabricated specifically for this testing program to ensure maximum sensitivity while limiting the maximum strain to maintain linear elastic behavior. To measure the axial load, each of the two load rods joining the top distributing beam to the jacks on the underside of the strong floor were fitted with foil strain gauges and calibrated.

A combination of five LVDTs and two cable transducers were used to measure the lateral deflection of the wall. Figure 3.3 shows the layout of this instrumentation. Deflections were measured with LVDTs at the mid-point between the bottom reaction and bottom loading points, at the bottom and top loading points, at the mid-point between the loading points, and the mid-point between the top loading and the top reaction points. One cable transducer was placed at the upper and lower quarter points within the zero-shear span. This gave a total of five data points for plotting the deflected shape of the zero-shear span region. Lateral deflections were considered to be zero at the top and bottom reaction points as these locations were connected to the load frame with rigid links.

Three cable transducers were used to measure any vertical movement between the loading and reaction clamps. The instruments were mounted along the sides of the wall as seen in Figure 3.3. This was done to obtain an accurate center-to-center measurement; as well as, the instrumentation did not interfere with any other components in the system.

A rotation meter was mounted on each jack to monitor any angle change during the loading cycle.

Two series of strain data were measured, one series from the reinforcing steel and one series from the GFRP. Each piece of reinforcing steel was fitted with three foil strain gauges. The gauges were located at the tenth course level respectively at: lower bed joint, center of block, and upper bed joint. To accurately locate the gauges, the steel was

placed inside the respective core of the completed wall, marked for length, removed, and finally cut to length. Measurements were then taken from the top the wall to the joint and center of block locations and then transferred to the reinforcing steel. After bonding the gauges to the steel reinforcement and soldering the wire pig tails to the leads on each gauge, a layer of silicon was placed over each gauge for protection against damage during the grouting process. Figure 3.4 shows the typical layout of these gauges. Six foil strain gauges were bonded to the north most GFRP strip on each face of the wall. Figure 3.5 shows the typical layout of the gauges. Two rows of gauges were used at the location of the tenth course. Three gauges were located across the GFRP at the level of the upper bed joint and three gauges were located across the GFRP at the center of block level. The gauges at each side of the GFRP were located 10 mm from the edge of the strip and the middle gauges were centered within the GFRP sheet. This criteria was used to locate the gauges because of the varying GFRP strip widths. A technique for applying the foil strain gauges to the GFRP was developed at the University of Alberta. The technique involves using a small amount of "Five Minute" epoxy to create a flat surface to bond the strain gauge to. A small amount of epoxy is place on the GFRP at the desired gauge location and a piece of clear tape is placed over the epoxy to form a surface flush with the contours of the GFRP. Once the epoxy has cured, the clear tape is removed and the strain gauge is bonded to this epoxy surface.

All data readings were recorded through a Fluke™ electronic data acquisition systems during testing and stored on a PC. The data sampling rate was set to "manual", thus all data readings were signaled by pressing a key on the keyboard. A Hewlett Packard™ X-Y plotter was connected in parallel with the data acquisition system. In real-time, the plotter recorded the lateral load versus deflection curve. The advantage of using the plotter while testing is it provides a graphical representation of the test to the operator. Thus, any observed anomalies can be addressed or noted as soon as they occur.

3.4.6 Testing Procedure

Each of the four lateral load clamps was assemble on the lab floor and then positioned on the wall using the overhead crane. The clamps were centered and tightened

before the crane was disconnected to ensure the clamps did not slide down the wall. A lifting device incorporating the axial load distributing beam and the steel base plate was used. A steel bracket was bolted to each side of the steel baseplate and had provisions to connect to one end of a large turn buckle. The other end of each turn buckle was connected to high strength steel rods which ran up, along each end of the wall to the axial load distributing beam. After centering all the components, the turn buckles were tightened which induced an axial load into the wall. The overhead crane was then connected to the axial load distributing beam using a shackle. Figure 3.6 shows this operation. This lifting arrangement ensured the walls would remain uncracked during positioning and provided a safe lifting procedure.

Before moving the wall into the final position, the lower boundary condition, namely the rollers and knife edge, was properly aligned. The wall was then positioned over the lower boundary support leaving a vertical space of about 10 mm. The lateral reaction links were connected and the wall was lowered onto the lower boundary support. Following this procedure ensured that each wall specimen was properly centered. The jacks and instrumentation were then connected in an arbitrary manor and all bolted connections were checked for proper torque. The lifting brackets and turn buckles were removed from the baseplate and longer axial load rods were connected to the axial load distributing beam. These longer rods passed through the laboratory strong floor leaving about 1.2 m exposed below the underside of the strong floor. The axial load hydraulic jack and spring arrangements were slipped over each load rod and a nut was threaded up each load rod to remove the slack from the system.

Before testing, all the electronic systems were given 12 hours to warm-up so the systems would be electrically stable. Once all the instruments were checked, an initial data reading was taken and then the axial load was applied. Following another data reading, the lateral loading program was started. Guidance from the Applied Technology Council (ATC 24) manual was used to determine this lateral loading program. The loading program for each specimen was divided into two phases, controlling the level of load and controlling the amount of centerline displacement. The first three groups of cycles consisted of the load control mode. The term "group" refers to a family of fully-reversed complete cycles. Within each group, the walls were subjected to a constant,

predefined load level for three consecutive cycles. Thus, a total of nine complete cycles for the load control phase of the test were performed. The load level for each group was calculated as a percentage of the predicted ultimate load obtained from the strength model presented in Chapter 5. Typically, the predicted ultimate lateral load was divided by four. The load level for the first group was assigned one-quarter, the second group was assigned one-half, and the third group of load control cycles was assigned three-quarters of the predicted ultimate load.

The second stage of the lateral loading program for the walls was based on a centerline displacement criterion. A reference displacement was taken as the largest displacement experienced during the final group of load control cycles, group three. This reference displacement was divided by three and typically rounded up or down to the nearest multiple of 5 mm to obtain the incremental displacement required for the subsequent loading cycles. Each group of displacement controlled cycles included one or two complete loading cycles to the specified displacement. This was continued until the ultimate capacity of the wall was obtained. The loading levels for each specimen are described in Section 3.5.

3.5 Test Observations

The following section provides a general description of each wall specimen during testing. During each test, the load versus centerline deflection hysteresis was plotted in real time to provide a graphical insight into the behavior of each wall specimen. These figures are included in this chapter as raw data and is thus helpful in describing each test. The walls were tested in the following order: Wall 5a, Wall 5b, Wall 1, Wall 8, Wall 6, Wall 7, Wall 3, Wall 4, Wall2.

3.5.1 Wall 5a, 5b (Tests 1 & 2)

Two tests were performed on Wall 5. Specimen 5a had no externally applied GFRP but did contain two 10M reinforcing bars. Once positioned in the loading frame, an initial data reading was taken and then the axial load was applied. A second data reading

was taken after which the lateral loading was started. This procedure of applying the axial load before beginning the lateral loading was common to all the tests. The lateral load consisted of thirteen cycles in which the first nine cycles were controlled by the level of lateral load and the remaining five cycles were controlled by level of centerline deflection. Figure 3.7 shows the load versus deflection hysteresis. As mentioned in Section 3.4.4, the lateral load was applied using stroke control for the hydraulic jacks. Thus, to obtain reasonable loading rates throughout the test, values of 1, 2, 4, and 10 mm/min of jack stroke were programmed into the signal generator. Load reversals were manually performed when either the desired level of load or centerline deflection was reached.

The first three groups of cycles were controlled by load levels of 2.5, 3.5, and 4.5 kN per jack. The remaining groups of cycles were controlled by increasing the centerline deflection by 30 mm for each successive group. No visible cracking occurred until the fourth cycle which was the first cycle at the load level of 3.5 kN per jack. At this point, cracking occurred at the joint locations in the zero shear span. These cracks grew progressively larger as the level of lateral load was increased. On the thirteenth cycle, no increase in lateral load resistance was observed, as seen in Figure 3.7, and the testing was stopped. This wall could have tolerated further deformations but it was desired to retrofit a partially damaged wall with externally applied GFRP.

Wall 5b was the previously described specimen retrofitted with two 250 mm wide GFRP sheets on each side of the wall. Figure 3.8 shows the load versus deflection hysteresis for this specimen. The load levels for the first three group of cycles were 3.5, 10, and 15 kN per jack. An increase of 25 mm was used for the deformation controlled cycle groups. On the first loading cycle at 5.2 kN, the GFRP spanning a joint on the compression side in the zero shear region began to buckle outwards. As the test progressed, this buckling phenomena of the GFRP occurred at most joints in the zero shear span. Figure 3.9 shows this localized buckling of the GFRP. When the lateral load on the wall was reversed, the buckles in the GFRP gradually disappeared as the GFRP began to be loaded in tension. Cracking at the joints on the tension face was evident from the first cycle due largely to the fact that the wall was previously cracked. A sudden failure of this wall occurred on the eleventh loading cycle when the jack stroke for both

jacks exceeded the calibrated range. This resulted in both jacks continuing to travel to the fully extended position which caused an unexpected catastrophic failure.

3.5.2 Wall 1 (Test 3)

Before Wall 1 was tested, the control system governing the jack strokes was re-calibrated to accommodate a larger stroke to eliminate the problem which occurred while testing Wall 5b. Wall 1 was considered to be the standard wall from which all the testing parameters would be varied. This specimen was identical to Wall 5b with the exception that the GFRP was applied to the wall in the undamaged state. The loading levels for the first three group of cycles were 7, 14, and 21 kN per jack. An increase of about 20 mm was used for each successive group of deformation cycles. Figure 3.10 shows the load versus deflection hysteresis. During the first group of loading cycles, hairline cracks developed at the mortar joints between the two vertical sheets of GFRP as seen in Figure 3.11. By the third group of loading cycles, the mortar joints were fully cracked and there was no debonding or localized buckling of the GFRP while under compression. Figure 3.12 shows some diagonal cracks forming in the masonry along each sheet of GFRP. These cracks started at the edge of the GFRP sheets about 50 mm from each bed joint and digressed at 45 degree angles to the bed joints. During the twelfth cycle, a vertical crack opened on the side of the block in the sixth course from the bottom which induced the failure mode of flexure-shear. The testing was stopped at this point and the wall was returned to the zero position.

3.5.3 Wall 8 (Test 4)

This specimen was reinforced internally with two 15M steel bars and externally with two 250 mm wide GFRP sheets on each side of the wall. The axial load level was 30 kN and the lateral loading levels for the first three groups of cycles were 7, 14, and 21 kN. The displacement controlled cycles were incremented by 15 mm for each successive group. The load versus deflection hysteresis is shown in Figure 3.13.

No visible cracking was observed until the second group of loading cycles at which time the bed joints started cracking. By the end of the third group of cycles, diagonal shear cracks were forming in the face shells as described in the previous section. Once the centerline deflections reached about ±70 mm, horizontal cracks through the middle of the face shells starting appearing in every second course between the GFRP sheets within the zero shear span. This horizontal cracking is illustrated in Figure 3.14. This wall specimen was the most heavily reinforced and thus, carried the greatest level of lateral load and centerline deflection. Again, the flexure-shear mode of failure forced the end to the test.

3.5.4 Wall 6 (Test 5)

For specimen 6, the axial load was reduced to 15 kN and the steel reinforcement and the GFRP remained at two 10M and two 250 mm wide sheets respectively. The first three groups of cycles were loaded to 7, 14, and 21 kN. Cracking in the bed joints begun in the second group of cycles and diagonal cracks on the face shells started to appear on the tenth cycle. On the eleventh cycle, vertical splitting through the sides of the blocks located in the courses of the shear span just adjacent to the zero shear span occurred. This vertical cracking resulted in a flexure-shear failure on the thirteenth cycle. Figure 3.15 shows the load versus deflection hysteresis for this specimen.

3.5.5 Wall 7 (Test 6)

The axial load was increased to 50 kN for specimen 7. Both the steel reinforcement and the GFRP remained at two 10M and two 250 mm wide sheets per side respectively. The first three loading cycle groups were increased incrementally by 7 kN and the deformation controlled cycle groups were increased by 10 mm. The onset of bed joint cracking did not occur until the third group of load controlled cycles and the progression of this cracking throughout zero shear span happened at a slower rate over more cycles than the previous tests. The failure was well pronounced on the fourteenth cycle with a

loud "crack" and a sudden drop in load as seen in Figure 3.16. Again, the flexure-shear failure mode occurred.

3.5.6 Wall 3 (Test 7)

The parameters for Wall 3 were two 10M reinforcing steel bars, 30 kN of axial load, and two 125 mm wide GFRP sheets on each side of the wall. For the first three groups of loading cycles, 5, 10, and 15 kN were used. The deformation controlled cycle groups were incremented at 15 mm. Refer to Figure 3.17 for the load versus deflection hysteresis. Visible cracking in the bed joints within the zero shear span occurred in the first loading group and progressively increased in width. In the tenth cycle, diagonal cracks began to appear on the face shells. At no point did any horizontal cracks appear through the center of any blocks as was seen on most of the specimens fit with two 250 mm GFRP sheets per side. Figure 3.18 shows the failure location which occurred at the top of the lower shear span on the west face on the wall. This failure was unique to this specimen in that a highly localized region induced a peeling off of the GFRP. Typically, peeling off of the GFRP is induced by the flexure-shear mode in which shear cracking of an entire block results in the relative lateral movement between two courses. In this specimen, only the upper one-quarter of a block slightly fractured and translated laterally causing the GFRP to rip or peel off the masonry below this point.

3.5.7 Wall 4 (Test 8)

Wall 4 had the least amount of GFRP externally applied. Two 65 mm wide sheets were used in addition to the two 10M reinforcing bars and 30 kN of axial load. The levels of lateral loading used for the first three groups of cycles were 3, 6, and 9 kN. Each deformation controlled group of cycles was incremented by 15 mm. Figure 3.19 shows the load versus deflection hysteresis for this specimen. During the second group of loading cycles, cracks started to form along the bed joints only. In the second group of deformation controlled cycles, specifically cycle 12, diagonal cracks started to appear in the face shells as shown in Figure 3.20. However, the angle from which these cracks

propagated away from the GFRP sheets was considerable less than the wall specimens with wider GFRP sheets. This angle was in the order of 20 degrees as opposed to the typical 45 degrees. In addition, the GFRP buckled over the block region between each bed joint as seen in Figure 3.21. Again, this observed behavior was completely opposite to the GFRP buckling over the bed joint region in the previously described specimens. This buckling behavior will be further discussed in Chapter 4. The failure of this specimen was classified as a serviceability mode in that the specimen was loaded to the limits of the load frame in terms of the centerline deformation. Thus, the ultimate strength was not determined and the wall looked relatively undamaged at the end of the test.

3.5.8 Wall 2 (Test 9)

The final specimen tested had no steel reinforcement, rather only two 250 mm wide GFRP sheets per side. The axial load remained at 30 kN for this test. The lateral loading levels for the first three groups of cycles was 4, 8 and 12 kN and the increment for the deformation controlled cycles was 10 mm. Figure 3.22 shows the load versus deflection hysteresis for this specimen. In the second group of loading cycles, cracks appeared in the bed joints; as well as, diagonal crack started appearing in the face shells. The GFRP did not start buckling over the bed joints until cycle thirteen, the second to last cycle. On the fourteenth cycle, a sharp drop in load occurred as the specimen failed under the flexure-shear mode. The load versus deflection behavior for this specimen was identical to specimen MCST 7-4 tested by Albert *et al.* (1998) which had the same geometric properties and reinforcement layout.

3.6 Flexure-Shear Failure Mode

The only observed mode of failure was that of flexure-shear. This failure mode typically occurred simultaneously in the courses directly below the lower load line and directly above the upper load line. At these locations, the combination of shear force and curvature is at a maximum. The progression of this failure type is shown in figure 3.23.

At small lateral deflections, cracks appear at the bed joint location due to flexure. As lateral deflections become large, rigid body rotations occur between adjacent blocks to accommodate the wall curvature. Vertical and/or diagonal cracks begin to form on the ends of the blocks immediately below and above the lower and upper loading lines respectively. This is shown in Figure 3.24. These cracks typically start at the bed joint to block interface at a depth equivalent to either half the wall width or the thickness of the face shell. Both of these locations can be viewed as regions of high stress concentration as there are radical changes within the cross-sectional geometry of the masonry units. The cracks eventually cause the blocks to split and two pieces translate laterally away from one another. This translation, if large enough, begins to debond the GFRP on the tension face within the shear span inducing a peel-off effect.

3.7 System Integrity

The performance of the GFRP reinforced masonry walls was highly successful under flexural loads. Figure 3.25 shows the wall integrity was maintained at extreme lateral deflections. The tests showed stable, predictable behavior with highly enhanced strength and stiffness. The system also remarkably maintained its integrity under repetitive high stress fully reversed cycles of load and large flexural deformations. This is demonstrated in a typical load versus deflection hysteresis response as that shown in Figure 3.10. The unloading/reloading paths for successive loading cycles was similar indicating little degradation. Each unloading path passed near the origin forming a hysteresis response with a pinched nature. Damage occurred during each loading cycle only when the load level achieved in a previous cycle was exceeded. The response consistently followed a typical envelope resulting in the wall system maintaining it's integrity throughout.

Table 3.1 Masonry Prism Test Results

Statistics	Ungrouted f'_m	Fully Grouted f'_m
Mean	10.33 MPa	9.32 MPa
Standard Deviation	1.31 MPa	1.34 MPa
Coefficient of Variation	12.73 %	14.35 %

Table 3.2 Steel Reinforcement Tension Coupon Results

Specimen	σ_y (MPa)	σ_u (MPa)	E (MPa)
10M	434	670	200000
15M	441	692	201000

Table 3.3 Glass Fibre Reinforced Polymer Coupon Tests

Fibre Type	ε_u (mm/mm)	E [1] (MPa)	E* [2] (N/mm)	E** [3] (N/mm)
Glass Sheet (SEH51)	0.022	27521	35651	27579

[1] Modulus based on manufacturer's fibre thickness of 1.2954 mm (0.051")

[2] Modified Modulus (load/fibre width/strain)

[3] Manufacturer's published Modulus

Table 3.4 Test Specimen Parameters

Specimen	Steel Reinforcement (bar type)	GFRP (width per side) (mm)	Axial Load (kN)	Number of Full Cycles	Ultimate Total Load (kN)	Ultimate Deflection (mm)
Wall 1	2 – 10M	500 (2 x 250)	30	12.5	57.1	98.9
Wall 2	none	500 (2 x 250)	30	15.5	38.1	82.3
Wall 3	2 – 10M	500 (2 x 125)	30	13.5	39.0	122.2
Wall 4	2 – 10M	500 (2 x 65)	30	13.5	28.4	137.0
Wall 5a	2 – 10M	none	30	15	15.2	58.9 [1]
Wall 5b	2 – 10M	500 (2 x 250)	30	10.5	53.2	88.6
Wall 6	2 – 10M	500 (2 x 250)	15	12.5	65.3	113.5
Wall 7	2 – 10M	500 (2 x 250)	50	13.5	69.1	118.0
Wall 8	2 – 15M	500 (2 x 250)	30	13.5	84.1	132.0

[1] Wall 5a was not tested to ultimate failure

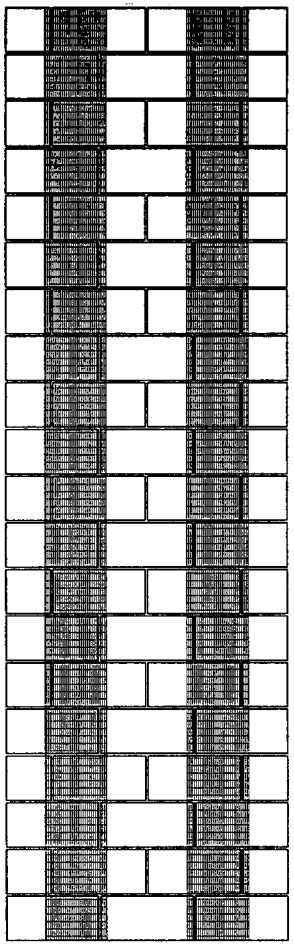

2 – 250 mm Wide Sheets

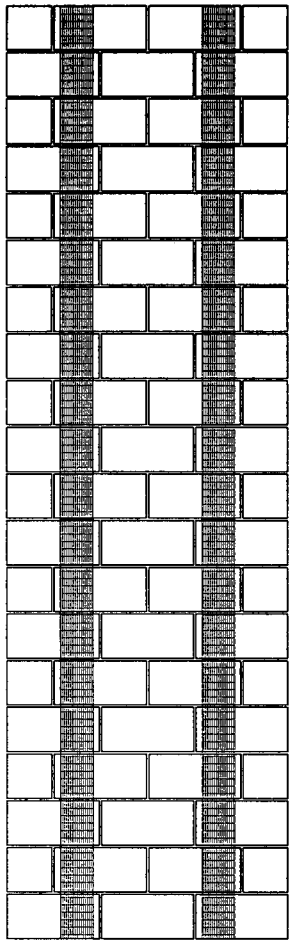

2 – 130 mm Wide Sheets

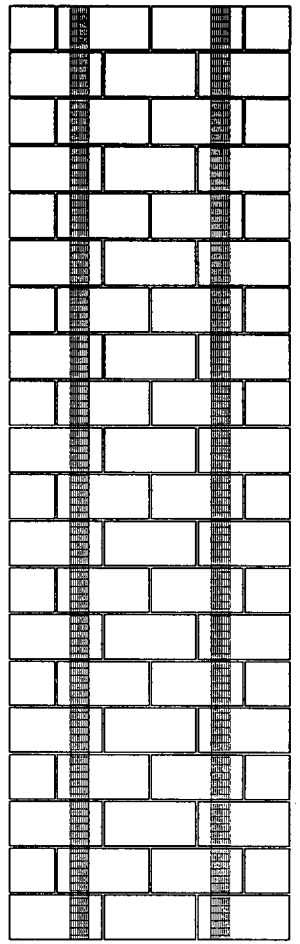

2 – 65 mm Wide Sheets

Figure 3.1 GFRP Layout

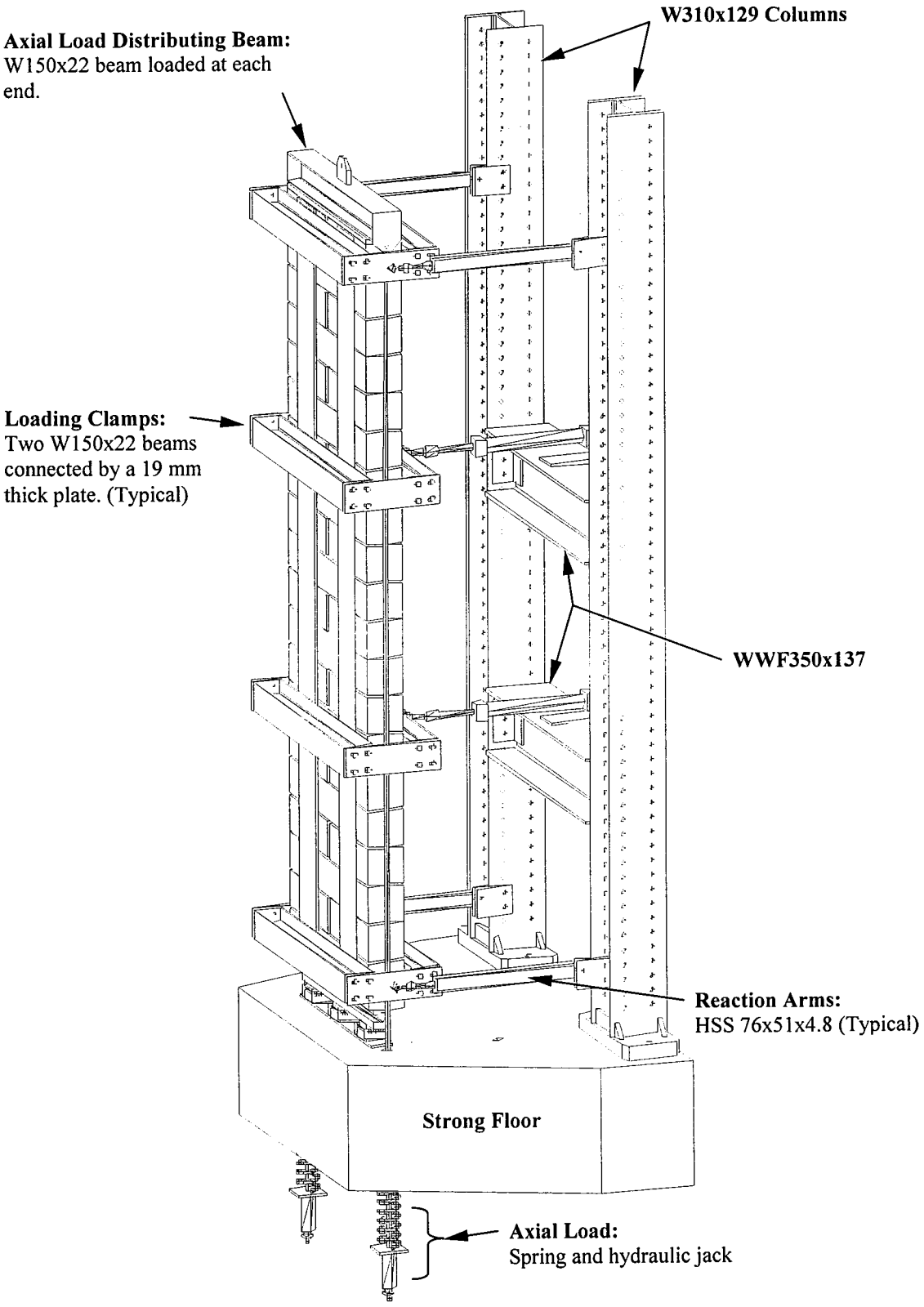

Figure 3.2 Test Setup

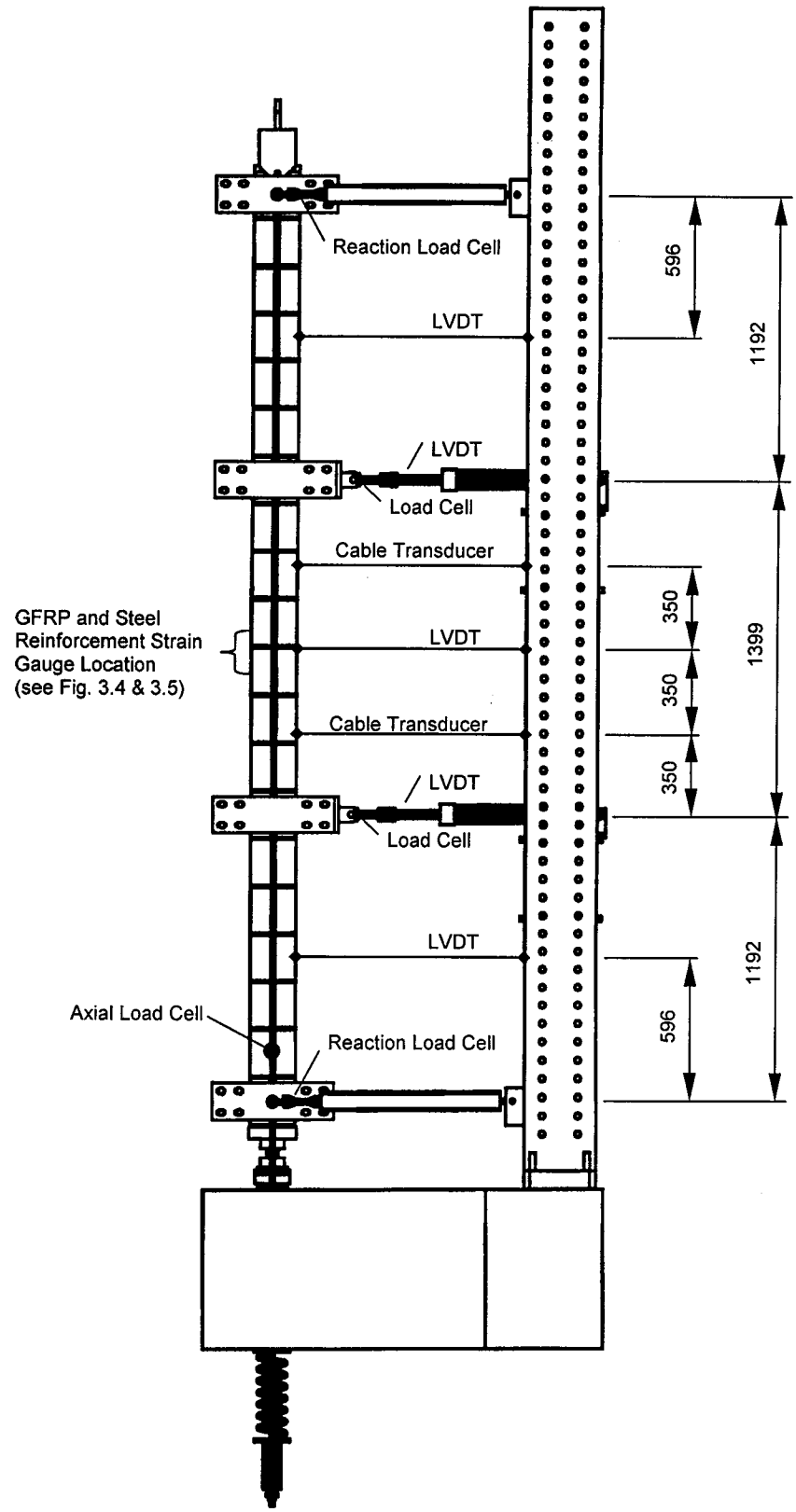

Figure 3.3 Instrumentation Layout

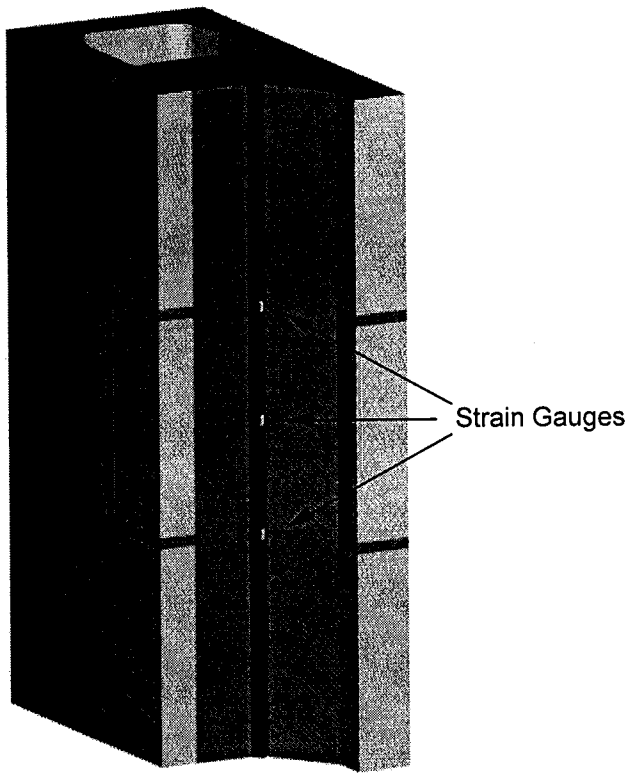

Figure 3.4 Layout of Strain Gauges on Steel Reinforcement

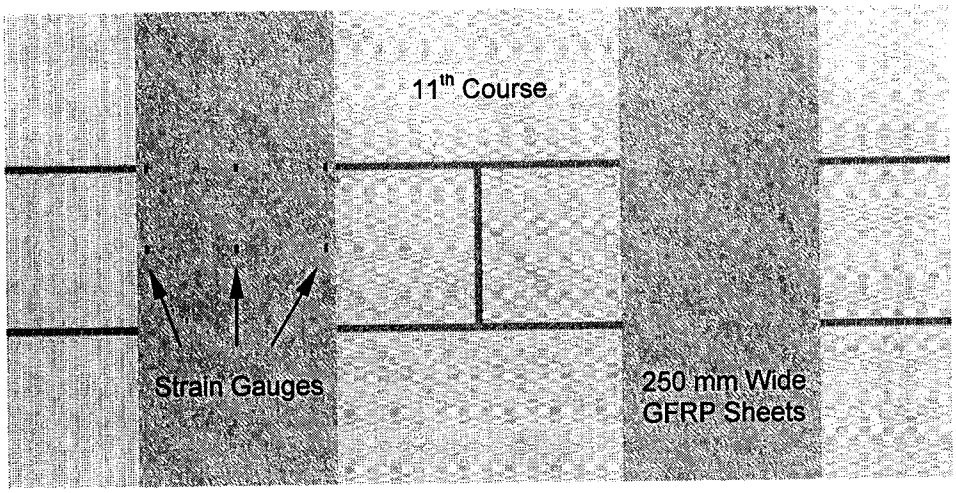

Figure 3.5 Layout of Strain Gauges on GFRP

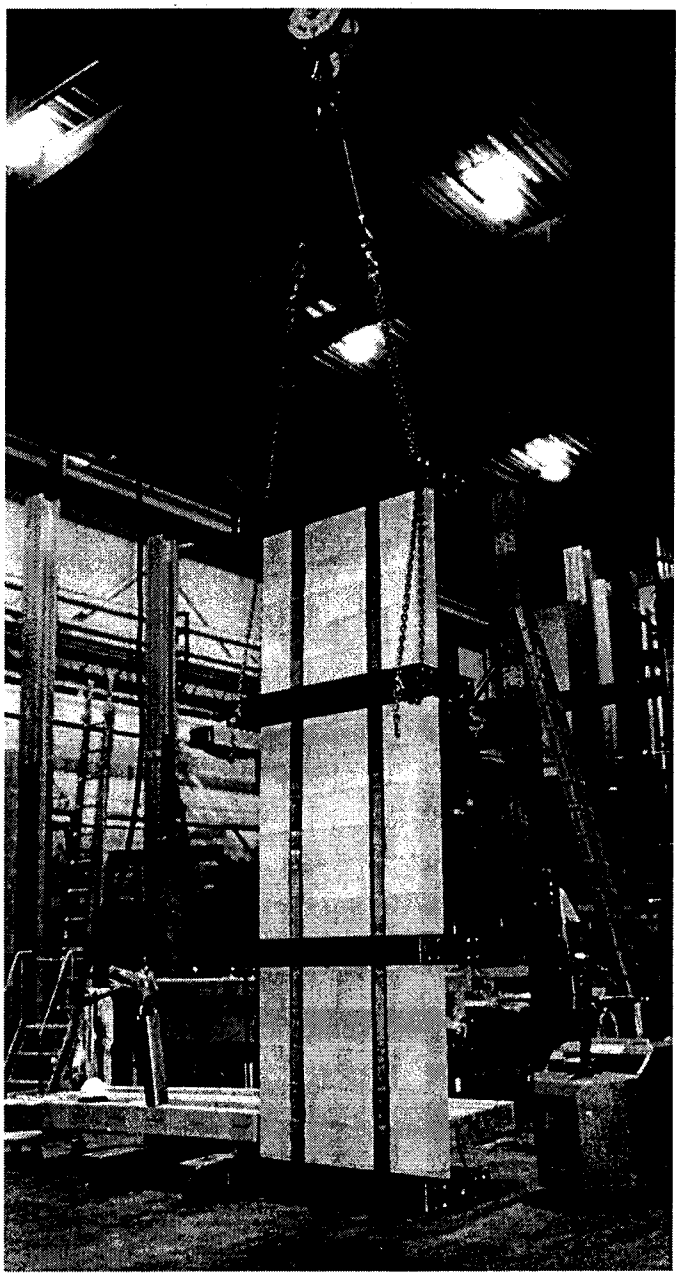

Figure 3.6 Positioning of Walls

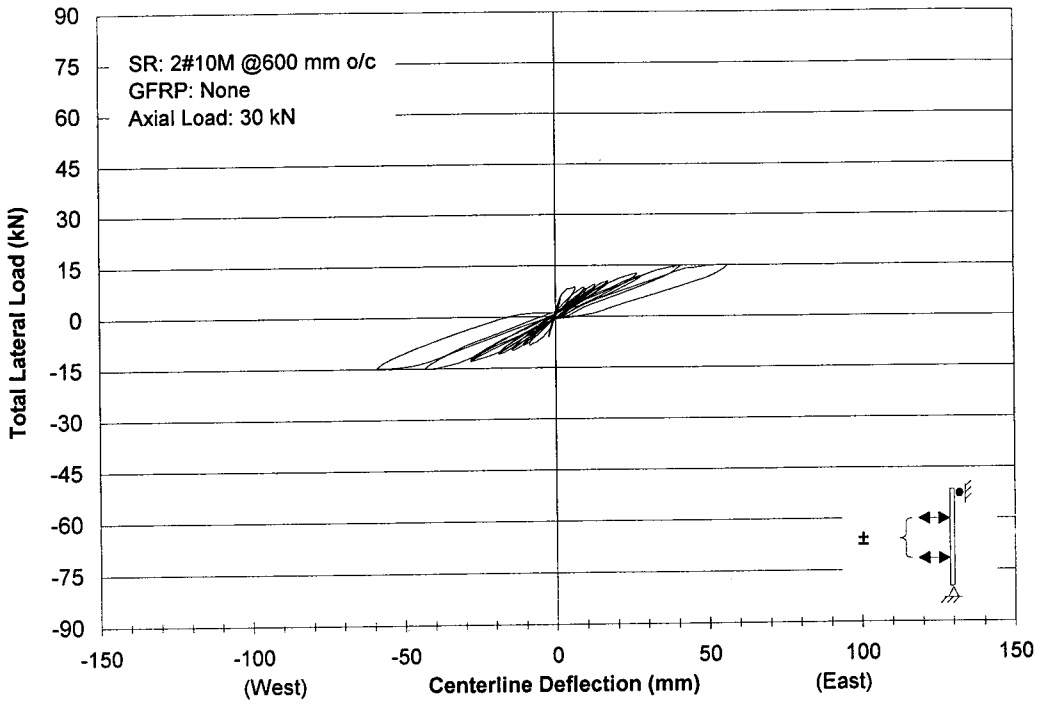

Figure 3.7 Load versus Deflection Hysteresis for Wall 5a

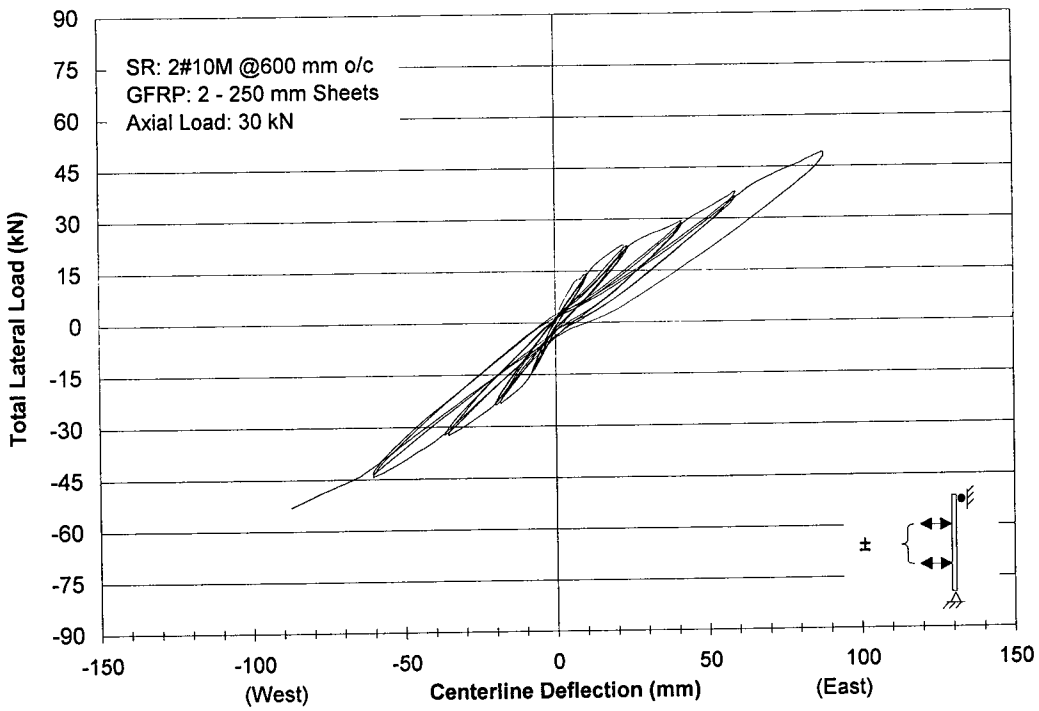

Figure 3.8 Load versus Deflection Hysteresis for Wall 5b

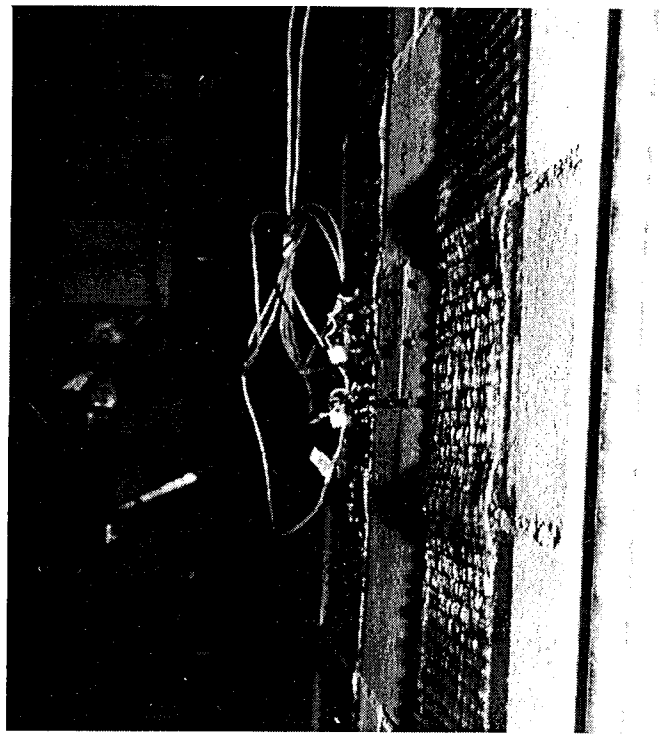

Figure 3.9 GFRP Buckling at Bed Joint Location

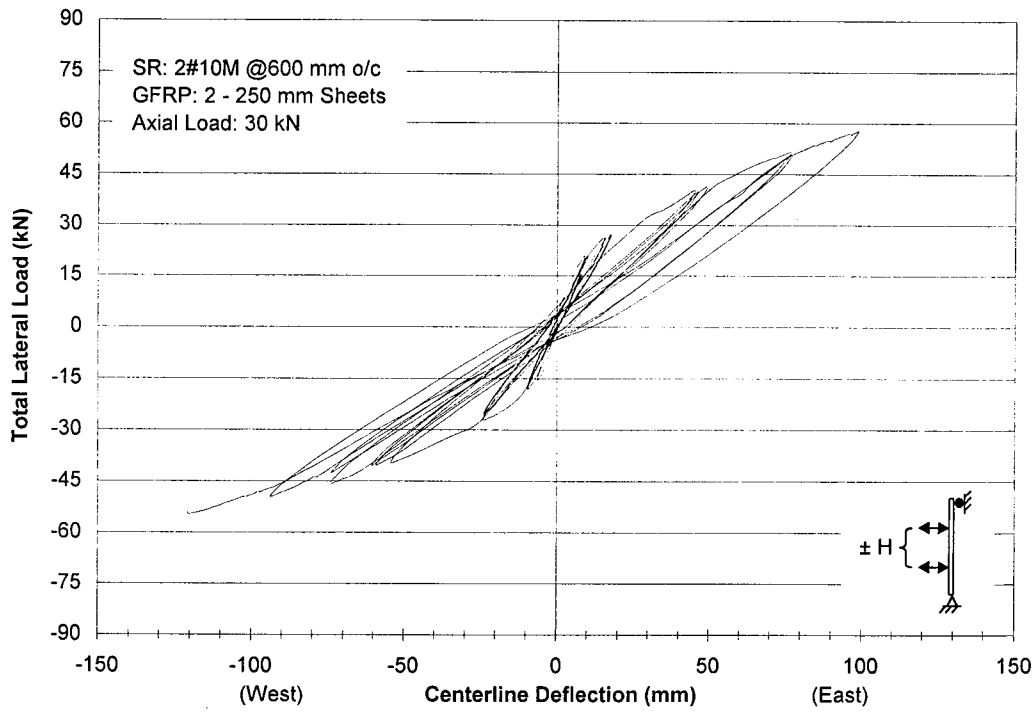

Figure 3.10 Load versus Deflection Hysteresis for Wall 1

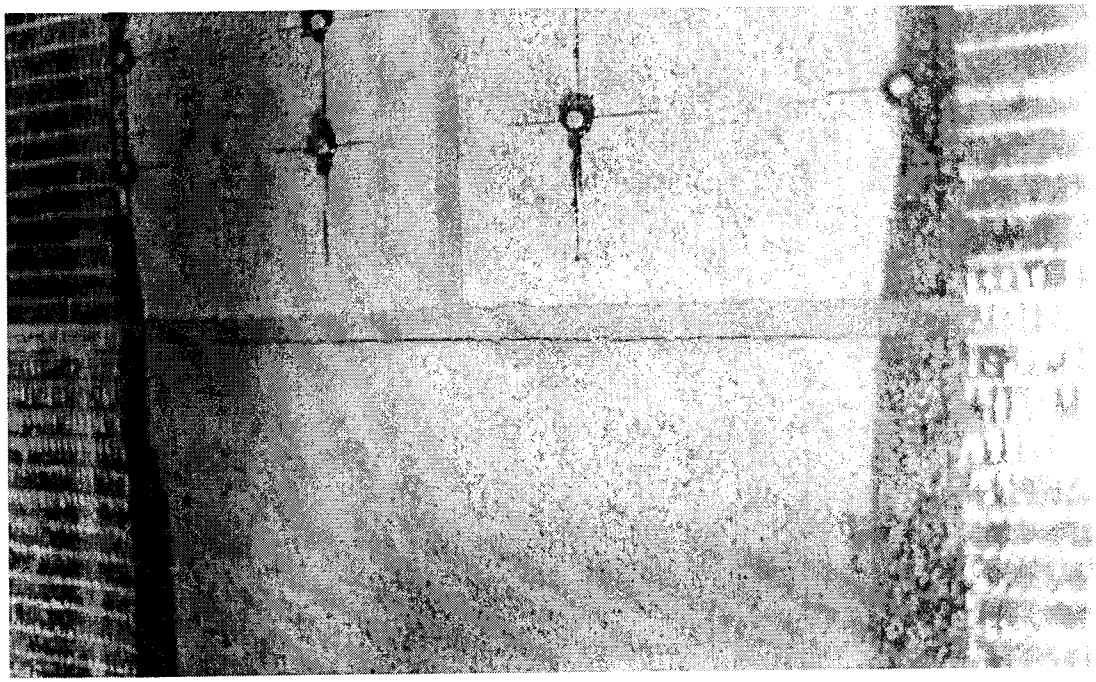

Figure 3.11 Horizontal Cracking within the Bed Joints

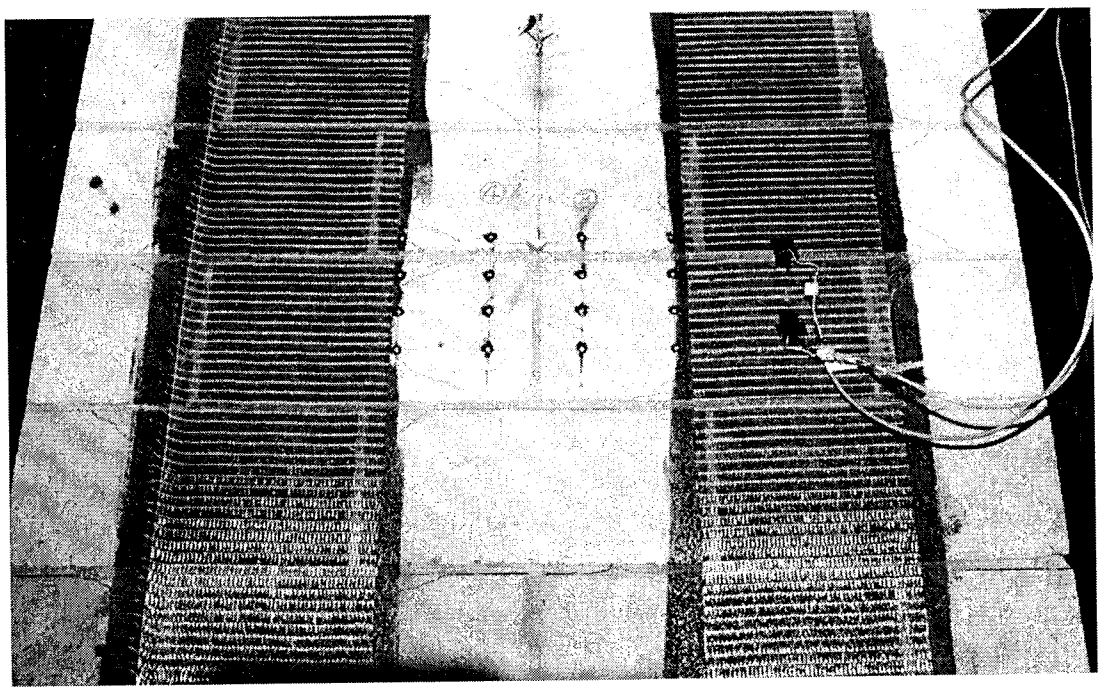

Figure 3.12 Diagonal Cracking of Masonry

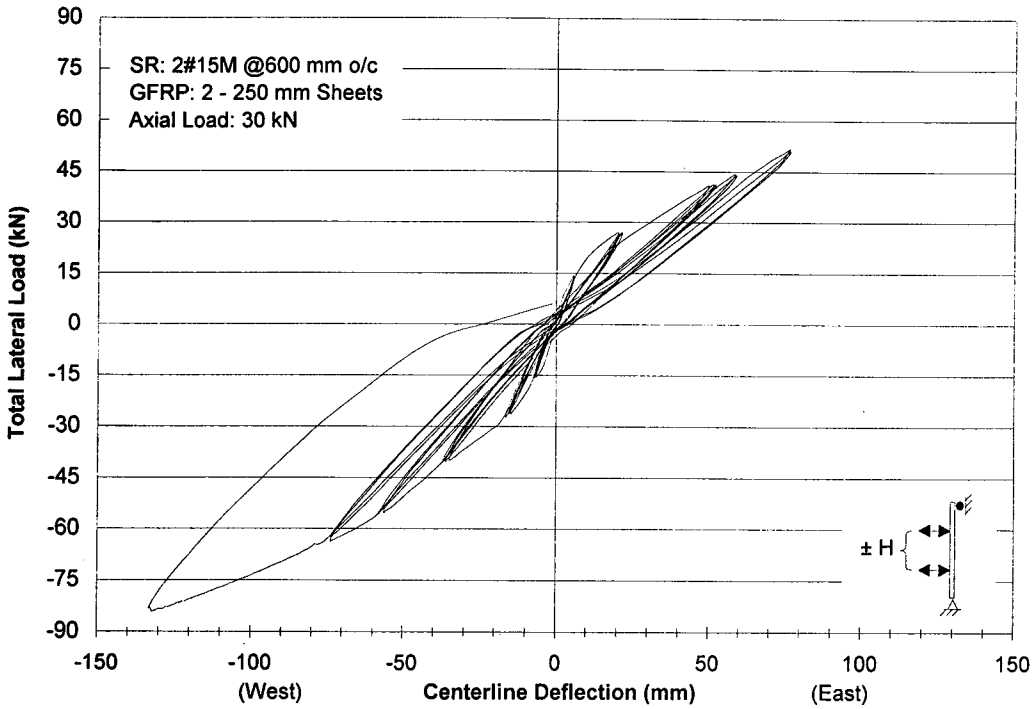

Figure 3.13 Load versus Deflection Hysteresis for Wall 8

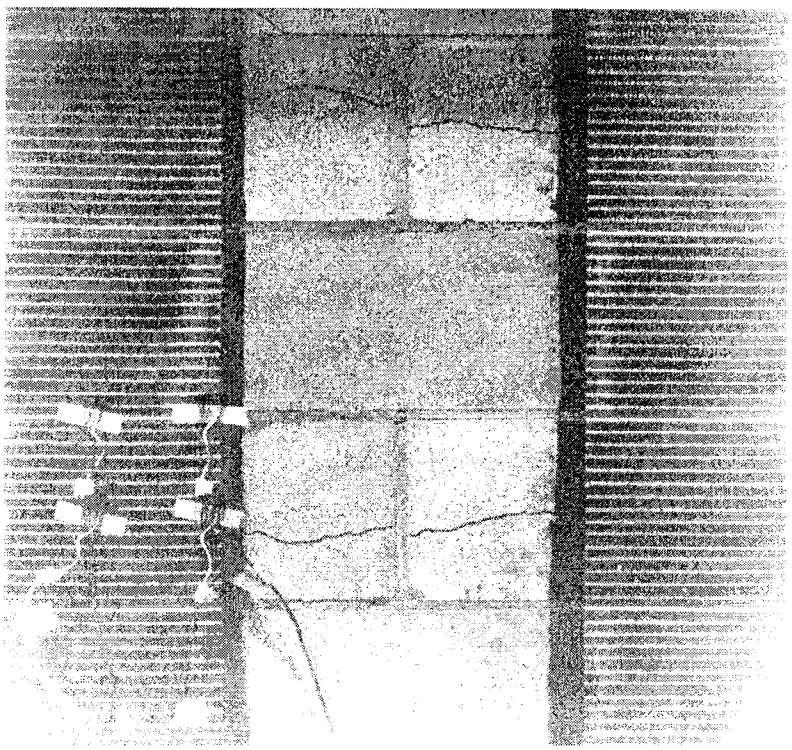

Figure 3.14 Horizontal Cracking of Masonry Units

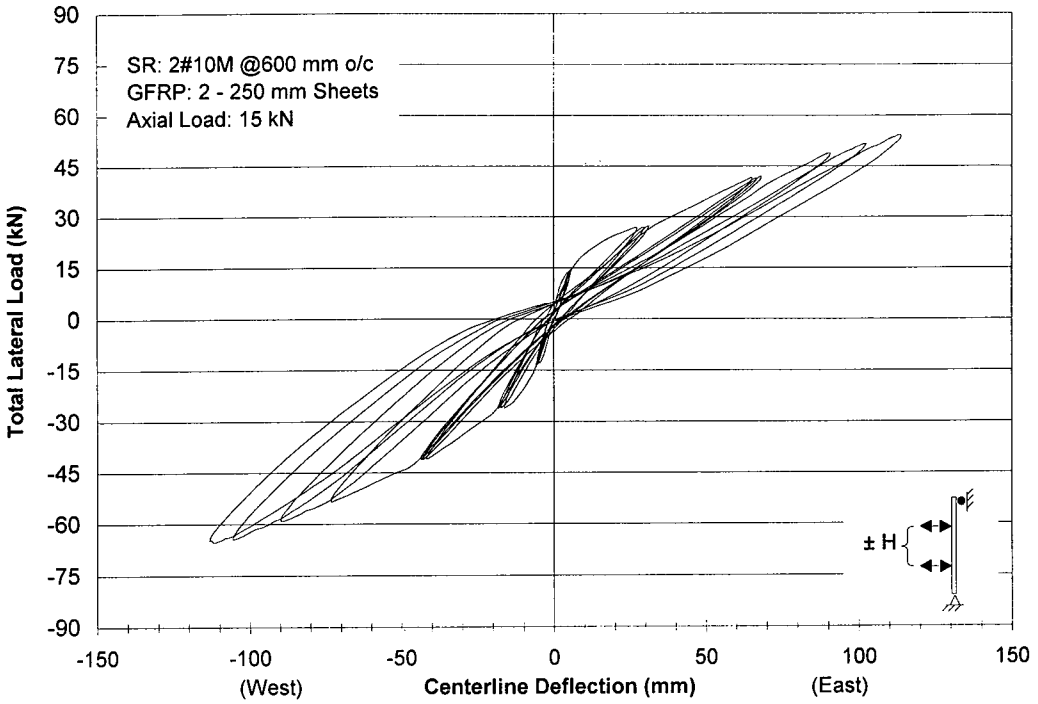

Figure 3.15 Load versus Deflection Hysteresis for Wall 6

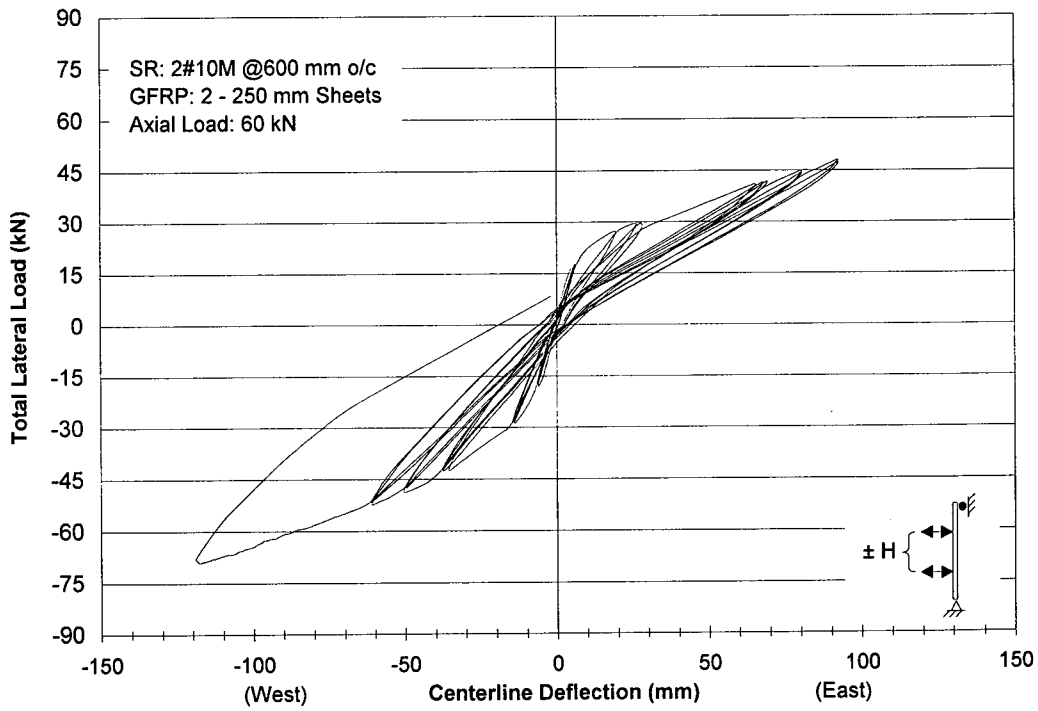

Figure 3.16 Load versus Deflection Hysteresis for Wall 7

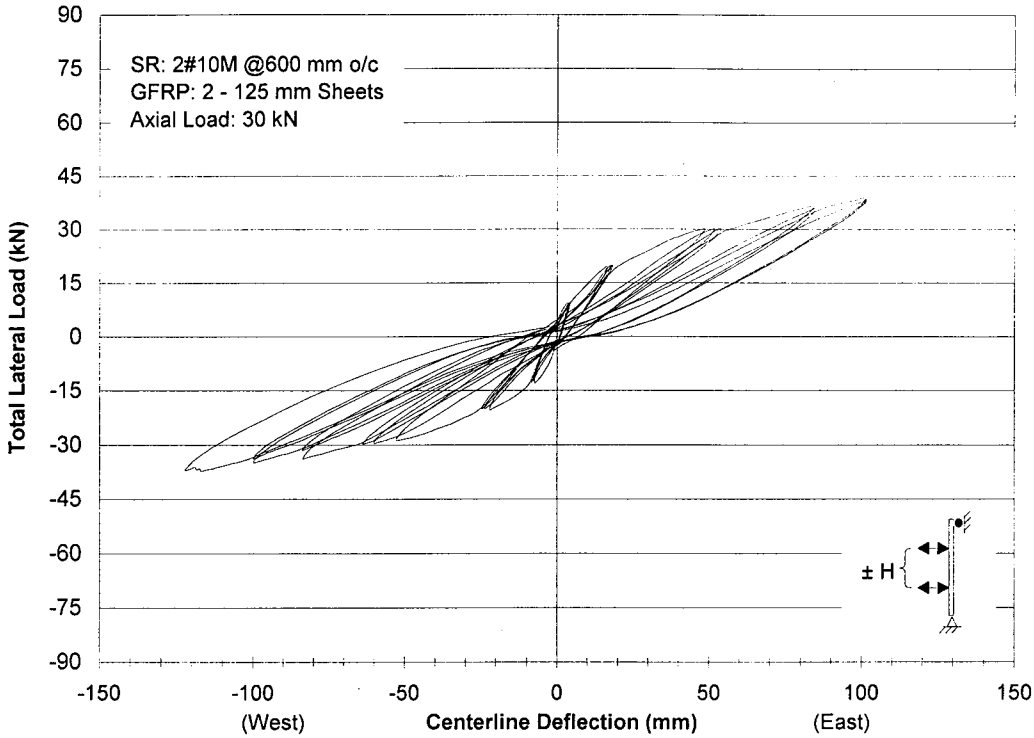

Figure 3.17 Load versus Deflection Hysteresis for Wall 3

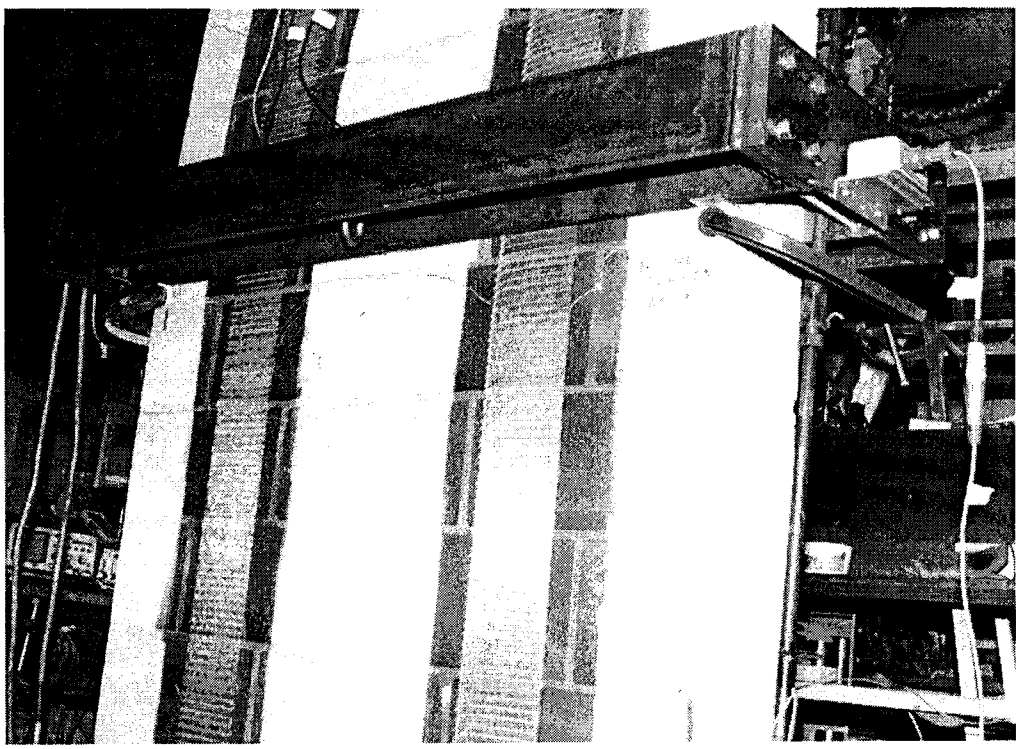

Figure 3.18 Failure Location of Wall 3

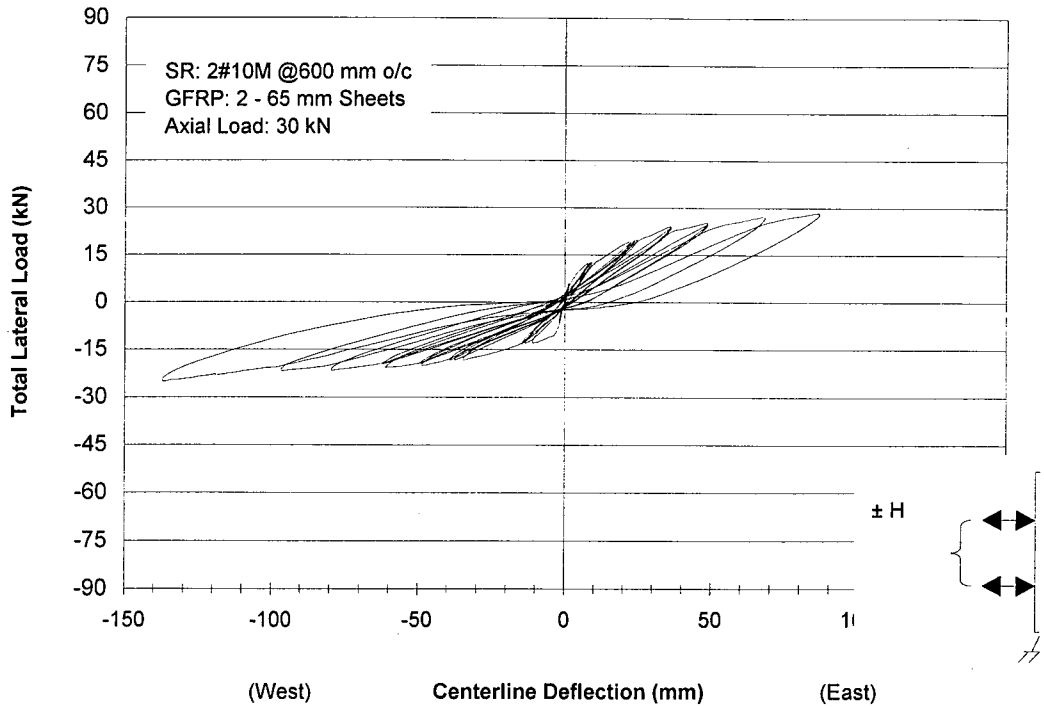

Figure 3.19 Load versus Deflection Hysteresis for Wall 4

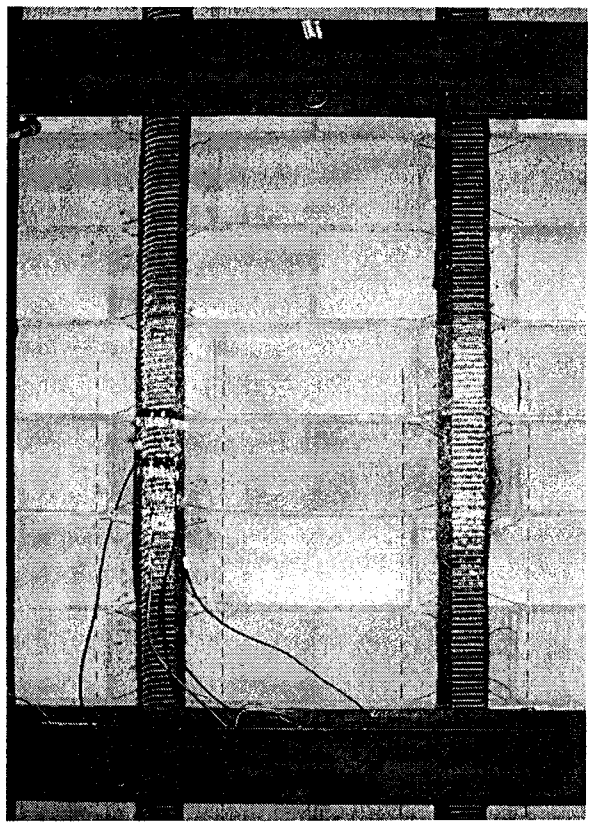

Figure 3.20 Diagonal Cracking of Masonry in Wall 4

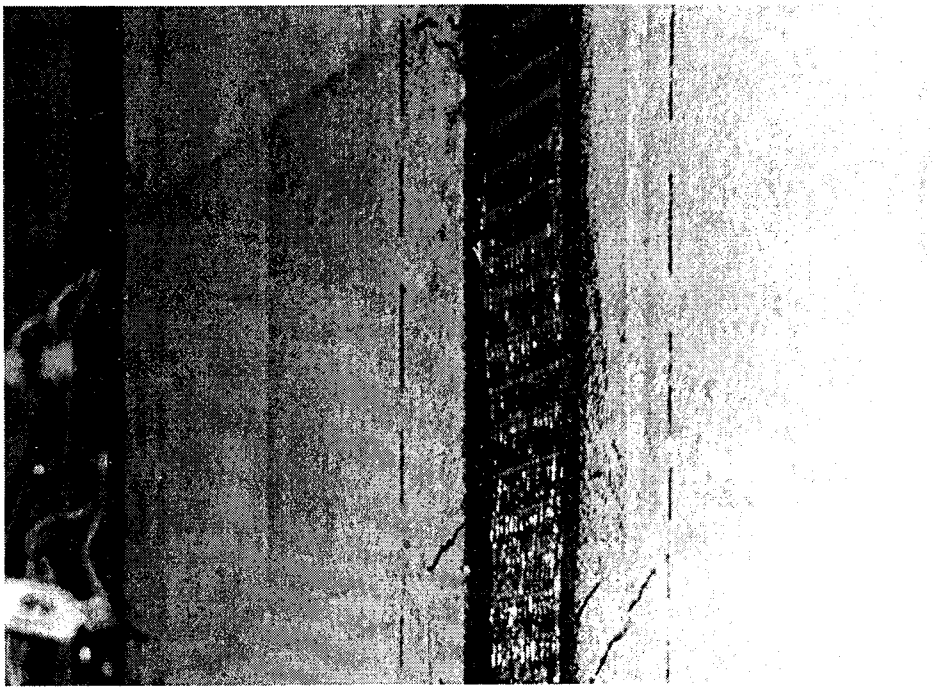

Figure 3.21 GFRP Buckling at Center-of-Block Location

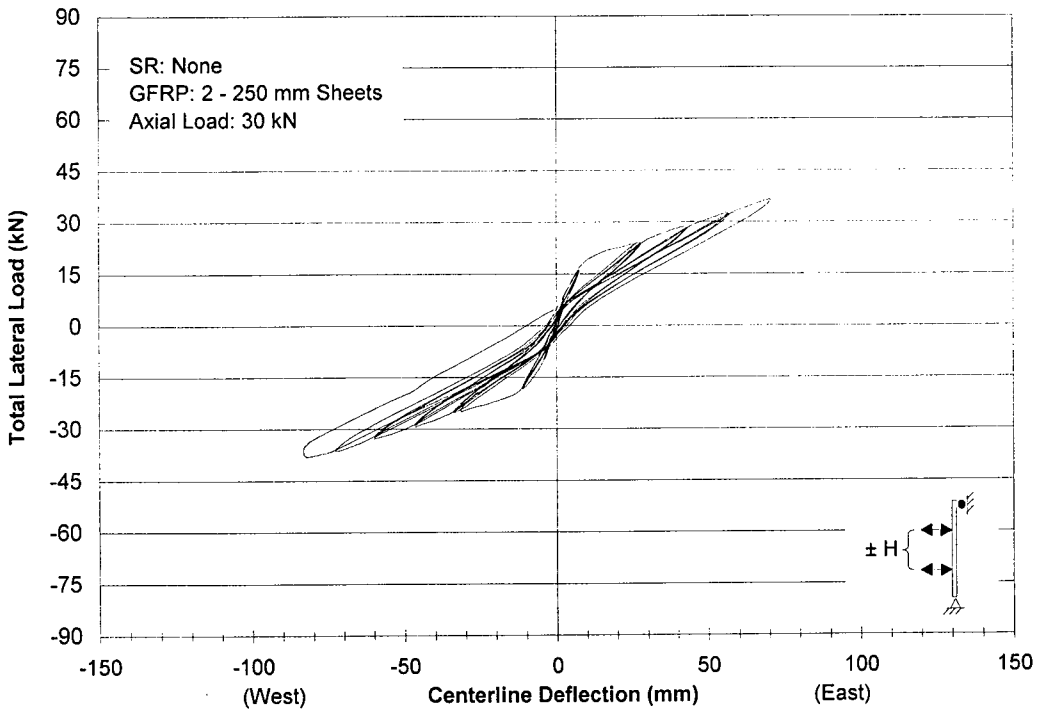

Figure 3.22 Load versus Deflection Hysteresis for Wall 2

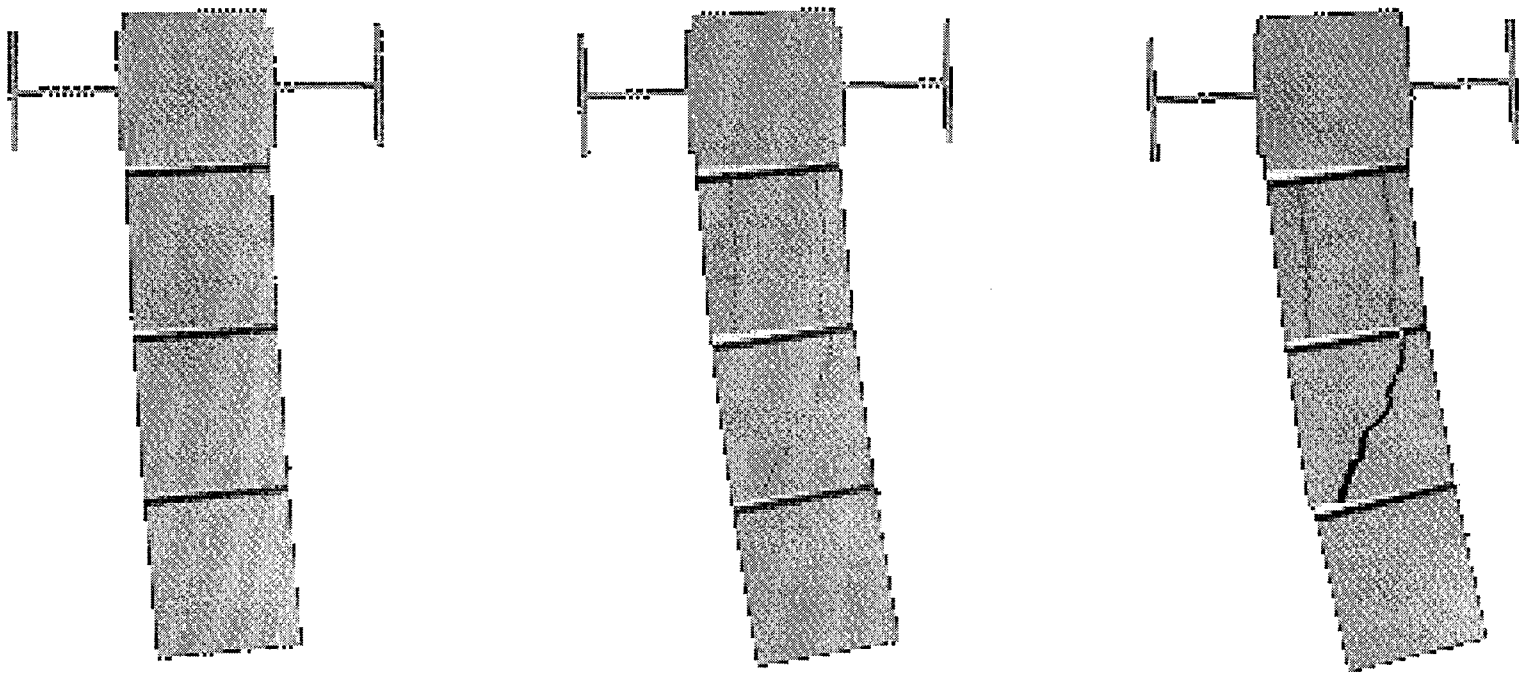

(a)
Mortar joints are slightly cracked

(b)
• Rigid-Body rotation of blocks
• Hairline cracks appear

(c)
Block splits and translates laterally

Figure 3.23 Progression of Flexure-Shear Failure Mode

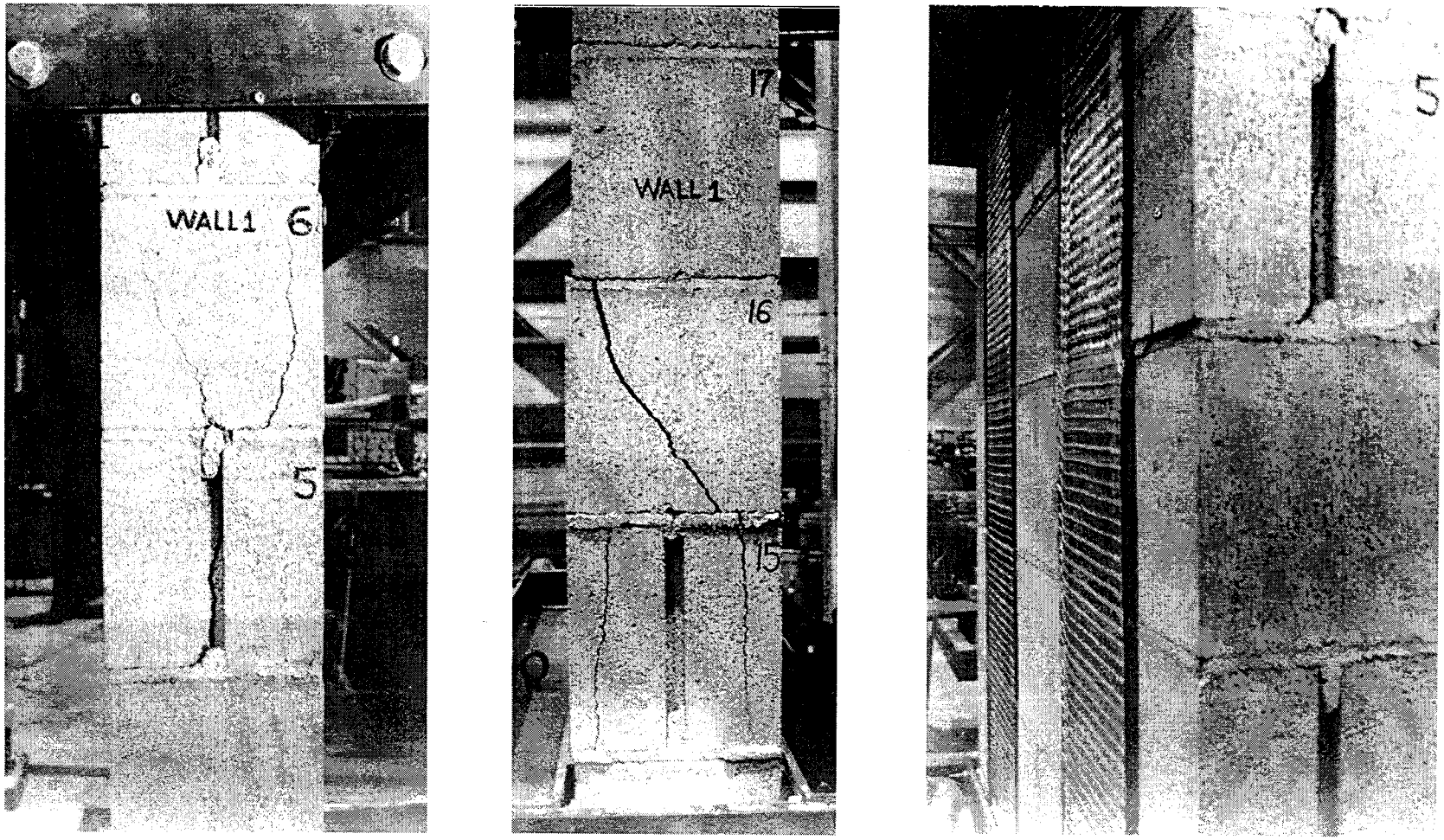

Figure 3.24 Actual Flexure-Shear Failure

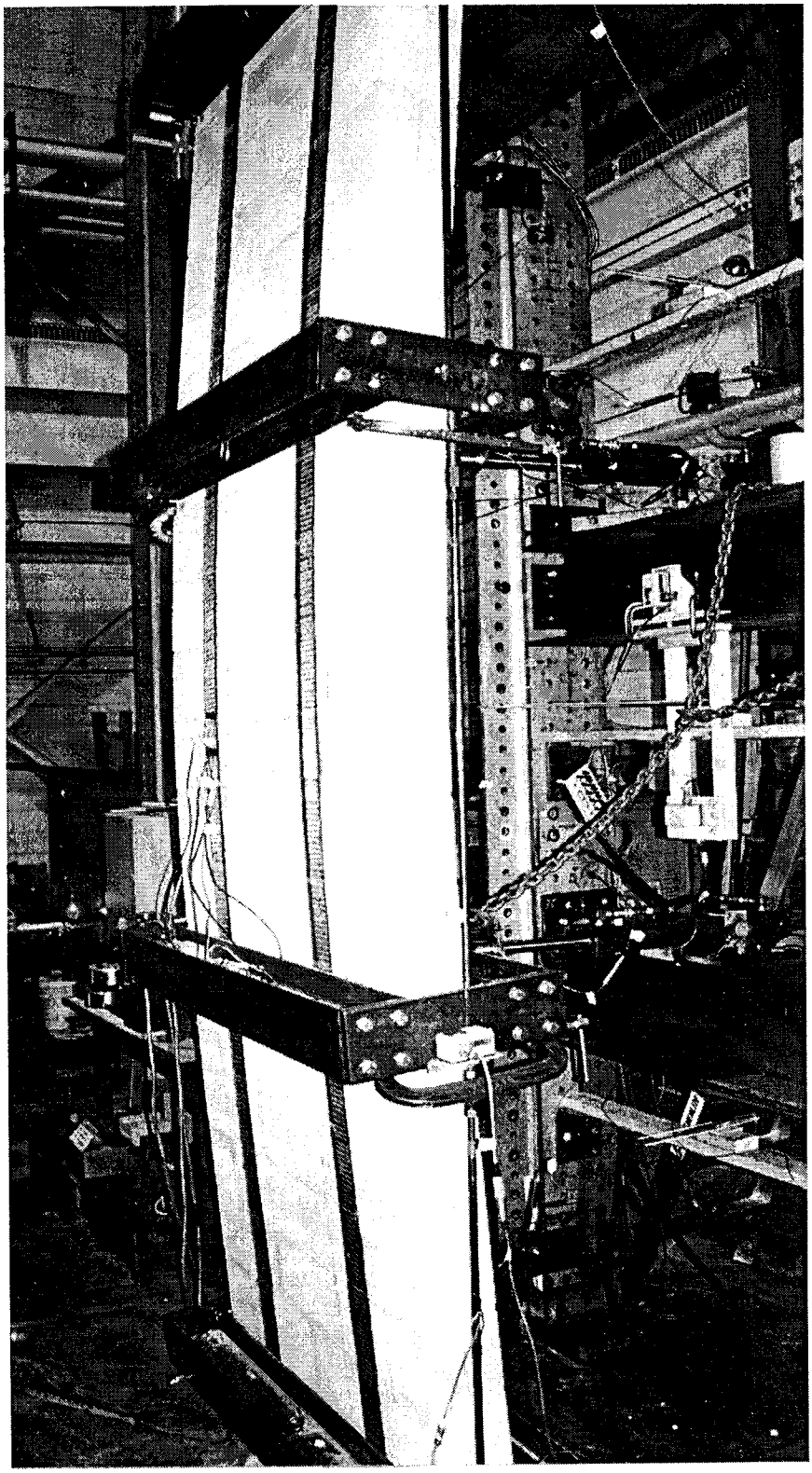

Figure 3.25 Wall Integrity Maintained at Large Deflections

4. RESULTS AND DISCUSSION

4.1 Introduction

In this chapter, the results from an examination of the test data are presented and discussed in detail. Of significant importance is the interpretation of the relationship between the out-of-plane bending moment versus centerline deflection hysteresis response. More importantly, the test results allow a deep insight into the physical behavior of the walls in response to the flexural loads. This behavior is objectively quantified through the observed strain history in both the GFRP and reinforcing steel. In Chapter 5, a mechanistic approach is proposed for predicting both strength and centerline deflection; thus, a complete bending moment versus deflection hysteresis loop response can be generated for of a wall with known geometry and physical material properties.

In assessing the out-of-plane behavior of any wall system, it is more appropriate to discuss bending moment versus deflection rather than lateral load versus deflection. The advantage of discussing bending moment versus deflection is that it accounts for the geometry, lateral loads, and axial loads within the system. The bending moment versus curvature, and thus stiffness, relationships is used indirectly later in Chapter 5 to determine the ultimate centerline deflection. The majority of the analysis presented here is in terms of bending moment and deflection as these are the most useful quantities when designing a wall system.

The bending moment versus deflection hysteretic response for walls reinforced externally with GFRP differs from typical walls reinforced internally with steel. The general shape of the loading region of the bending moment versus deflection envelope for walls containing both internal steel reinforcement and external GFRP is trilinear. As the amount of internal steel reinforcement is reduced to none, the envelope correspondingly reduces to a bilinear response. However, regardless of the loading profile, both systems exhibit a linear unloading response.

4.2 Qualitative Behavior

Before a complete mathematical analysis can be performed to quantify the flexural behavior, a qualitative understanding of the behavior is required. This section provides some insight into the physical behavior of the bending moment versus deflection response. The results shown in Chapter 3, Figure 3.10 for example, indicate that the nature of the GFRP reinforced masonry wall systems render an identical cyclic response in both directions of loading. In any one direction, the hysteretic response is bound by a well defined loading envelope containing a succession of almost linear, loading and unloading paths which gradually decrease in slope. Therefore, the response can be segmented into a loading envelope and unloading/reloading regions. Each is discussed in detail in the following sections.

4.2.1 Loading Envelope Response

One characteristic displayed in a typical hysteresis loop, Figure 3.10, of a GFRP reinforced masonry wall is that it has a pinched nature. The result of this is a relatively indistinguishable difference between the loading envelopes from a cyclically loaded specimen and that from a virgin specimen loaded monotonically such as that reported by Albert *et al.* (1998). Assuming the response starts at the origin, it proceeds through a series of regions up to the point of failure. These regions can be characterized as either *Bilinear* or *Trilinear* depending on whether the wall contains steel reinforcement. However, both terms are in fact misnomers since the different linear regions are separated by slightly nonlinear transition regions.

Figure 4.1 shows a generic bilinear loading response of a bending moment versus deflection envelope which occurs for walls with external GFRP reinforcement and no internal steel reinforcement. This response envelope can be described by six distinct points represented by the letters *A* through *G* in Figure 4.1. Point *A* is simply the origin and defines the state of both zero bending moment and deflection. Point *B* describes the cracking moment (M_{cr}) and its corresponding deflection. The response is linear between the origin and point *B*. When cracking occurs at point B, a slight degradation in stiffness

occurs resulting in a slight change in slope of the response. A new term called the *transition moment* (M_T) is defined by point *C*. The slope from point *B* to *C* is also linear with a slightly reduced slope from the region defined by points *A* to *B*. However, this reduction in stiffness is very small and thus the response can be simplified by neglecting point *B* and directly connecting point *A* to point *C*. From point *C* to *D*, a nonlinear region exists and is defined as the *transition zone* where the slope of the response decreases at a relatively constant rate throughout. The ultimate failure moment and the corresponding deflection define point *F*. The response from the end of the transition zone, point *D*, to point *F* again follows approximately a linear path. The unloading path from point *F* to *G* is closely approximated by a linear path to point *G*. However, point *G* is very close to the origin as indicated from the raw data plots of lateral load versus deflection presented in Chapter 3; and thus, connecting points *F* and *A* together is a good conservative approximation for the unloading branch.

For wall specimens that contain both internal steel reinforcement and external GFRP, the loading behavior is slightly modified from the previous description of the bilinear response. In the description of the bilinear response, point *E* was purposely not included as the bilinear behavior is simply a special case of the trilinear loading behavior. Figure 4.2 schematically shows the trilinear bending moment versus deflection loading behavior. With the addition of reinforcing steel to the wall, point *E* is introduced between points *D* and *F* where a slight reduction in the slope was observed. Note that the response is still linear from points *D* to E and points *E* to *F*. Other than the addition of point *E*, the points defining the trilinear response are the same as in the bilinear response.

To understand the mechanisms affecting the shape of the bilinear and trilinear loading envelopes, both the GFRP strains and the steel reinforcement strains are analyzed. Figures 4.3, 4.5, and 4.7 show the west portion of the bending moment versus deflection hysteresis from Walls 2, 1, and 4 while Figures 4.4, 4.6, and 4.8 show the corresponding GFRP and steel reinforcement strains versus bending moment for the respective walls. These specimens were chosen as a representative sample because Wall 2 had no internal steel reinforcement and walls 1 and 4 had the most and least amount of external GFRP respectively. In Figures 4.4, 4.6, and 4.8, the terms "joint" and

"block" in the legends refer to strains measured in the vertical direction at the location of either a bed joint or the center of a concrete block at the tenth course elevation.

Up to point *E*, both the bilinear behavior and the trilinear behavior are the same; thus, the discussion will begin with Wall 2 that had no steel reinforcement, Figures 4.3 and 4.4. Upon initial loading, the slope from the origin to the cracking moment, point *B*, is taken as the gross moment of inertia since the section is largely uncracked. The next key point is the transition point which only occurs in walls with external GFRP. Or rather, for walls with no GFRP, the transition point is equal to the cracking moment. The addition of the external GFRP has the effect of modifying the section modulus immediately after first cracking occurs. This effect acts to maintain the integrity of the cross section and thus only a slight reduction in the moment of inertia is noticed at first cracking. The transition point is simply a linear function of the cracking moment which can be viewed as a delayed cracking moment. Notice that both the GFRP joint and block strains in Figure 4.4 are very small until about 4 kNm at which point the joint strains begin to increase rapidly.

Wall 2 appears to behave linearly up to about 8 kNm at which point the curve begins to decrease in slope. With increasing moment, the tensile force and thus strains in both the GFRP and masonry increase. Since masonry walls can only tolerate a few hundred microstrain in tension at the weakest tensile region, the interface between blocks and mortar in the bed joints, small cracks progressively form at these interfaces during loading from point *B* to point *C*. As loading continues beyond the transition moment, cracks at the bed joint-block interface increase in addition to strains in the GFRP. The cracks in the bed joints relieve the tensile strains in the face shell region of the blocks at locations away from the bonded GFRP strips.

In region *C* to *D*, the large discrepancy in strain between the face shell of the masonry immediately bonded to the GFRP strip and the rest of the face shell, induces a shear strain field in the face shell evidenced by diagonal cracks in the face shell. The diagonal cracks are followed by horizontal cracks across the face shell itself. This phenomenon was reported by Albert *et al.* (1998). Figure 3.20 shows this typical crack pattern.

The successive appearance of the shear lag cracks allows more of the GFRP to directly experience strains that are larger than those normally tolerated by the blocks behind and adjacent to the GFRP. Thus, as more of the GFRP is gradually "mobilized" due to progressive shear lag cracking, the slope in region C to D decreases. This increase in GFRP mobilization is analogous to a *system of rigid bodies connected by linear springs*. Initially when only the bed joints are cracked, an appropriate model is a system having an initial total length L which consists of two rigid bodies connected by a spring. If a tensile load P acts on the system, an elongation of δ will occur. When one crack in the masonry occurs, the model changes slightly to include two springs and three rigid bodies while still maintaining a total initial length L. If the same load P acts again, the elongation of the system will increase to 2δ. This trend continues until a sufficient level of cracking within the face shell of the masonry exists to permit the entire length of the still bonded GFRP strip to carry a large tensile force. Figure 4.9 illustrates this analogy. It must be emphasized that the GFRP stiffness does not change. Rather, more GFRP is mobilized and thus the stiffness of the masonry/GFRP system decreases. In terms of the analogy above, longer and longer springs with the same spring constant are continuously substituted into the system.

At point D, the rate of increase in GFRP strain at the center-of-block location is approximately equal to the rate of increase in GFRP strains at the bed joint location. This is clearly shown in Figures 4.3 to 4.8. At this point, a sufficient level of cracking has occurred to stabilize the interaction between the GFRP and the masonry on the tension face. Hence, the rest of the behavior up to failure is dominated by the GFRP on the tension face, which behaves linearly elastic to rupture, and by plastic strains within the bed joint on the compression face.

Comparing the transition zone in Figure 4.3 to those in Figures 4.5 and 4.7, both the length of the zone and the rate of change of slope are affected by the presence of internal reinforcing steel and the amount of external GFRP. To explain this, the interaction between the masonry and GFRP must be understood. Under large deflections, masonry walls with no external GFRP act like a series of rigid bodies connected by a tension tie, the steel reinforcement, in the center of the block. Thus, the majority of the tensile strains are concentrated at the bed joint location resulting in wide cracks. The face shell

on the tension face typically has very low tensile strains and thus cracks to a lesser extent. With the addition of external GFRP, the system is forced to behave more as a continuum rather than a series of rigid bodies. Thus, the masonry and GFRP work against each other. When a crack occurs at the joint level, the external GFRP must accommodate the magnitude of the crack width in the form of a distribution of strain. If the GFRP was not bonded to the wall, the strain would be uniform throughout the entire length of the GFRP. However, once bonded to the masonry, the strain in the GFRP can only achieve a uniform distribution if either the bond strength between the two materials is exceeded, or the masonry face shell experiences progressive shear lag cracks as described above. Since the epoxy bond strength between the aggregate and the GFRP is greater than the tensile rupture strength of the masonry, the masonry is forced to crack. Thus, the extent of grouting has the effect of changing the area of masonry in tension which alters the magnitude of the force transfer from the GFRP to the masonry that is required to crack the masonry. This interaction between the masonry and the GFRP is analogous to the shear lag phenomenon in a bolted steel connection or the development length required in reinforced concrete members.

For walls with internal steel reinforcement in addition to external GFRP, the system behaves slightly differently after point *D* due, solely, to the presence of the steel. Figures 4.5 and 4.7 in conjunction with Figures 4.6 and 4.8 indicate that point *E* occurs when the reinforcing steel yields. Thus, up to point *E*, the tensile component of the internal moment resisting mechanism consists of both the GFRP and the steel reinforcement. Once the steel yields, the tensile force in the steel remains constant, determined by the yield stress, while the tensile force in the GFRP continues to increase. Hence the slight decrease in slope at point *E*. Beyond point *E* to failure at point *F*, the envelope remains linear as the GFRP and the compression face shell dominate the behavior.

4.2.2 Unloading/Reloading Region

The remaining region of the bending moment versus deflection envelope is the unloading/reloading from/to point *F* to *G*. The linear behavior of this region is totally controlled by the GFRP which results in a very predictable and well defined pattern. As

the GFRP remains linearly elastic until rupture, the GFRP always unloads back to zero strain with no permanent deformation. Thus, upon unloading, the GFRP fully closes all the cracks formed when the masonry was in tension. Since the GFRP is always bonded to the extreme tension face, the neutral axis remains closer to the geometric centroid throughout the cyclic loading history resulting in lower strains in the steel reinforcement. Limiting the steel strains to values less than the yield strain for many cycles also results in the steel behaving elastically. The benefit of both tensile resisting mechanisms remaining elastic during cyclic loading is very little loss of the system's integrity.

If the system's integrity is maintained, then after unloading, the following reloading cycle occurs, more or less, along the previous unloading path. This behavior is well defined and thus, it can be easily and accurately predicted. Figures 4.10 through 4.18 show the complete bending moment versus centerline deflection hysteresis for all the walls tested. As seen in these figures, some damage does occur to the walls throughout the loading history as the unloading branches do not pass through the origin. This slight progressive lateral shift of the unloading branches indicates that some minor plastic behavior is occurring. Typically, these displacements range from a few percent of the ultimate displacement during the initial cycles to a maximum of seventeen percent of the ultimate displacement for the final cycles. As the GFRP to steel reinforcement ratio is reduced, this plastic behavior tends to increase as seen when Figures 4.10, 4.12, and 4.13 are compared. However, in predicting the unloading behavior, a very simple and conservative approach is to assume a linear path between the maximum point experienced in the load history to the origin.

4.3 Testing Parameters

The parameters investigated in this program were the amount of steel reinforcement, amount of GFRP, and level of axial load. Figures 4.19, 4.20, and 4.21 show a comparison of the moment versus deflection envelopes for each of the parameter groups respectively. From the three figures, the only parameter which significantly altered the behavior was the amount of GFRP shown in Figure 4.20. Three noticeable

effects occurred as the amount of GFRP was reduced while both the amount of steel reinforcement and level of axial load remained constant.

First, two of the effects can be quantified together. Both the transition moment and the ultimate moment were progressively reduced as the amount of GFRP was reduced. As the area of the GFRP is reduced, so is the internal tensile force provided by the GFRP to balance the forces within the cross-section during flexural loading. Since the internal moment arm of the GFRP is more than double the internal moment arm of the steel reinforcement, the resisting moment of the section is more sensitive to GFRP force component. When initial cracking occurs, strains are mobilized only in a highly localized region of the GFRP directly adjacent to the crack. This can be quantified in terms of average strain across the width of the GFRP. As the amount of GFRP is reduced, the average strain increases for a given moment, thus requiring the crack width to become larger. Hence, the transition moment reduces as a result of the decreasing ability of the GFRP to prevent crack propagation. At the ultimate moment condition, the reinforcing steel has yielded and thus its contribution towards equilibrium of the internal forces is constant. Since the GFRP remains linearly elastic until it ruptures, the GFRP internal force contribution is directly proportional to its area. The ultimate moment is, thus, controlled by the maximum force mobilized in the GFRP, which decreases as the area decreases.

The third behavioral difference is the stiffness after the transition moment. This is a direct effect of the cross-sectional properties, namely the cracked moment of inertia. In calculating the cracked moment of inertia about the centroid of the cross-section, only the tension GFRP and the masonry above the neutral axis contribute significantly. As the crack depth increases, the contribution of the masonry towards the moment of inertia reduces, whereas the contribution from the GFRP remains constant while the arm length increases. Thus, the effective cracked stiffness of the cross-section depends heavily on the amount of GFRP.

For the wall specimens fit with either 130 mm wide or 250 mm wide GFRP sheets, only limited buckling of the GFRP occurred at the bed joint locations. This typical behavior is illustrated in Figure 3.9. However, as shown in Figure 3.22, the buckling of the 65 mm wide GFRP sheets occurred over the center of the masonry blocks, not over

the bed joints. As discussed in Section 4.2.1, the progressive cracking of the masonry is a result of the internal force interaction between the GFRP and the masonry. The critical link between the GFRP and the masonry is the bond provided by the epoxy. For the two wider GFRP sheets, the shear stress developed between the GFRP and the masonry does not exceed the epoxy bond stress. Rather, the masonry tensile strength is first exceeded resulting in the masonry cracking before debonding of the GFRP occurs. Conversely, for the narrow GFRP strips, an insufficient bond width/area is provided to transfer the tensile forces from the GFRP to the masonry at the center-of-block location. The GFRP remains bonded to the masonry just adjacent to the bed joints as the diagonal cracks, as shown in Figure 3.21, in the masonry form at much lower GFRP tensile forces than is required to crack the masonry units horizontally at the center-of-block location. Hence, the epoxy bond strength is exceeded in the center-of-block regions but not exceeded adjacent to the bed joint locations. In qualitatively assessing the force transfer between the both the GFRP and steel reinforcement and the masonry, insight is provided by the strain profile for each reinforcement type. For each wall specimen, GFRP strains versus bending moment are shown in Figures 4.22 through 4.24, and the steel reinforcement strains versus bending moment are shown in Figures 4.25 through 4.27.

4.4 Measurement of Curvature

Using the experimental data obtained from the deflected shape, an attempt was made to directly compute the curvature and thus stiffness of the walls. The technique used was a Polynomial Least Squares Fitting to fit five lateral deflection points within the zero shear span to a second-order parabola. The matrix method used is included in Appendix A. By fitting a second-order parabola to five data points, the sensitivity of any one data point is reduced. Once the coefficients have been obtained, the second derivative of the second-order function is taken which is the curvature. Knowing the corresponding bending moment, the effective stiffness can be calculated through simple algebra.

This technique proved only partially successful. At small lateral deflections, typically up to 5 mm at the centerline, the results from this technique proved to be highly

sensitive to small errors in the deflection measurements. A measurement error of 0.5 mm can alter the curvature by an order of magnitude. This was the case within this research program. Of the five deflection points sampled within the zero shear span, each of the end deflections was measured through the corresponding LVDT monitoring the stroke of each jack. The three measurement points used between the two end points were connected directly to the masonry wall. After analyzing the data, highly erratic stiffness results appeared for small deflections. The tolerances were then checked on the loading frame and were approximately determined to be a maximum of 0.7 mm. This "slop" in the systems was determined by measuring the pin tolerances, about 0.2 mm, and estimating the foam compression for both the reaction and loading beams at 0.25 mm. Thus, the deflection measurements made at each end of the zero shear span had much greater error than the three measurements made between the end measurements. Hence, the deflection data obtained at small deflections did not provide stable results. However, for large lateral deflections, the stiffness calculations were not sensitive to the small measurement errors and thus the results were stable. Because the exact measurement error was not known, this technique was not used to determine the stiffness.

A simple fix to this problem would be to substitute additional measuring devices for the LVDTs monitoring each ram. The new devices should be attached directly to the masonry wall just above and below the lower and upper loading beams respectively. This would render all the monitoring of deflection data within the zero shear span independent of the jack strokes and thus the associated "slop" in the system.

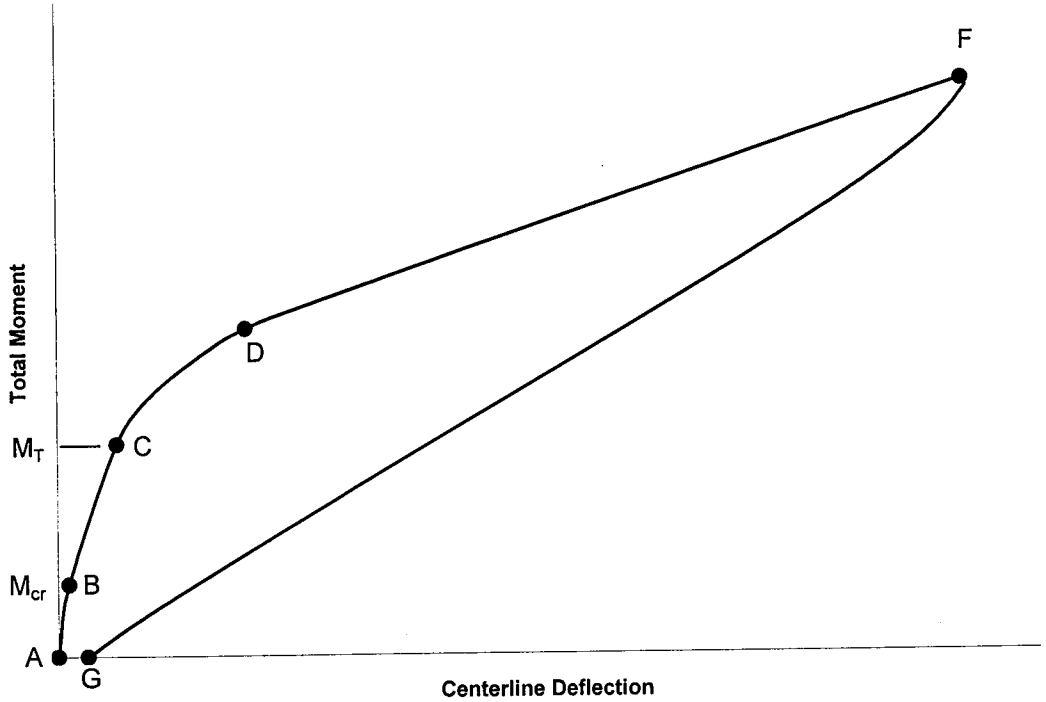

Figure 4.1 Bilinear Hysteretic Behavior

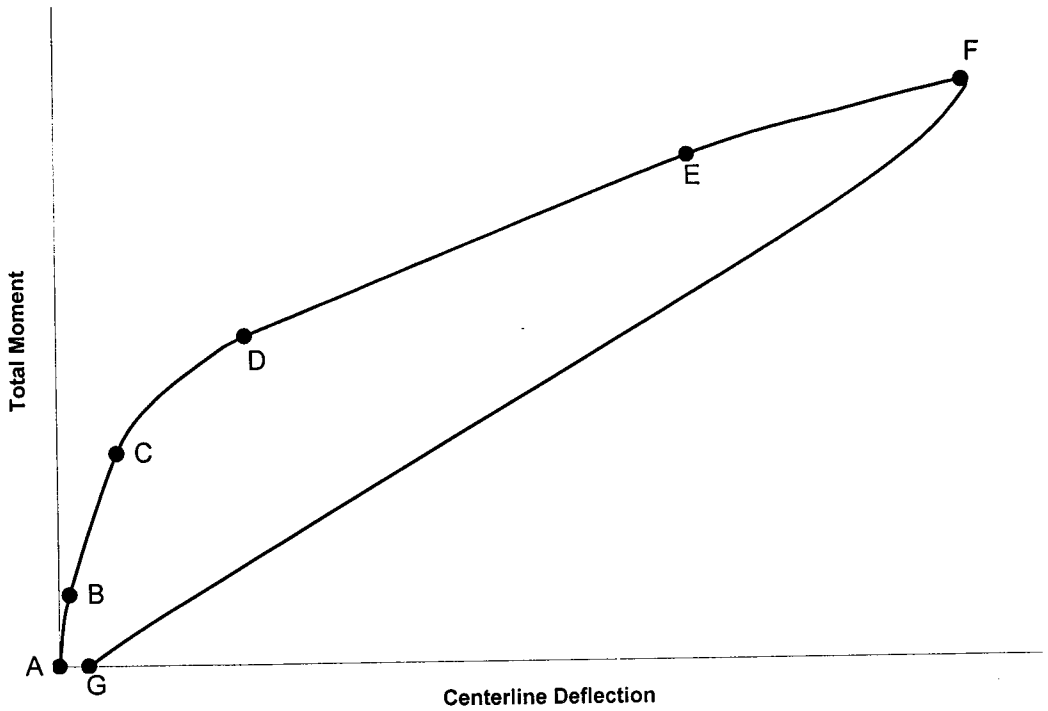

Figure 4.2 Trilinear Hysteretic Behavior

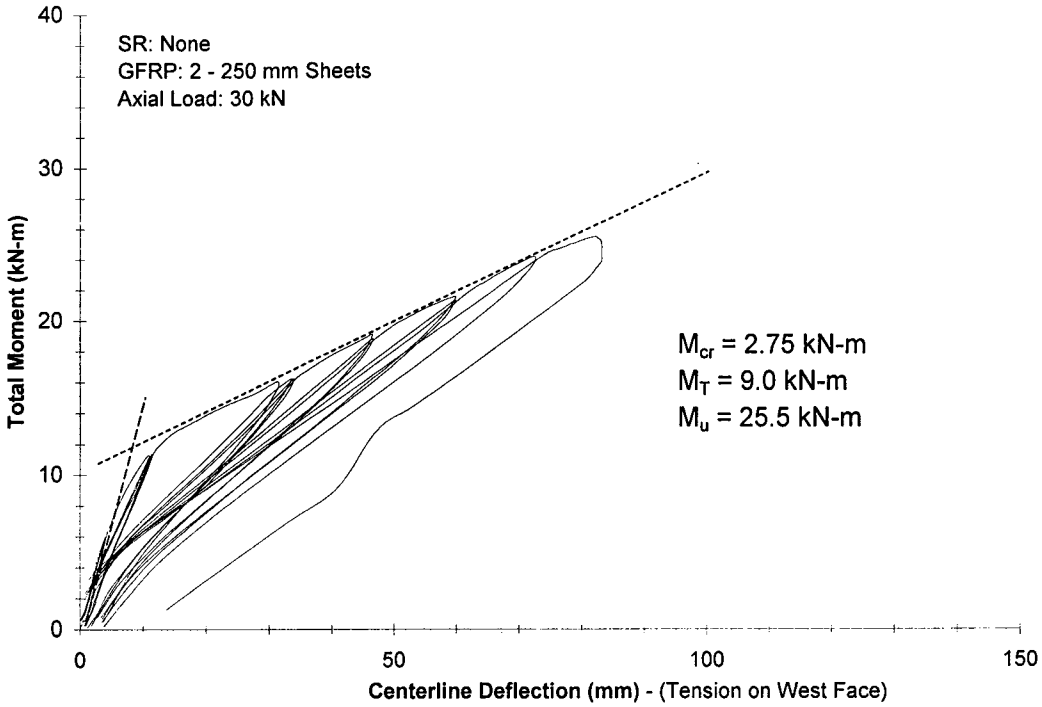

Figure 4.3 Moment versus Deflection Hysteresis for Wall 2

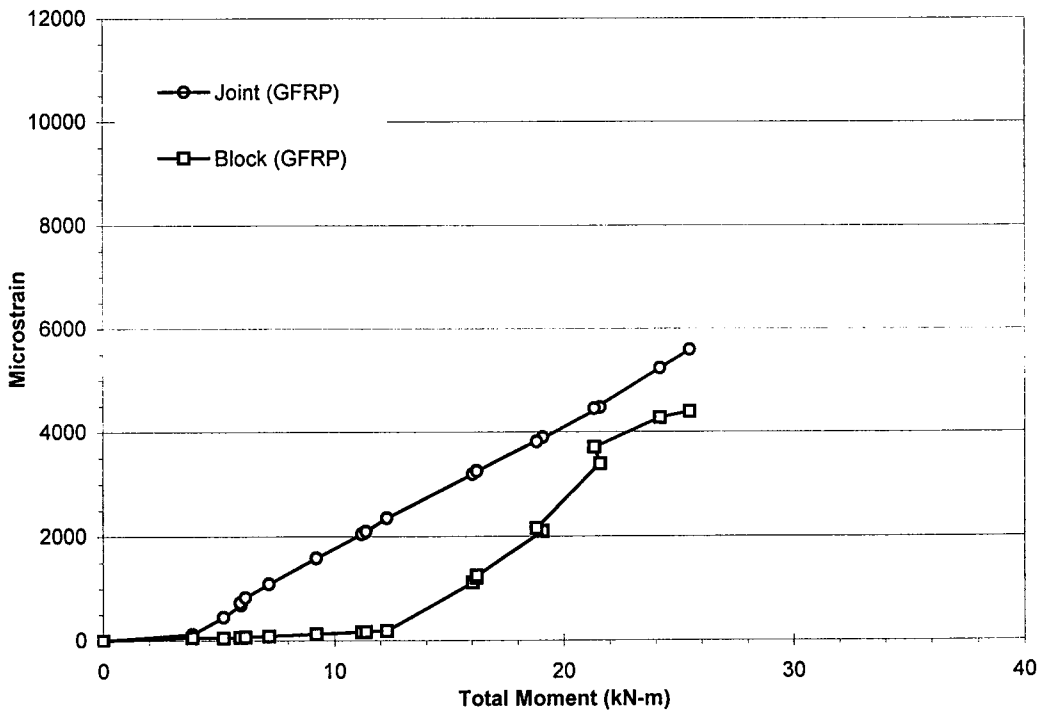

Figure 4.4 GFRP Strains versus Moment for Wall 2

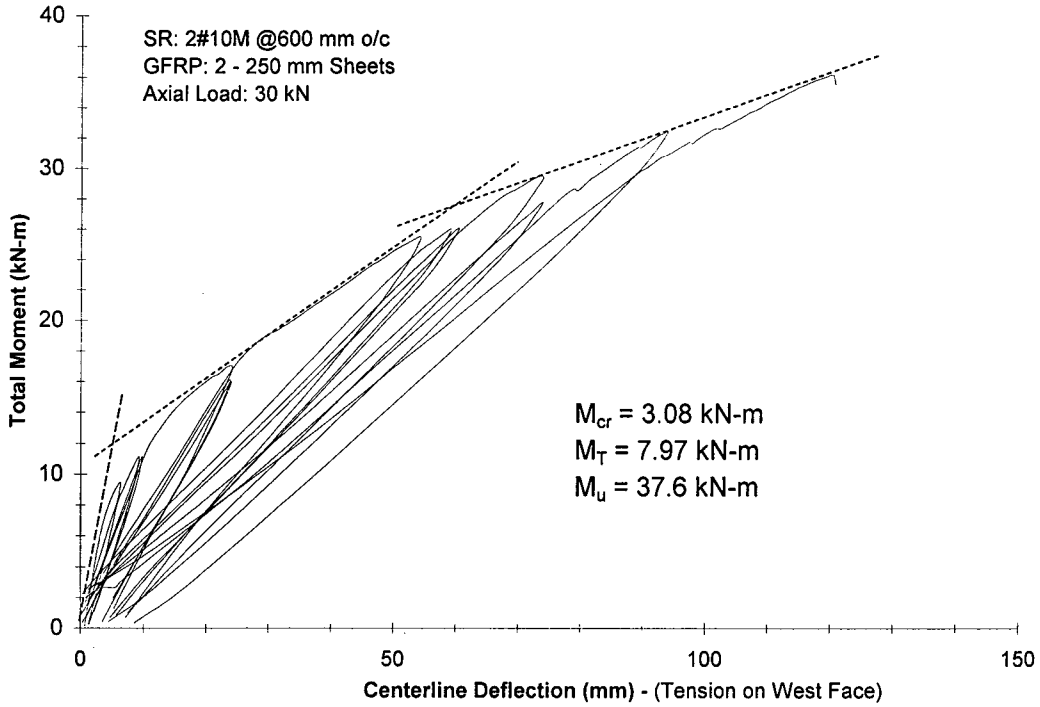

Figure 4.5 Moment versus Deflection Hysteresis for Wall 1

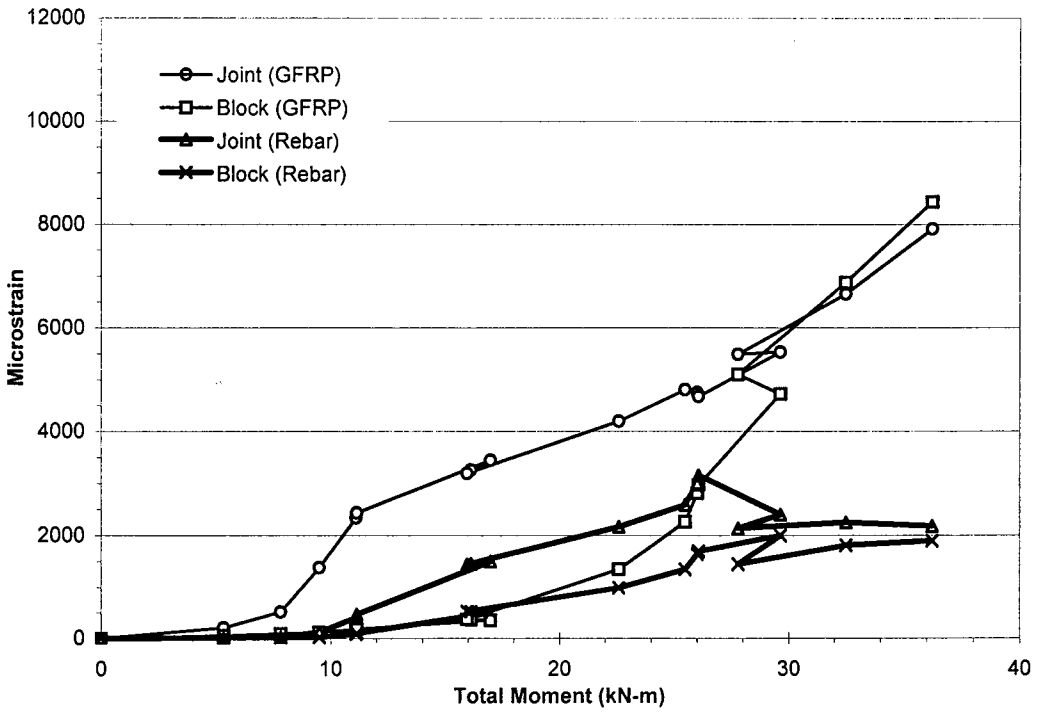

Figure 4.6 GFRP and Rebar Strains versus Moment for Wall 1

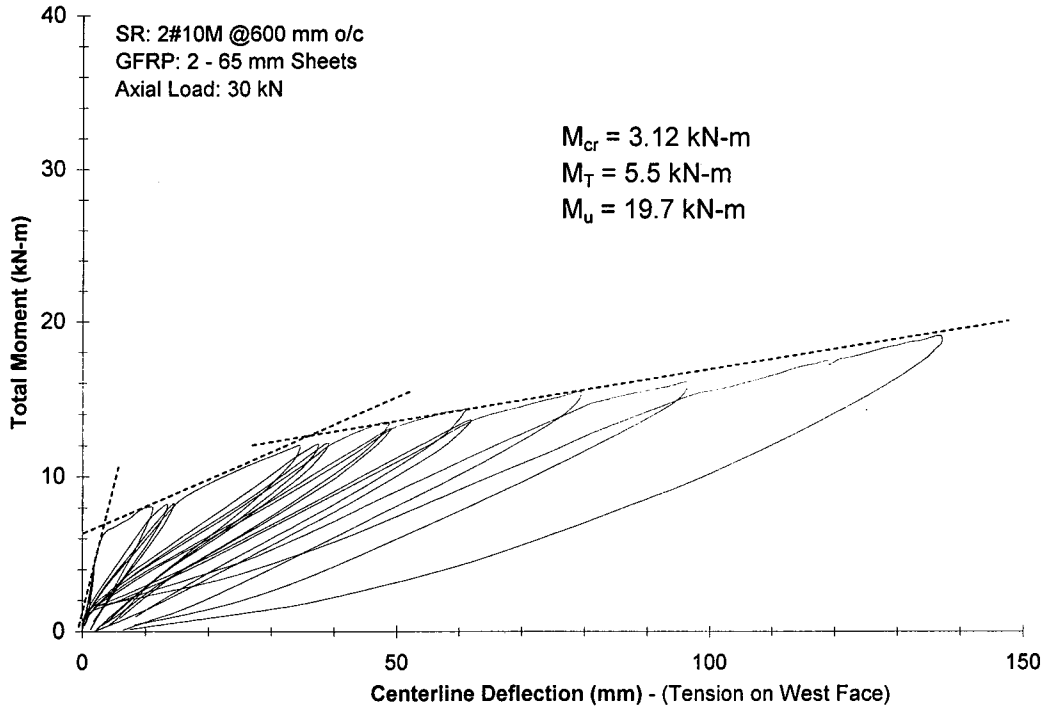

Figure 4.7 Moment versus Deflection Hysteresis for Wall 4

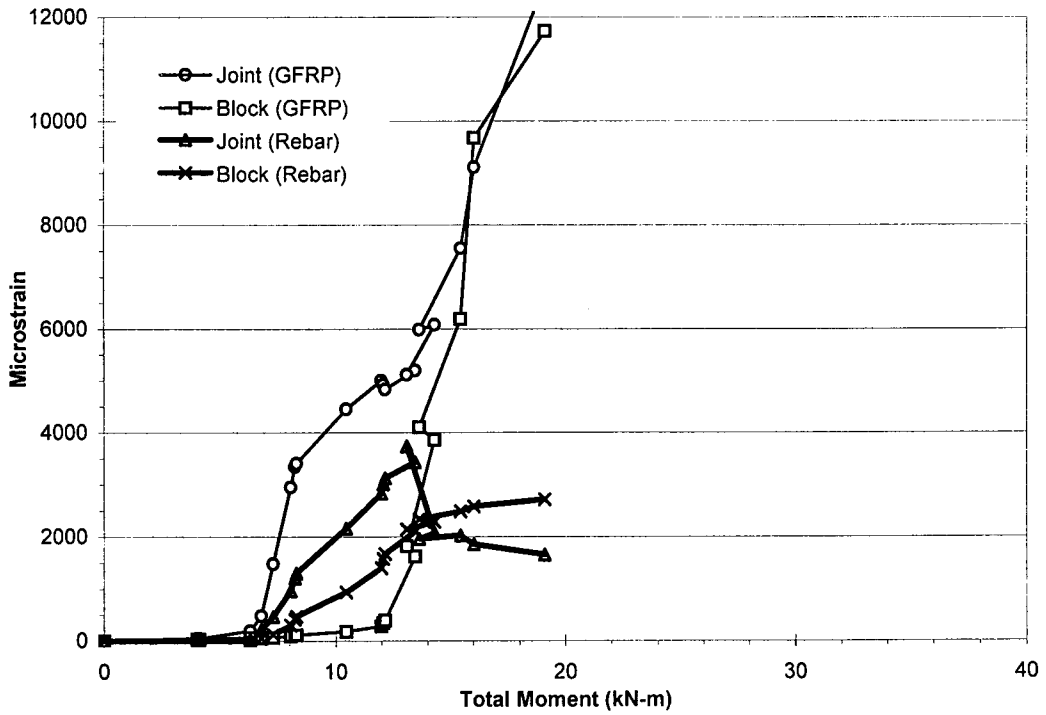

Figure 4.8 GFRP and Rebar Strains versus Moment for Wall 4

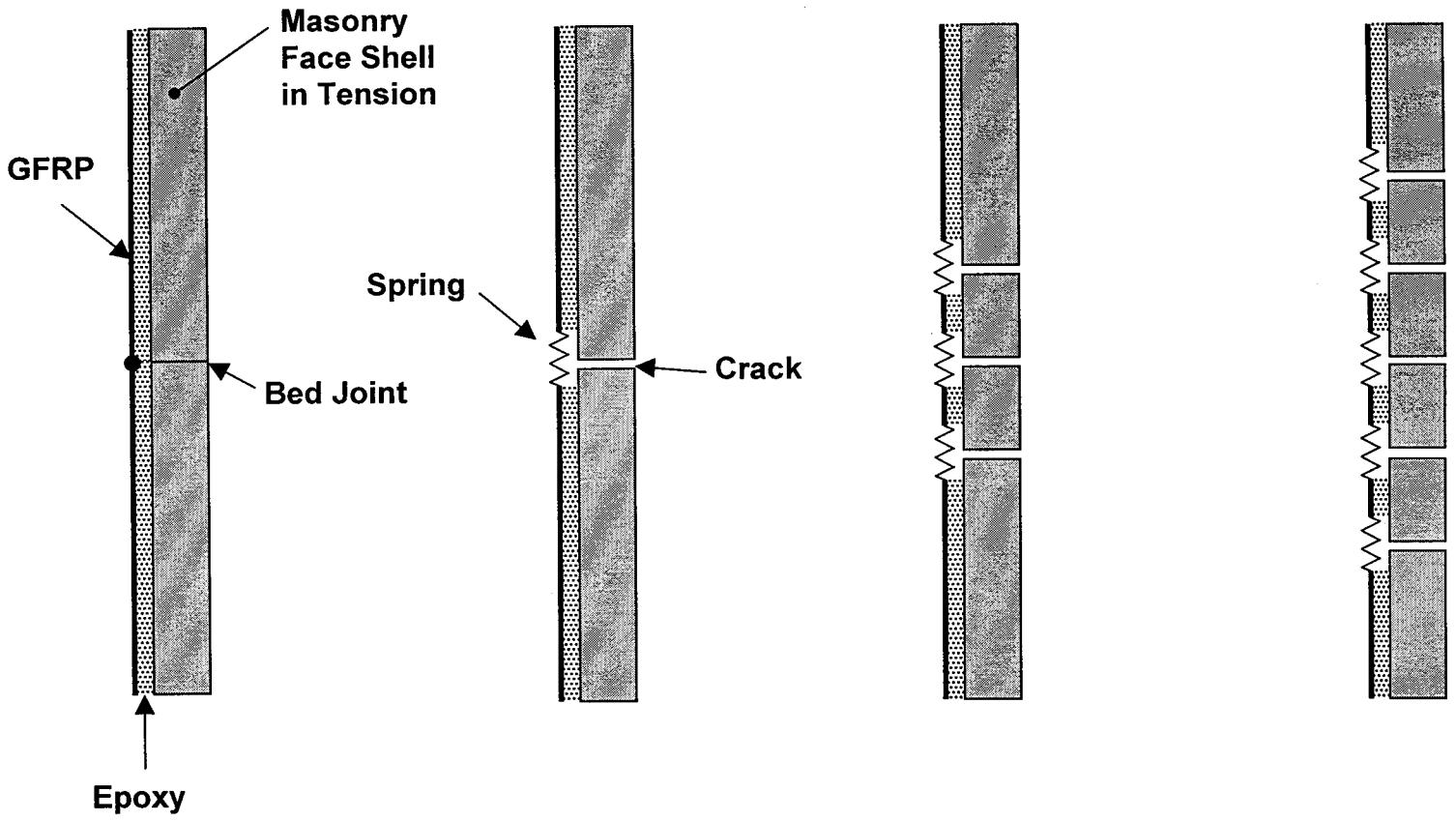

Figure 4.9 Spring Analogy for GFRP Strain Mobilization

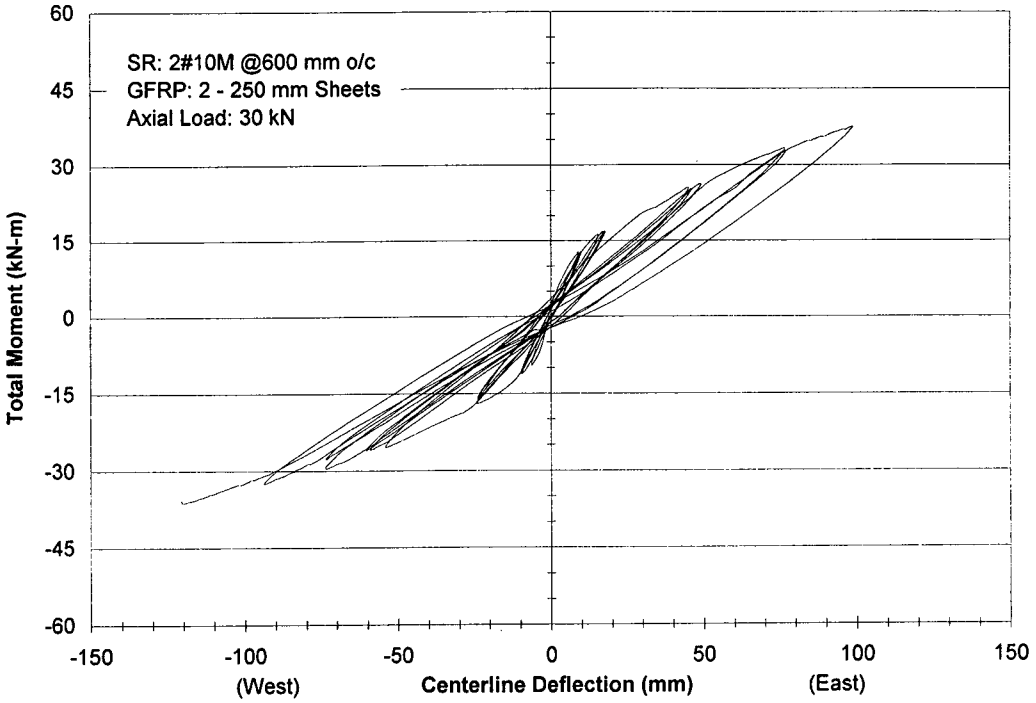

Figure 4.10 Moment versus Deflection Hysteresis for Wall 1

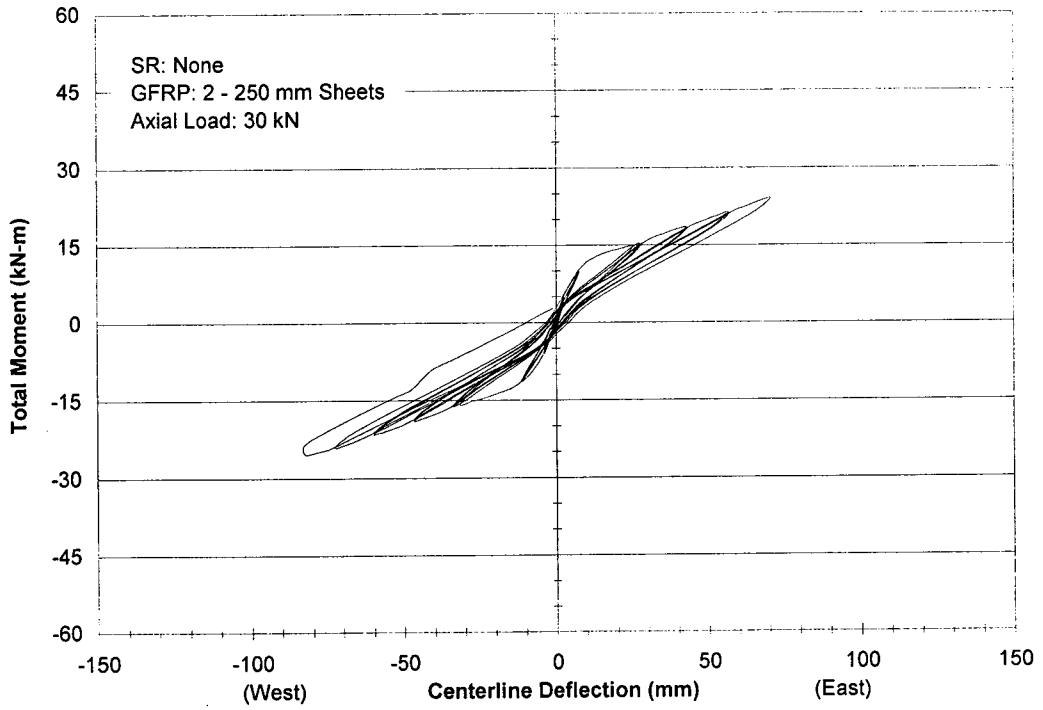

Figure 4.11 Moment versus Deflection Hysteresis for Wall 2

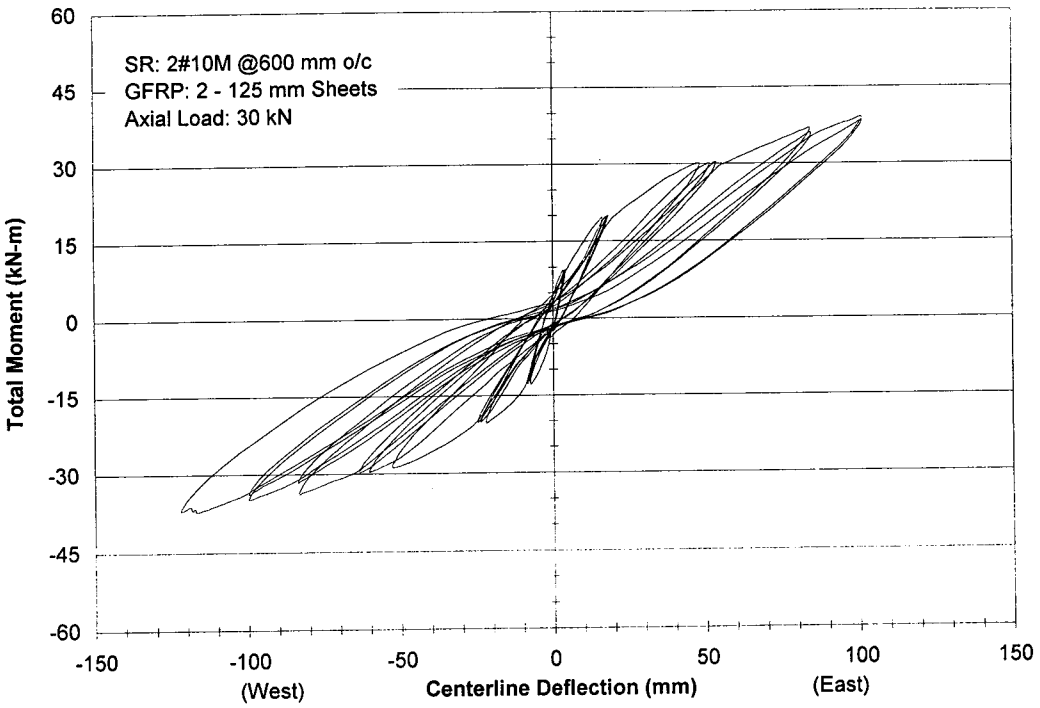

Figure 4.12 Moment versus Deflection Hysteresis for Wall 3

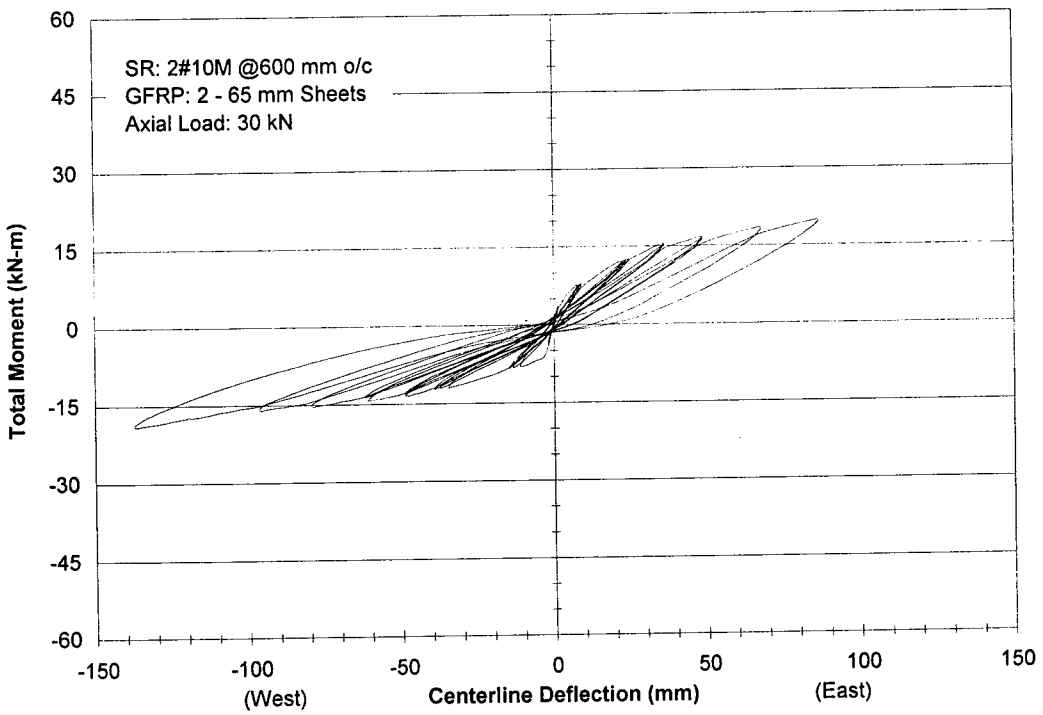

Figure 4.13 Moment versus Deflection Hysteresis for Wall 4

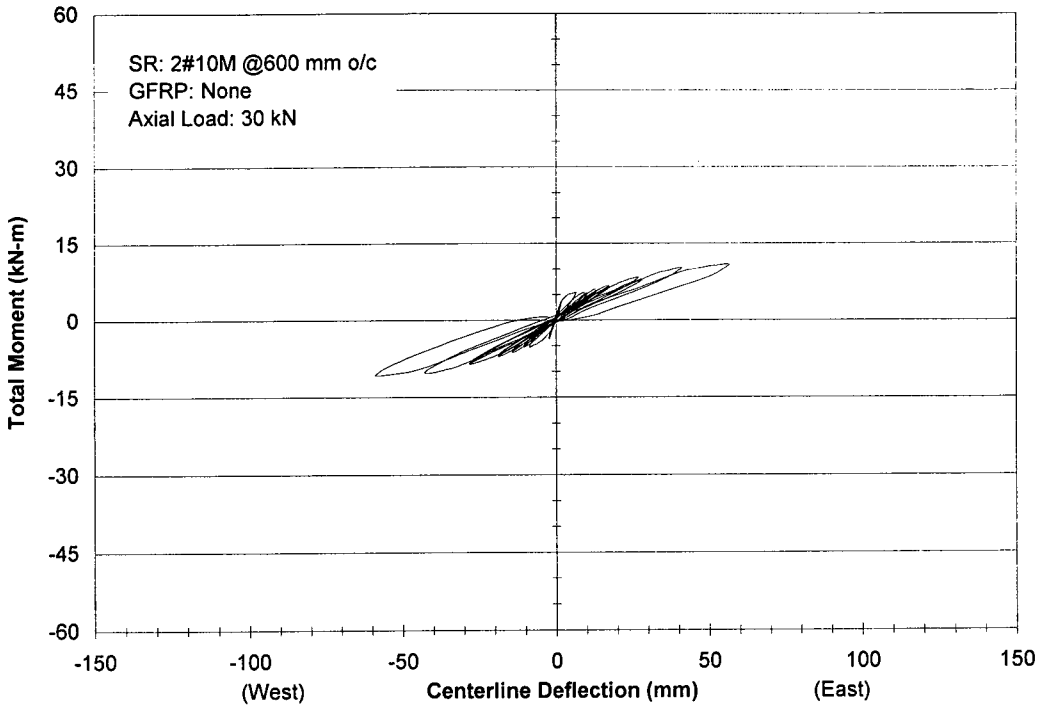

Figure 4.14 Moment versus Deflection Hysteresis for Wall 5a

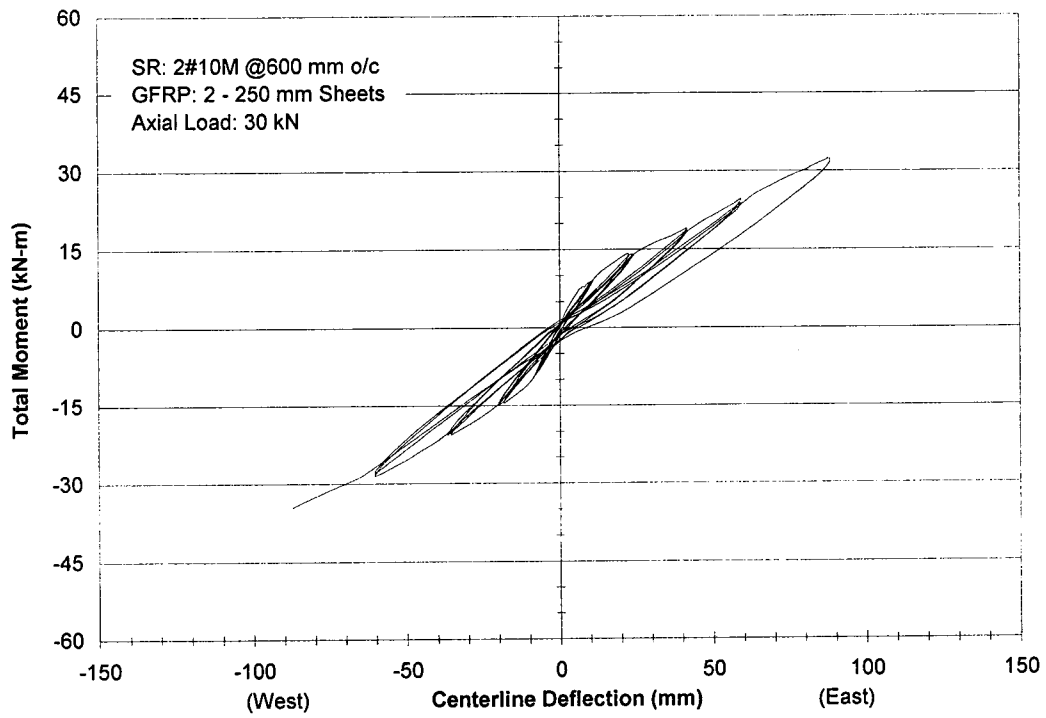

Figure 4.15 Moment versus Deflection Hysteresis for Wall 5b

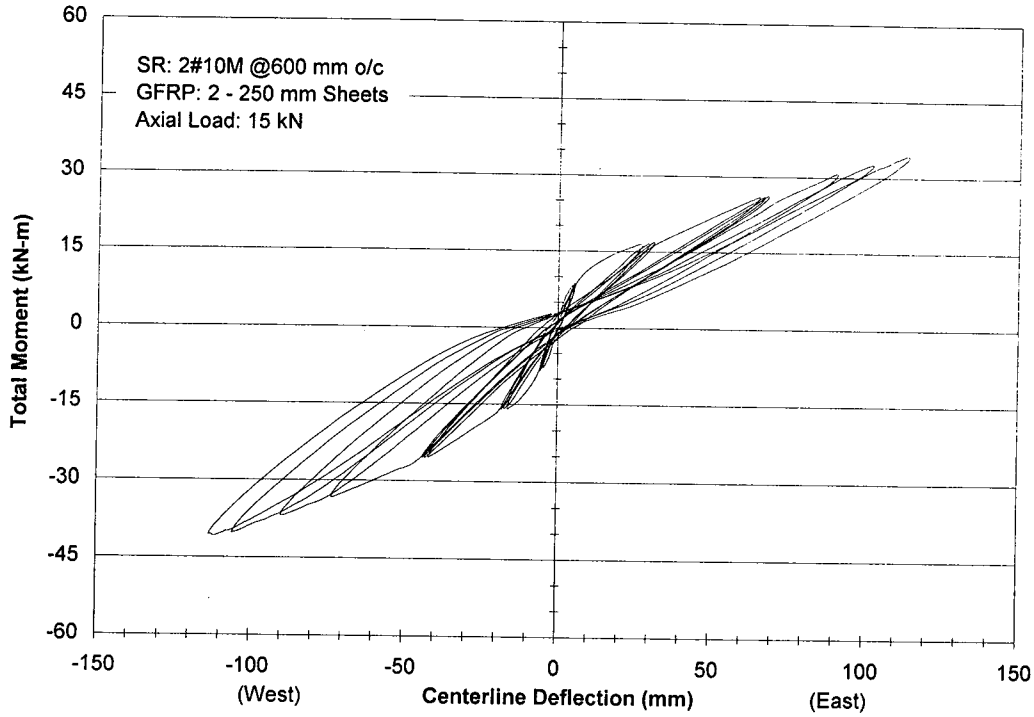

Figure 4.16 Moment versus Deflection Hysteresis for Wall 6

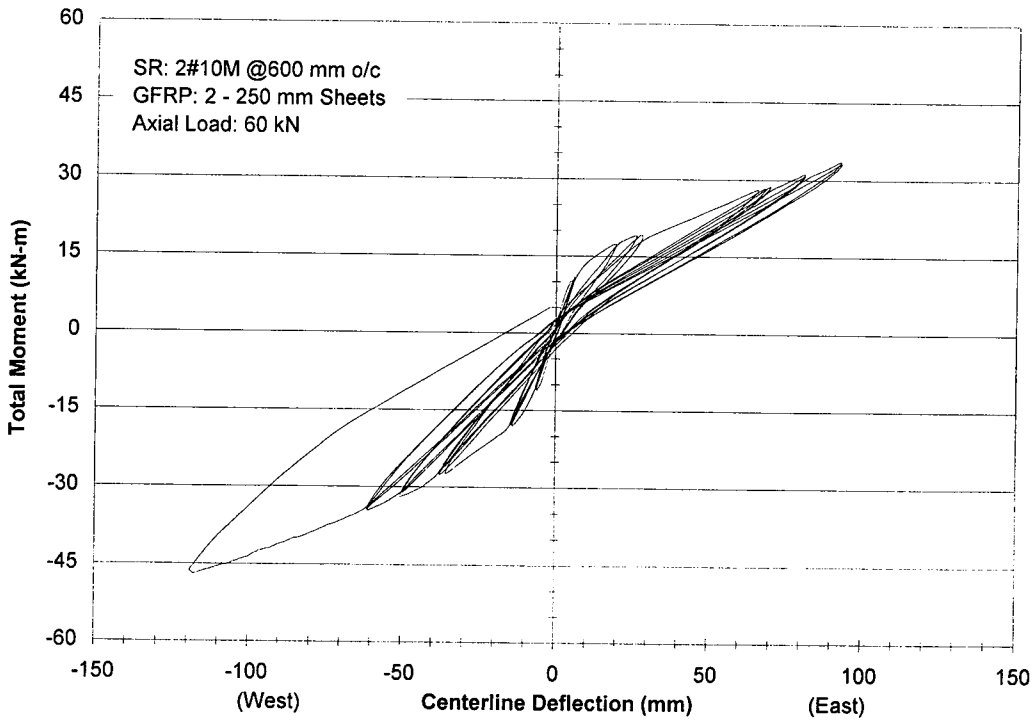

Figure 4.17 Moment versus Deflection Hysteresis for Wall 7

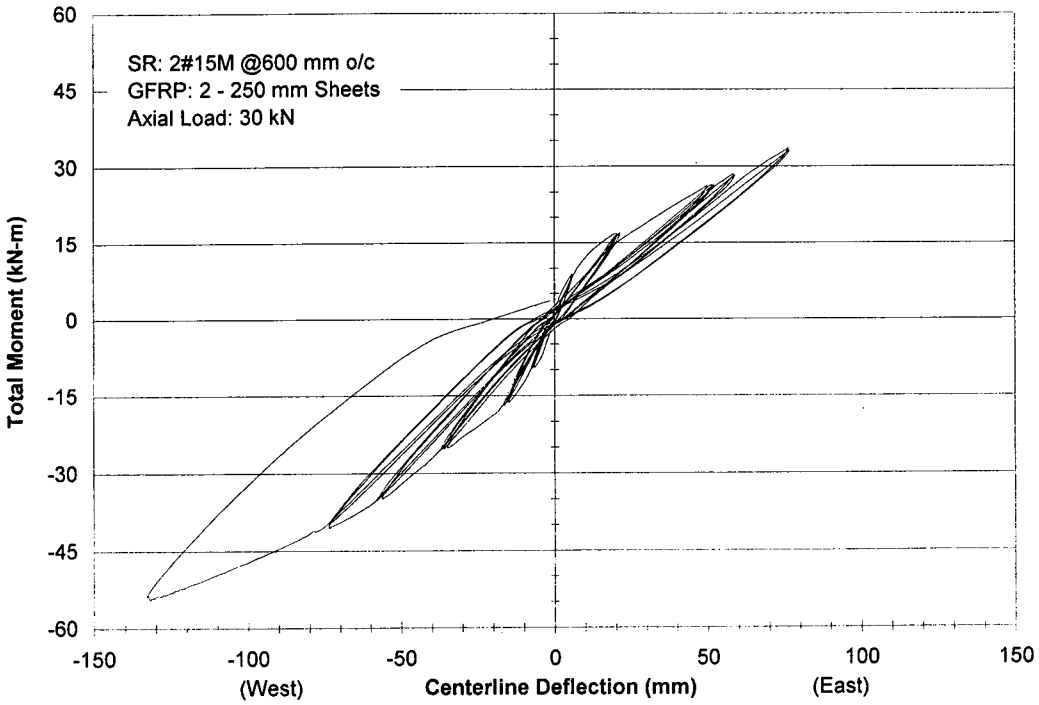

Figure 4.18 Moment versus Deflection Hysteresis for Wall 8

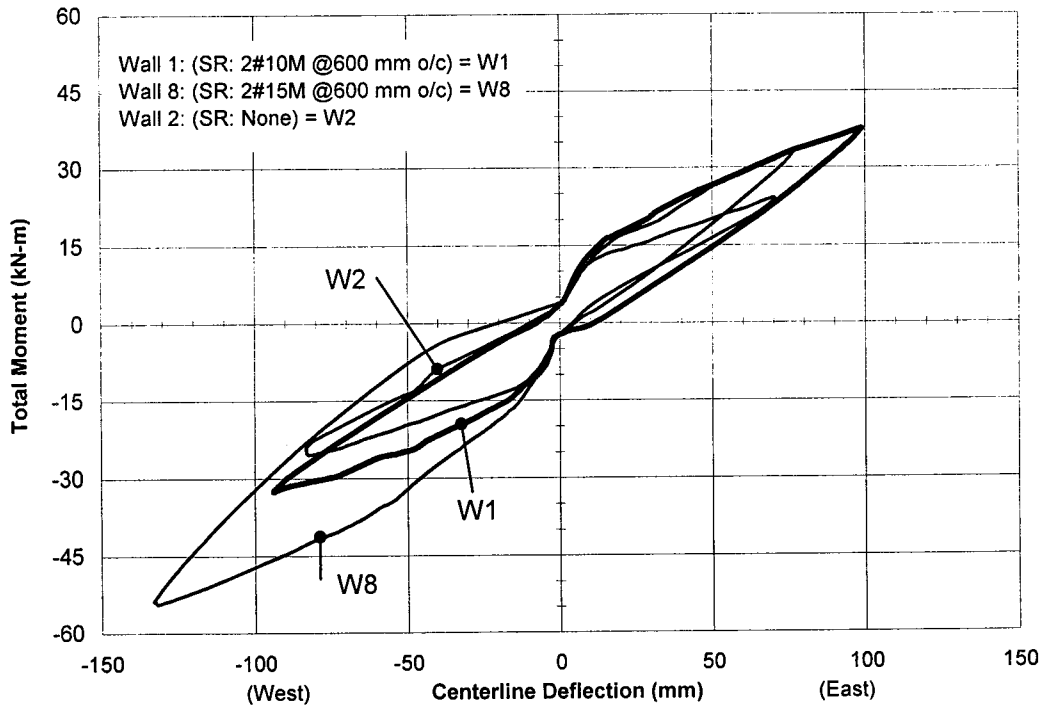

Figure 4.19 Moment versus Deflection Envelopes for Different Steel Reinforcement Ratios

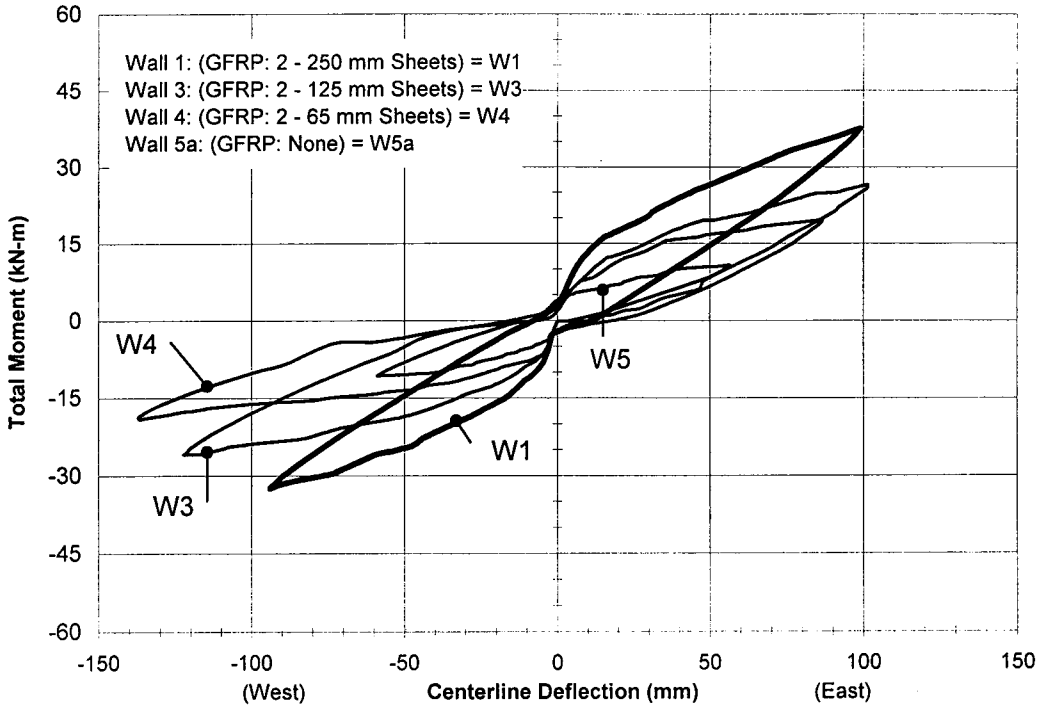

Figure 4.20 Moment versus Deflection Envelopes for Different GFRP Reinforcement Ratios

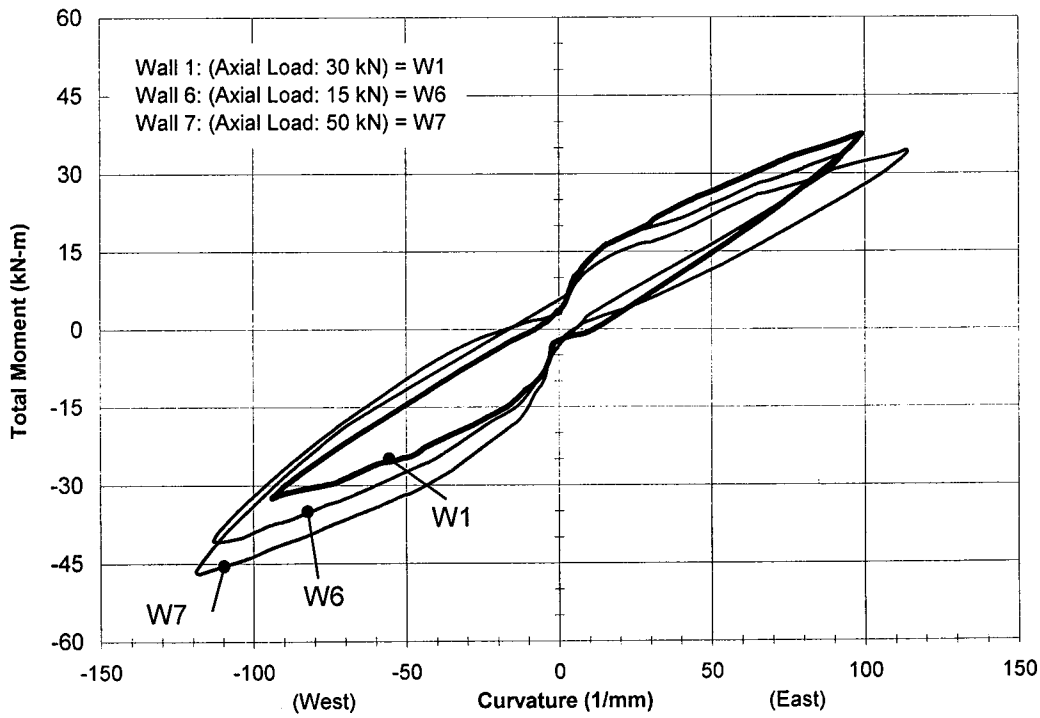

Figure 4.21 Moment versus Deflection Hysteresis for Different Levels of Aial Load

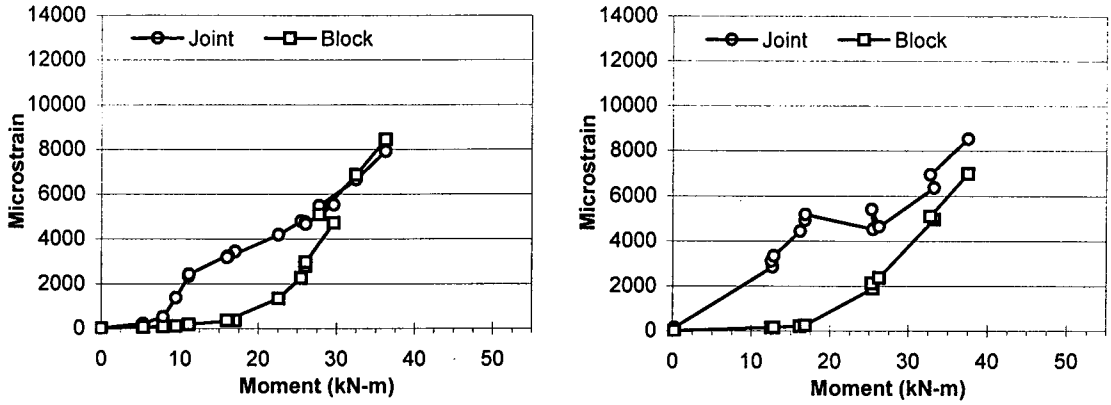

(West Side) (East Side)

(a) Wall 1
SR: 2#10M @600 mm o/c
GFRP: 2 - 250 mm Sheets
Axial Load: 30 kN

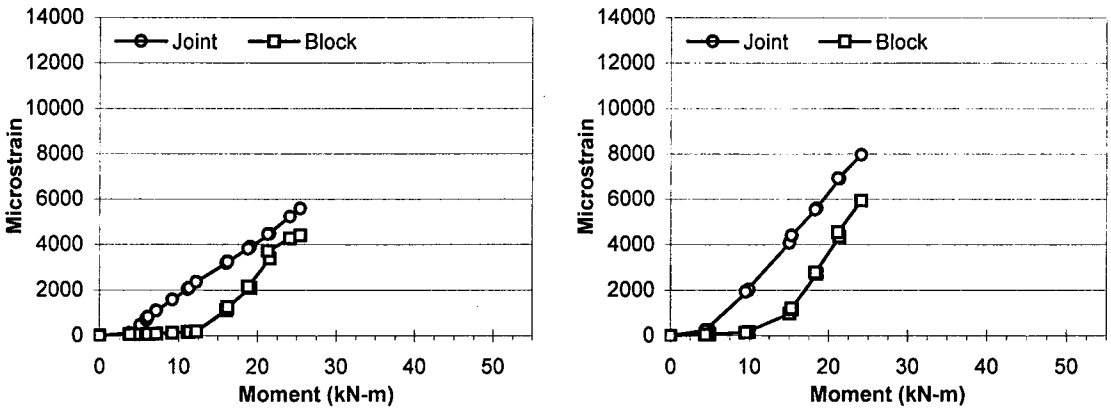

(West Side) (East Side)

(b) Wall 2
SR: None
GFRP: 2 - 250 mm Sheets
Axial Load: 30 kN

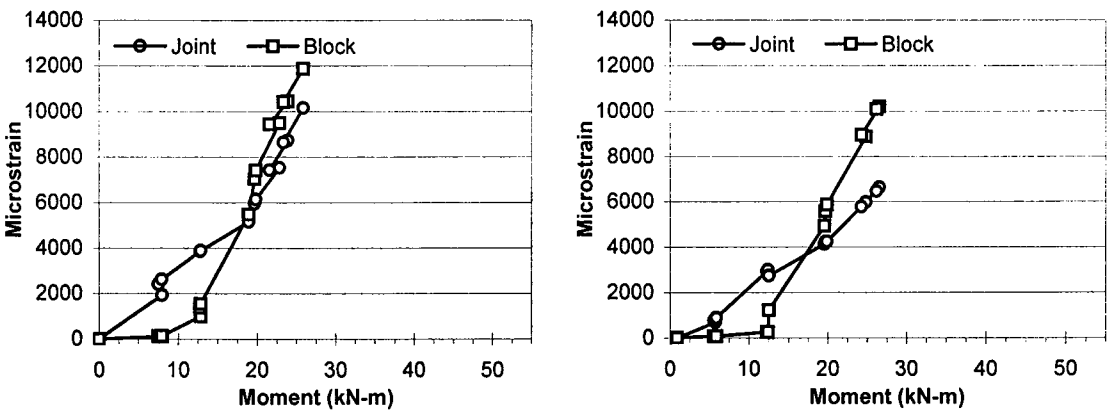

(West Side) (East Side)

(c) Wall 3
SR: 2#10M @600 mm o/c
GFRP: 2 - 125 mm Sheets
Axial Load: 30 kN

Figure 4.22 Average GFRP Joint and Block Strains versus Moment

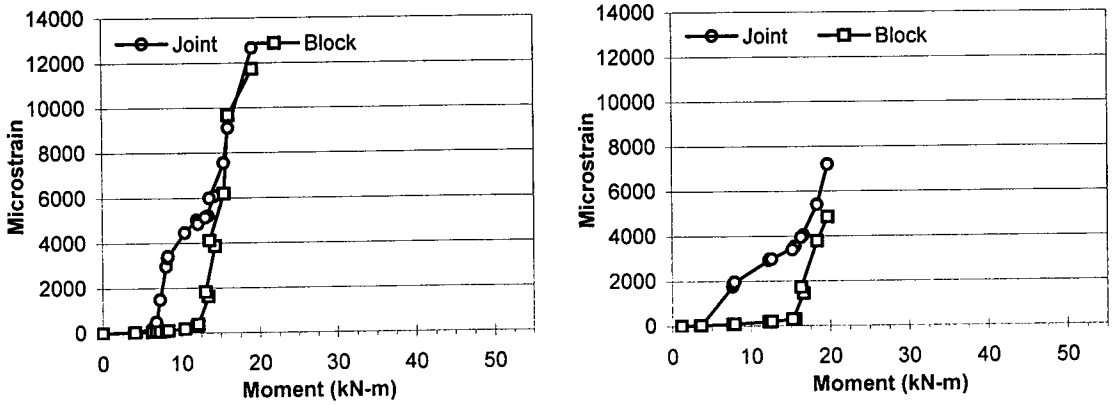

(West Side) (East Side)

(a) Wall 4
SR: 2#10M @600 mm o/c
GFRP: 2 - 65 mm Sheets
Axial Load: 30 kN

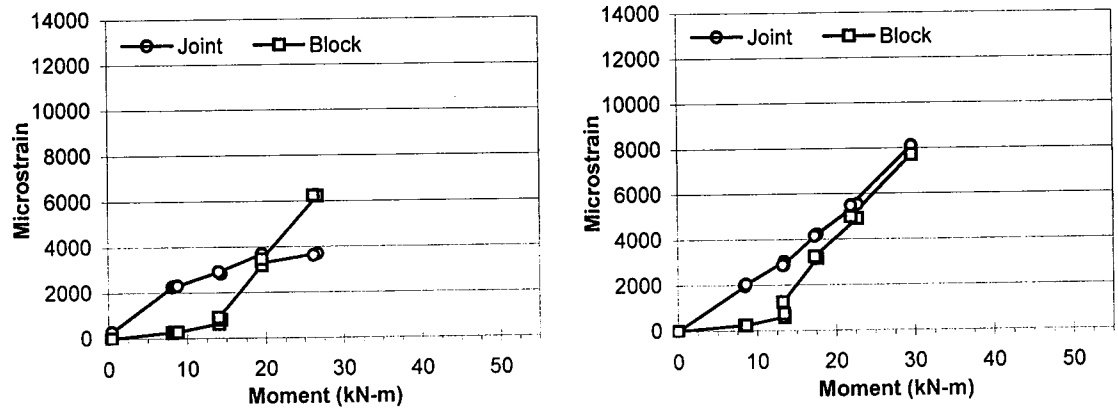

(West Side) (East Side)

(b) Wall 5b (cracked)
SR: 2#10M @600 mm o/c
GFRP: 2 - 250 mm Sheets
Axial Load: 30 kN

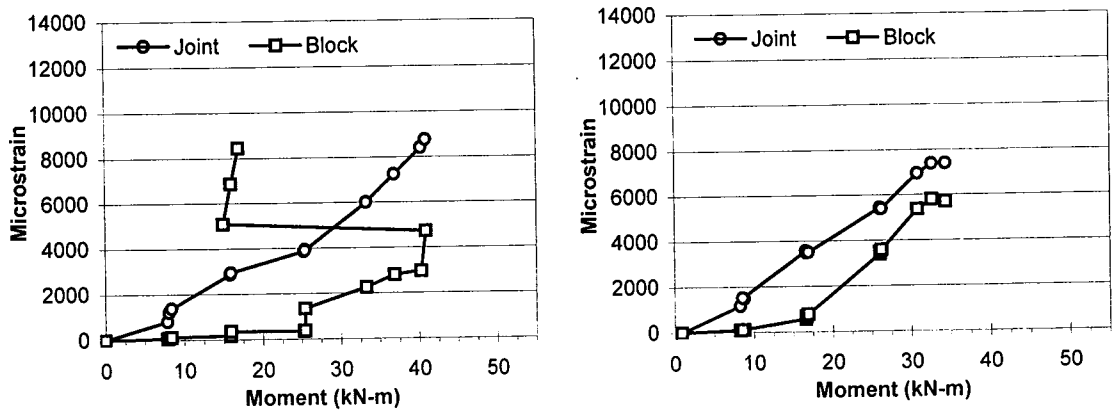

(West Side) (East Side)

(c) Wall 6
SR: 2#10M @600 mm o/c
GFRP: 2 - 250 mm Sheets
Axial Load: 15 kN

Figure 4.23 Average GFRP Joint and Block Strains versus Moment

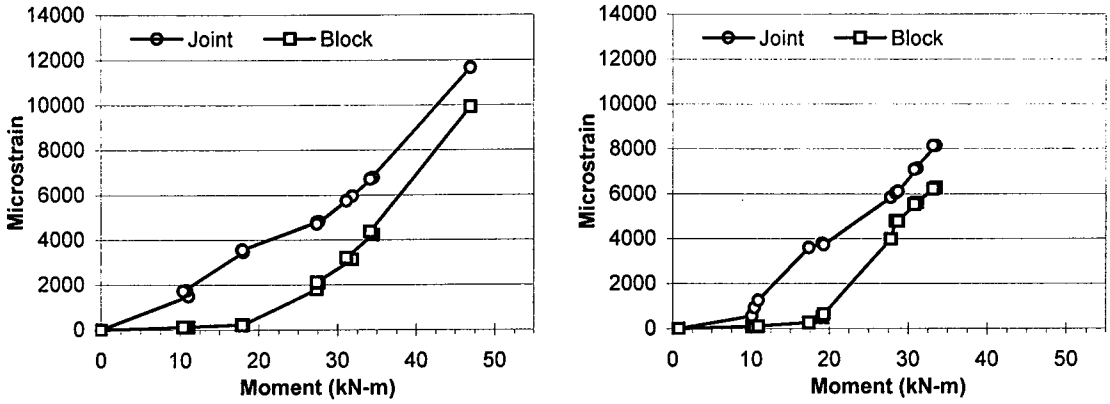

(West Side) (East Side)

(a) Wall 7

SR: 2#10M @600 mm o/c
GFRP: 2 - 250 mm Sheets
Axial Load: 60 kN

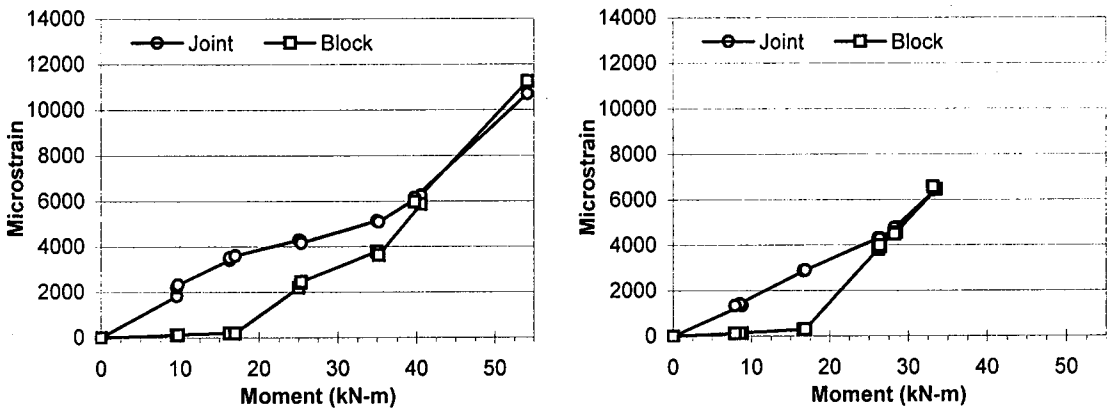

(West Side) (East Side)

(b) Wall 8

SR: 2#15M @600 mm o/c
GFRP: 2 - 250 mm Sheets
Axial Load: 30 kN

Figure 4.24 Average GFRP Joint and Block Strains vs Moment

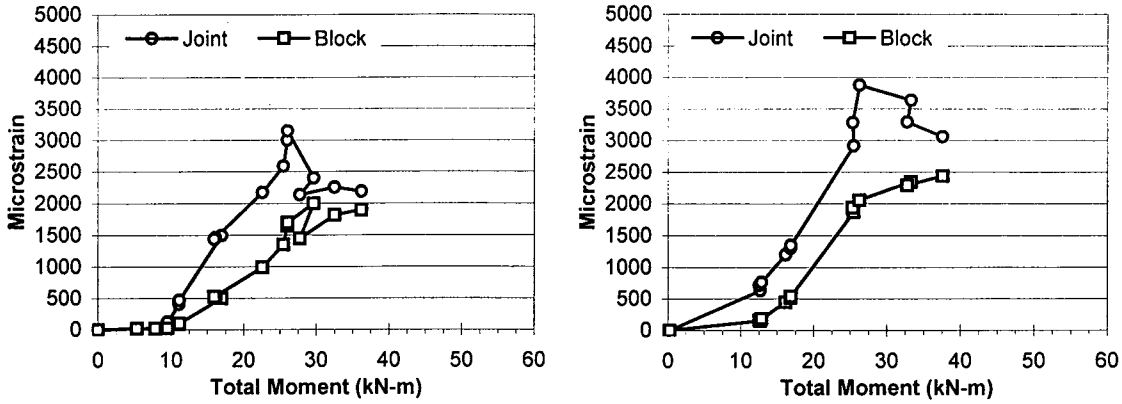

(West Side) **(a) Wall 1** (East Side)

SR: 2#10M @600 mm o/c
GFRP: 2 - 250 mm Sheets
Axial Load: 30 kN

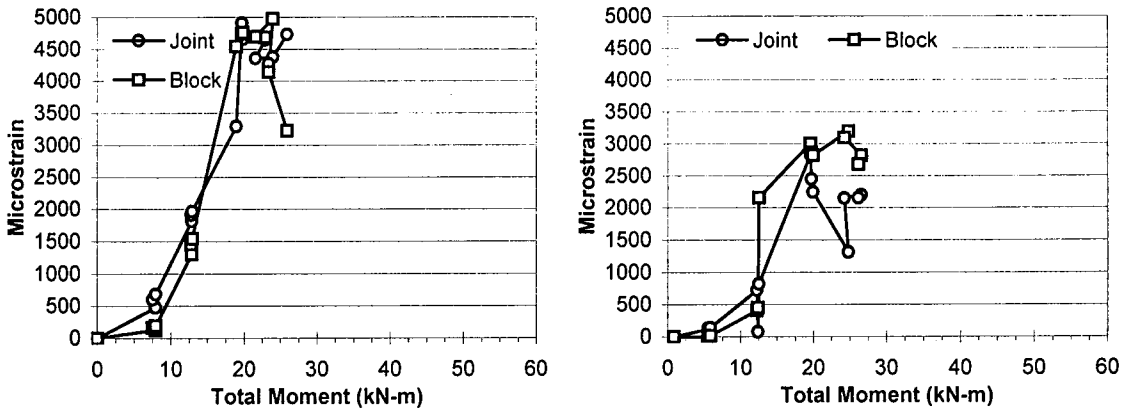

(West Side) **(b) Wall 3** (East Side)

SR: 2#10M @600 mm o/c
GFRP: 2 - 125 mm Sheets
Axial Load: 30 kN

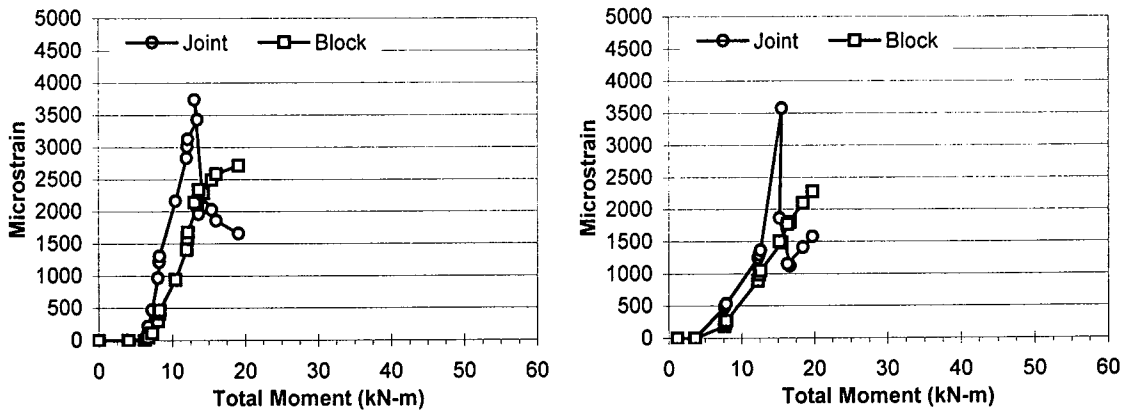

(West Side) **(c) Wall 4** (East Side)

SR: 2#10M @600 mm o/c
GFRP: 2 - 65 mm Sheets
Axial Load: 30 kN

Figure 4.25 Rebar Joint and Block Strains versus Total Moment

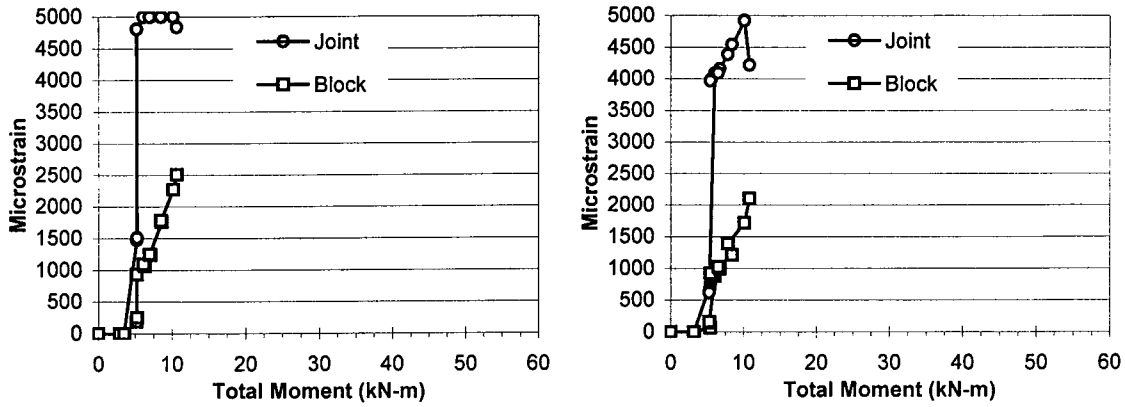

(West Side) **(a) Wall 5a** (East Side)

SR: 2#10M @600 mm o/c
GFRP: None
Axial Load: 30 kN

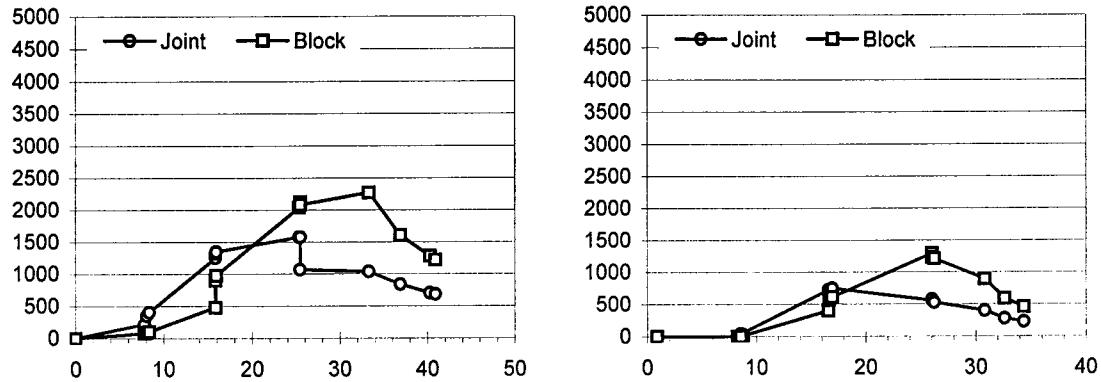

(West Side) **(b) Wall 6** (East Side)

SR: 2#10M @600 mm o/c
GFRP: 2 - 250 mm Sheets
Axial Load: 15 kN

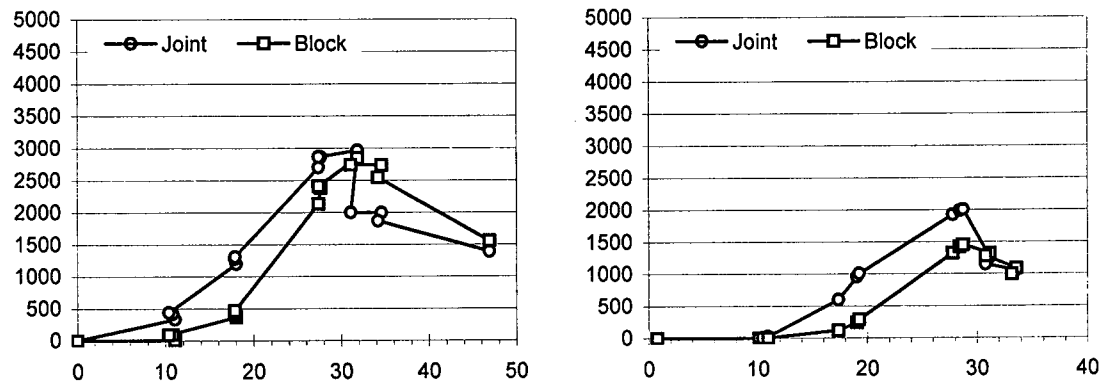

(West Side) **(c) Wall 7** (East Side)

SR: 2#10M @600 mm o/c
GFRP: 2 - 250 mm Sheets
Axial Load: 50 kN

Figure 4.26 Rebar Joint and Block Strains versus Total Moment

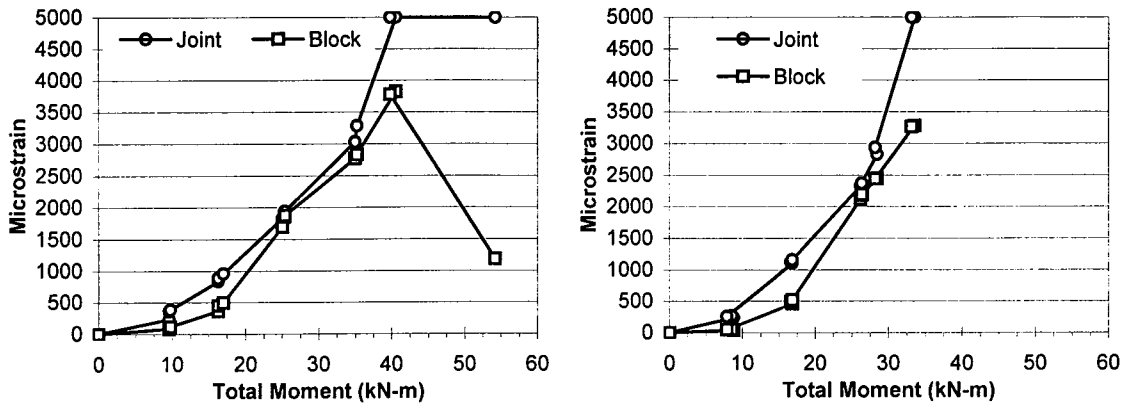

Figure 4.27 Rebar Joint and Block Strains versus Total Moment

5. QUANTITATIVE BEHAVIOR AND NUMERICAL MODEL

5.1 Introduction

There are many models available to predict the load versus deflection response for reinforced concrete elements but most are too complicated to implement (Saiidi, 1982). A very simple and, therefore, practical model developed by Saiidi and Sozen (1979) includes all of the characteristics of the hysteresis loops obtained. The model is referred to as the Q-HYST and is governed by only four rules. Key features of this model include: the loading response is bilinear with an ascending post-yield branch, the unloading stiffness beyond yielding is a function of the maximum experienced deformation, and stiffness degradation is accounted for during load reversal.

To successfully quantify and thus predict the out-of-plane behavior of any wall system, an understanding of the mechanics of each material and the interaction between materials is required. In assessing the qualitative behavior, the GFRP and steel reinforcement strains were used extensively. These data were again used along with a fundamental strength of materials approach to mathematically quantify the strength behavior. In addition, a flexural stiffness model was used to predict the stiffness degradation, thus deflections, throughout the loading history.

5.2 Flexural Strength

To define the flexural strength behavior, three bending moment values must be calculated. These are the cracking moment (M_{cr}), the transition moment (M_T), and the ultimate moment (M_u).

5.2.1 Cracking Moment

Theoretically, the cracking moment is determined from the tensile strength of masonry (f_t) and the section modulus (S) as shown in Equation 5-1.

$$M_{cr} = f_t S \qquad [5\text{-}1]$$

However, Equation 5-1 has no provisions to account for compressive axial loads which increase the cracking moment by shifting the neutral axis away from the compression face. To include axial load effects into M_{cr}, guidance from the Canadian Masonry Code CSA-S304.1-94 (1994) was used which presents the factored cracking moment in the form:

$$M_{cr} = \frac{\left(\phi_m f_t + \frac{P}{A_e}\right)}{y_t} I_o \qquad [5\text{-}2]$$

where,

ϕ_m = resistance factor for masonry, 0.55,

P = axial compressive force (N),

A_e = effective area of uncracked cross section, (mm^2),

y_t = distance from the neutral axis to the extreme tension fibre, (mm) and

I_o = moment of inertia of the effective area about its centroidal axis (mm^4).

Various research has shown that cracking at the bed joint location occurs through the depth of the tension face shell under very small moments. Thus, a good approximation of the moment of inertia up to the cracking moment is calculated using the net area with only one face shell. For reference, all moments of inertia discussed in this document are calculated about the geometric centroid of the cross section. Abboud *et al.* (1995) designated this modified moment of inertia as I_g^f. Modifying Equation 5-2 to remove the material resistance factor and include the various section properties yields the modified cracking moment (M_{cr}^f) as:

$$M_{cr}^f = \left(0.7 + \frac{P}{A_e}\right) \cdot \left(\frac{2\, I_g^f}{h}\right) \qquad [5\text{-}3]$$

where,

h = total depth of the cross section, (mm) and

I_g^f = modified moment of inertia, (mm^4) (Abboud *et al.*, 1995).

5.2.2 Transition Moment

As mentioned in the previous section, the transition moment depends solely on the amount of GFRP bonded to the wall. To assess M_T, the GFRP reinforcement ratios were plotted against the ratios of M_T/M_{cr} determined from the test data and a linear regression was performed. Figure 5.1 shows the regression line plotted through the data and the resulting linear equation relating the two ratios. The linear approximation is an excellent fit through the data as the coefficient of determination, R^2, is very close to 1.0. The relationship determined from the regression analysis can be mathematically incorporated into the cracking moment equation quite easily. However, a physical interpretation must be associated with this factor for it to be justified.

The two components making up the theoretical cracking moment relationship are the masonry tensile strength and the section modulus. Some boundary layer regions of masonry directly adjacent to the bonded GFRP may have a slight increase in tensile strength due to the absorption of epoxy. However, this boundary layer is highly variable and so small relative to the effective area that it can be neglected. The only remaining term is the section modulus which is what the regression equation targets. With the addition of the GFRP, the initial cracking point is not delayed. But, once a crack starts, the rate at which the crack propagates through the cross section is influenced greatly by the amount of GFRP on the tension face. The amount of GFRP can be expressed as a reinforcement ratio (ρ_T) in terms of the transformed section area as:

$$\rho_T = \frac{A_{GFRP} E_{GFRP}}{A_e E_m} \qquad [5\text{-}4]$$

where,

A_{GFRP} = area of GFRP on one side of the wall, (mm^2),

E_{GFRP} = modulus of elasticity of the GFRP, (MPa) and

E_m = modulus of elasticity of masonry, (MPa).

The modulus of elasticity, E_m, is usually assumed to be a linear function of the prism strength, f'_m:

$$E_m = k f'_m \qquad [5\text{-}5]$$

where,

f'_m = compressive strength of masonry, (MPa).

As an aside, the properties of masonry are known to vary from region to region. Therefore, there is no agreement on which value to use for the proportionality constant *k* in Equation 5-5 to determine the masonry modulus of elasticity. Values of *k* ranging from 750 to 1000 have been used. Up to 1985, the UBC specified a value for *k* of 1000 and then reduced it to 750. The CSA S304.1-94 (1994) specifies a value for *k* of 850. In choosing an appropriate value for *k*, it must be realized that the lower value is not necessarily conservative. When assessing deflections of individual members, using a lower value for E_m over-predicts the deflections, which is conservative under static loading cases. However, under seismic loading, over-predicting deflections or under-predicting member stiffness is unconservative as the member may be subjected to forces greater than those predicted in the structural analysis. Thus, the value of 850 was adopted in this document if for no better reason that it is, roughly, the mean of the three values. Equation 5-6 expresses the relationship used to determine E_m in this document.

$$E_m = 850 f'_m \qquad [5\text{-}6]$$

Now, if the regression term from Figure 5.1 is multiplied by Equation 5-3, an expression for M_T is obtained as:

$$M_T = \left(0.7 + \frac{P}{A_e}\right) \cdot \left(\left(\frac{2\,I_g^f}{h}\right)(1 + 94.3\rho_T)\right) . \qquad [5\text{-}7]$$

Simplifying this expression, the transition moment can be expressed in the form of:

$$M_T = M_{cr}^f \cdot (1 + 94.3\rho_T) . \qquad [5\text{-}8]$$

5.2.3 Ultimate Moment

The flexural design philosophy adopted for both reinforced concrete and masonry is to ensure a ductile failure. This is achieved by limiting both the compression strains and the steel reinforcement ratio to ensure the steel yields before the material in compression crushes. The approach developed here follows the same philosophy of ensuring a flexural failure mode, only this criteria has been implemented by limiting the ultimate GFRP strains.

As stated in Chapter 3, all the observed failures were of the flexure-shear mode. Each specimen failed at a different level of moment which was observed to be strongly related to the amount of GFRP bonded to the specimens. A short discussion of the effect of each testing parameter is included within Section 4.3. A linear regression analysis was performed between the measured strains in the GFRP at the point of wall failure and the corresponding area of GFRP used. Figure 5.2 includes the linear relationship from the regression analysis in addition to the coefficient of determination. As indicated by the R^2 value of 0.9969, the linear fit to the data is excellent. From this analysis, a relationship between the GFRP area and the maximum strain at the ultimate moment is proposed in Equation 5-9:

$$\varepsilon_{u\,GFRP} = (13200 - 6.5A_{GFRP}) \times 10^{-6} \qquad [5\text{-}9]$$

where,

$\varepsilon_{u\,GFRP}$ = maximum GFRP strain, (mm/mm).

The procedure used to calculate the ultimate moment is the same used in the flexural design of reinforced concrete members. For concrete members, the moment resistance (M_r) without material safety factors is given as:

$$M_r = A_s f_y \left(d - \frac{a}{2} \right) \qquad [5\text{-}10]$$

where,

A_s = area of steel reinforcement, (mm^2),

f_y = yield strength of steel reinforcement, (MPa),

d = distance from the extreme compression fibre to the centroid of the tension steel, (mm) and

a = depth of the equivalent rectangular stress block, (mm).

For systems with external GFRP, Equation 5-10 is modified to a more general form to include the contribution of the GFRP as expressed as:

$$M_u = A_s f_y \left(d - \frac{a}{2} \right) + A_{GFRP} E_{GFRP} \varepsilon_{u\,GFRP} \left[\left(h + \frac{t_{GFRP}}{2} \right) - \frac{a}{2} \right] \qquad [5\text{-}11]$$

where,

t_{GFRP} = nominal thickness of GFRP, (mm).

The term representing the depth of the equivalent rectangular stress block for a cross section is typically calculated using Equation 5-12:

$$a = \frac{P + \phi_s A_s f_y}{0.85 f'_m \beta_1 b} \qquad [5\text{-}12]$$

where,

ϕ_s = material safety factor for reinforcing steel,

0.85 = approximation of rectangular stress block height,

β_1 = factor based on f'm used to compute depth of stress block and

b = width of the compression zone, (mm).

This relationship was developed for use in reinforced concrete and has simply been adopted in its entirety by the masonry field. The mechanics of Equation 5-12 are valid in masonry, however the 0.85 term and the β_1 factor in the denominator warrant further discussion. Both of these factors were empirically determined by performing non-linear regression analysis on data obtained from different sources for the compressive strength of concrete cylinders. Kaar *et al.* (1978) extended the database established by Hognestad *et al.* (1955) for determining these parameters to include high strength concrete. The original publication by Hognestad *et al.* (1955) defined the parameters to approximate the rectangular stress block shape and its centroid location using the factors k_1, k_2, and k_3 as shown in Figure 5.3. The terms of interest in the denominator of Equation 5-12, namely β_1 and the 0.85 term, relate to the factors k_1 and k_3 respectively. Both k_1 and k_3 are shown to vary nonlinearly with the concrete compressive strength. Thus, both terms can not, and should not, be mathematically combined in a linear sense or evaluated individually with the concrete strength and then combined as done in Equation 5-12. The denominator in Equation 5-12 is really an approximation to a region within the regression analysis. This approximation works very well for concrete strengths ranging from about 20 to 50 MPa. However, the approximation is excessively conservative for concrete strengths lower than 15 MPa. Thus, this expression very poorly approximates the dimensions of an equivalent rectangular stress block from the actual parabolic stress distribution. Kaar *et al.* (1978) presented the polynomial regression equation for normal weight concrete between the product of k_1k_3 and the compressive concrete strength as shown in Equation 5-13:

$$k_1k_3 = 0.00003\, f_c'^4 - 0.0013\, f_c'^3 + 0.0214\, f_c'^2 - 0.1672\, f_c' + 1.1564 \qquad [5\text{-}13]$$

where,

k_1k_3 = β_1*0.85, (ksi) and

f'_c = concrete compressive strength, (ksi).

As an example, the masonry prism compressive strength determined in this testing program was 10 MPa (1.450 ksi). This strength value was interpolated linearly between the fully grouted and ungrouted prism strengths to account for the level of grouting in the wall specimens. β_1 given in CSA S304.1 for compressive strengths up to 20 MPa is 0.8. Thus, the product of 0.85 and 0.8 is 0.68. In comparison, the product determined from Equation 5-13 is 0.96. This is a 29% error in determining the product of k_1k_3 for this highly typical masonry assembly strength of 10 MPa. If the GFRP tensile force contribution is added to the numerator and the denominator is corrected for a strength of 10 MPa, the expression for computing the stress block "a" becomes:

$$a = \frac{P + A_s f_y + A_{GFRP} E_{GFRP} \varepsilon_{u\,GFRP}}{0.96\, f'_m b} . \qquad [5\text{-}14]$$

5.3 Lateral Deflection

Accurately predicting the out-of-plane deflections in masonry is difficult due largely to the continually changing flexural stiffness, EI. To the author's best knowledge, the best attempt at predicting the out-of-plane deflections of masonry walls was proposed by Abboud *et al.* (1995). The deflection analysis developed for the GFRP reinforced walls tested by the author is based upon the flexural stiffness degradation model proposed by Abboud *et al.* (1995).

The stiffness model proposed by Abboud *et al.* (1995) for reinforced masonry walls is presented below. The model predicts an effective stiffness for a given level of moment above the cracking moment. This effective stiffness can then be used in an appropriate beam deflection equation to determine the desired lateral displacements.

$$(EI)_{eff} = (EI)^f_g R + (EI)_{cr}(1 - R) \qquad [5\text{-}15]$$

where,

$(EI)_g^f = (E_m)_g I_g^f$; modified gross sectional stiffness,

$(EI)_{cr} = \alpha\ (E_m)_g I_{cr}$; cracked sectional stiffness,

α = modulus of elasticity reduction factor

= 0.5 for fully grouted section; 0.32 for partially grouted section,

R $= (0.4)X + (0.6)X^4$; stiffness interpolation factor,

X $= (M_n - M_a) / (M_n - M_{cr})$; moment ratio,

M_n = nominal moment strength,

M_a = bending moment acting at the condition under which deflection is Computed,

I_g^f = modified gross section moment of inertia with one face shell only and

I_{cr} = cracked section moment of inertia.

5.3.1 GFRP Wall Deflections

To incorporate the model proposed by Abboud *et al.* (1995), several slight modifications were made. First, it should be noted that the model is only applied at levels of moment beyond the transition moment. From point *A* to point *C* on Figure 4.1, a linear path is used with the slope determined using $(EI)_g^f$ for the stiffness. From point *C* to point *F*, the model is applied to predict the loading stiffness of the envelope.

In the development of the proposed model by Abboud *et al.* (1995), the general form of the term α is given in Equation 5-16.

$$\alpha = \frac{M_u I_g^f \Delta_{cr}}{M_{cr} I_{cr} \Delta_u} \qquad [5\text{-}16]$$

To assess the coefficient α, the ultimate deflection (Δ_u) is required. This is easy to obtain from test specimens to confirm the model; however, a rational method is required to compute Δ_u for any wall to make the model a useful design tool.

For systems which behave plastically, quantifying an ultimate deflection requires an iterative procedure or one of trial and error. Once the system yields, knowing how much

plastic strain the system will tolerate is difficult to assess. This renders calculating the ultimate deflections from a curvature approach highly variable.

Alternatively, this is not the situation for walls with externally bonded GFRP. The GFRP behaves in a linear elastic manner until it ruptures, which is well beyond the failure point of the tested walls. An ultimate deflection assessment based on curvature can therefore be accurately performed. The author is proposing a method that uses the ultimate GFRP strains predicted from Equation 5-9 to assess the ultimate curvature. At large deflections, masonry behaves like a number of rigid bodies connected by a tension tie. Thus, a rigid body rotation occurs between most masonry blocks to accommodate the strain compatibility required for that particular curvature. As previously stated, for masonry walls reinforced only with steel, this tension tie becomes plastic at some curvature and thus the ultimate strain and/or curvature is not easily assessed. For walls reinforced with GFRP, the ultimate GFRP strain for the ultimate curvature is known. This permits the deflection to be obtained from a closed form solution.

Initially, the wall is assumed to behave as a continuum with no rigid body rotations. The strain profile in the GFRP is assumed to have the same shape as the bending moment diagram. Knowing the predicted ultimate strain in the GFRP and the predicted location of the neutral axis, the curvature can be assessed by simple geometry. Once the corresponding curvature is determined, this value can be substituted into the appropriate beam equation to obtain the deflection at any point along the wall.

To obtain the relationship for the ultimate curvature, the components of the triangle in Figure 5.4 must be determined. The long leg is simply defined as (h-a) which is the wall depth minus the neutral axis depth. The second leg, labeled ε_{GFRP}, is the strain in the GFRP at the ultimate load determined from Equation 5-9. Since the angle formed by the triangle is very small, i.e. 10^{-5} radians, the small angle approximation can be applied which renders $\sin(\theta) \cong \theta$. This assumes that all the rigid body rotations occurring at the bed joint level are locally distributed along the wall. The expression for the ultimate curvature can now be expressed as:

$$\frac{M}{EI} = \frac{1}{\rho} = \frac{\Delta_{GFRP}}{h-a} = \frac{\varepsilon_{u\,GFRP}}{h-a} \qquad [5\text{-}17]$$

For the walls tested, the applicable beam deflection equation is given in Equation 5-18.

$$\Delta_{MAX} = \frac{P \cdot x \cdot \left(3L^2 - 4x^2\right)}{24\,EI} = \frac{M}{EI}\frac{\left(3L^2 - 4x^2\right)}{24} \qquad [5\text{-}18]$$

The true behavior of masonry walls deviates slightly from that of a continuum and acts like a series of rigid bodies connected by a linear elastic tension tie. Equation 5-18 is for a member which acts a perfect continuum which is a good approximation for the walls tested since the cracks are small in relation to the height of the wall. Nevertheless, the continuum approach slightly underestimates the maximum deflection by about 5% as compared to a discrete analysis performed for a wall having a height of 20 courses.

Although some horizontal cracking was observed in individual masonry units during testing, these crack widths were much smaller than those observed at the bed joint locations. Thus, all the horizontal cracks from the center-to-center of each course can be assumed to be concentrated in one large crack at the bed joint location. A correction factor is proposed for Equation 5-18 to account for the crack spacing; thus, the simple continuum approach can accurately be used for the discrete case. The relationship in Equation 5-19 is proposed for calculating the ultimate deflections for the wall specimens tested in this program; however, this general procedure is applicable to any loading and wall geometry configurations as:

$$\Delta_u = \left[\frac{\varepsilon_{u\,GFRP}}{h-a}\right] \cdot \frac{\left(3L^2 - 4x^2\right)}{24\left(1 - \frac{2 \cdot S_{cr}}{L}\right)} = \left[\frac{\varepsilon_{u\,GFRP}}{190-a}\right] \cdot \frac{\left(3L^2 - 4x^2\right)}{24\left(1 - \frac{2\,(200)}{L}\right)} \qquad [5\text{-}19]$$

where,

L = wall height, (mm),

x = shear span length, (mm) and

S_{cr} = crack spacing; assumed at 200 mm, (mm).

5.3.2 Moment-Deflection Model

The model proposed to predict the bending moment versus deflection hysteresis envelope is based on that proposed by Abboud *et al.* (1995). To account for the behavioral differences observed in the GFRP systems, some changes have been incorporated into Abboud's model. The model is based on a rational mechanics approach and thus only requires knowledge of the cross-sectional geometry and the material physical properties. All the terms required are determined from closed-form solutions and no additional tables and/or figures are required for any of the calculations. Thus, the procedure for predicting the entire moment versus deflection envelope is ideally suited for implementation into any spreadsheet program. For the convenience of the reader, all the equations referenced in this subsection will be explicitly rewritten within the subsection with the origin equation number maintained in *italics*. All the variables will be defined at the end of the subsection.

The points in Figure 4.1 will be referenced throughout the following procedure. In predicting the initial loading region, the cracking moment is not plotted as the transition moment is simply a linear multiple of the cracking moment. The starting point is the origin which is defined by zero moment and zero deflection. Both the transition moment and the transition deflection are required to plot the initial region. The transition moment is obtained from Equation 5-7 and the corresponding deflection is calculated from Equation 5-20.

$$\rho_T = \frac{A_{GFRP} E_{GFRP}}{A_e E_m} \qquad [5\text{-}4]$$

$$M_{cr}^f = \left(0.7 + \frac{P}{A_e}\right) \cdot \left(\frac{2\, I_g^f}{h}\right) \qquad [5\text{-}3]$$

$$M_T = M_{cr}^f \cdot (1 + 94.3\rho_T) \qquad [5\text{-}8]$$

$$\Delta_T = \frac{M_T}{E_m I_g^f}\frac{\left(3L^2 - 4x^2\right)}{24} \qquad [5\text{-}20]$$

A straight line is then plotted from the origin to point *C* using Equation 5-20. Next, a continuous curve is plotted from point *C* to point *F* using the modified stiffness degradation model. The following parameters are required for this region.

$$\Delta_{cr}^f = \frac{M_{cr}^f}{E_m I_g^f}\frac{\left(3L^2 - 4x^2\right)}{24} \qquad [5\text{-}21]$$

$$\varepsilon_{u\,GFRP} = \left(13200 - 6.5A_{GFRP}\right)\times 10^{-6} \qquad [5\text{-}9]$$

$$a = \frac{P + A_s f_y + A_{GFRP}E_{GFRP}\varepsilon_{u\,GFRP}}{0.96\, f_m' b} \qquad [5\text{-}14]$$

$$M_u = A_s f_y\left(d - \frac{a}{2}\right) + A_{GFRP}E_{GFRP}\varepsilon_{u\,GFRP}\left[\left(h + \frac{t_{GFRP}}{2}\right) - \frac{a}{2}\right] \qquad [5\text{-}11]$$

$$\Delta_u = \left[\frac{\varepsilon_{u\,GFRP}}{h - a}\right]\cdot\frac{\left(3L^2 - 4x^2\right)}{24\left(1 - \frac{2\cdot S_{cr}}{L}\right)} \qquad [5\text{-}19]$$

$$\alpha = \frac{M_u I_g^f \Delta_{cr}}{M_{cr} I_{cr} \Delta_u} \qquad [5\text{-}16]$$

$$R_a = (0.4)\left(\frac{M_u - M_a}{M_u - M_T}\right) + (0.6)\left(\frac{M_u - M_a}{M_u - M_T}\right)^4 \qquad [5\text{-}22]$$

$$(EI)_{eff\,(a)} = E_m I_g^f R_a + \alpha E_m I_{cr}\left(1 - R_a\right) \qquad [5\text{-}23]$$

Equation 5-24 is then used to compute the deflection at any level of bending moment between the transition moment and the ultimate moment.

$$\Delta_a = \frac{M_a\left(3L^2 - 4x^2\right)}{24\,(EI)_{eff\,(a)}};\ \text{for } M_T \le M_a \le M_u \qquad [5\text{-}24]$$

As previously discussed, the unloading path can be considered as linear from any value of M_a to the origin. To plot the unloading path, a linear line is plotted from the desired level of M_a to the origin. For design purposes, the unloading branch connecting points *F* to *G* is typically not required.

5.4 Predicted Hysteresis Envelope

The procedure outlined in Section 5.3.2 was used to predict the loading region of the moment versus deflection envelopes for each of the tested wall specimens. Figures 5.5 through 5.13 show the predicted and actual bending moment versus centerline deflection envelopes for each wall. Tables 5.1 and 5.2 list the properties used in the wall deflection calculations and Table 5.3 lists the test-to-predicted ratios for both the strength model and the deflection model.

As shown in Table 5.3, the test-to-predicted ratios for the walls with externally bonded GFRP ranges from 1.01 to 1.14 for the ultimate bending moment calculations. This agreement between the test specimens and the mathematical model validates the rational mechanics approach used. Because the test-to-predicted results for the GFRP walls are greater than one, the rational approach is slightly conservative with no material safety factors applied.

The test-to-predicted ratios for the GFRP wall deflections ranges from 0.93 to 1.33. Predicting the ultimate deflections of masonry walls within 20 percent is very uncommon from the current literature surveyed. This, as previously stated, is due largely to the plastic material behavior and rigid body rotations. The proposed approach by the author for determining the ultimate deflections achieves the ±20 percent for five of the eight walls tested with GFRP. Walls 6 and 7 have a test-to-predicted ratio of 1.21 and 1.22 respectively. Thus, seven of the eight walls tested with external GFRP are within ±22 percent of the actual deflections. The curvature analysis approach, which assumes the mechanics from a continuum body, is thus justified with confidence for walls with externally bonded GFRP.

In predicting the bending moment versus deflection hysteresis, small differences in the ultimate bending moment have a greater influence on the shape of the envelope than

do small differences in the ultimate deflection. At the ultimate limit state, the bending moment versus deflection envelope has a relatively flat slope as compared to the initial region of loading. Thus, the shape of the envelope is more sensitive to small changes in the vertical direction than in the horizontal direction. Hence, the allowable deviations for each parameter are different. Where a maximum allowable error of 10 percent in predicting the moment may be desired, an error of 20 percent in predicting the deflections may be tolerable. Because the unloading path is linear from the maximum experienced moment/deflection coordinate to the origin, the slope is not adversely effected if both errors approach there maximum allowable.

The poorest test-to-predicted results were obtained for Wall 5a, the standard masonry wall reinforced only with steel reinforcement. This wall was tested to its ultimate load but not its ultimate deflection as it was desired to retrofit a partially damaged wall with GFRP. Thus, the test-to-predicted ratio for the strength parameter is valid but the ultimate deflection comparison is not. With a test-to-predicted ratio of 1.38 for the ultimate moment capacity, the mechanics approach adopted from reinforced concrete design was found to be highly conservative for masonry design in this case. The predicted deflection for Wall 5a presented in Table 5.3 was calculated by the same procedure used for the walls with GFRP. Instead of using the GFRP strains and geometry, the steel strain was taken as 0.002 mm/mm and the appropriate distance to the neutral axis was used to compute the ultimate curvature. This is not an accurate technique as the ultimate strain could exceed 0.005 mm/mm which would produce a large error in the predicted curvature.

5.4.1 Prediction of the Previously Damaged Wall

GFRP was placed on Wall 5b after it had been fully cracked during testing as Wall 5a. In predicting the moment versus deflection behavior, the transition moment concept discussed previously does not directly apply. With the addition of externally bonded GFRP to an uncracked wall, the rate of crack propagation through the depth of the wall was reduced. Hence, a greater effective moment of inertia was maintained beyond the cracking moment which gave rise to the introduction of the transition moment. Because

of the pre-cracked nature of the cross-section in Wall 5b, the masonry had zero tensile strength. Thus, the transition moment was reduced since the moment of inertia by default was that of a fully cracked section.

In predicting the behavior of Wall 5b using the proposed model, the transition moment was set equal to the cracking moment. Initially, the model was run using the transition moment but this overestimated the stiffness of the entire curve. Upon reducing this value within the model, the predicted moment versus deflection behavior followed the testing results more closely.

5.5 Governing Failure Criteria

As discussed in Section 3.6, the governing failure mode was that of flexure-shear. Because this failure mode dominated, the design procedure developed in Section 5.3.2 intrinsically predicts this failure mode. The basis for development of the ultimate allowable GFRP strain was the strain measured at failure for the different amounts of GFRP. Since each specimen failed by the same mode, the ultimate strains were governed by the failure mode.

However, in assessing the ultimate capacity of a wall for design purposes, the shear capacity should be checked in addition to the procedure presented in Section 5.3.2 for flexure. Albert *et al.* (1998) recommended using an equation for the shear resistance (V_r) based on the CSA-S304.1-94 code.

$$V_r = 0.16\sqrt{f'_m} \cdot b \cdot a + 0.25P \qquad [5\text{-}25]$$

This equation is only valid for walls where the value of $\frac{M_f}{V_f \cdot d} \geq 1$. Albert *et al.* (1998) recommended that the term 0.25P not be included as the ability of the axial load to counteract other forces at large deflections is reduced. The author does not agree with the removal of this term as the axial load effects have been taken into account in the calculation of the stress block dimension "a". It is therefore recommended that Equation 5-25 be used to determine the shear capacity of the wall systems.

Table 5.1 Calculated Flexural Stiffness Values from a Transformed Section Analysis

	Wall 1	Wall 2	Wall 3	Wall 4	Wall 5a	Wall 5b	Wall 6	Wall 7	Wall 8
Gross									
I_g (mm^4)	5.51E+08	4.90E+08	5.51E+08	5.51E+08	5.51E+08	5.51E+08	5.51E+08	5.51E+08	5.51E+08
$E_m I_g$ (Nmm^2)	4.69E+12	4.17E+12	4.69E+12	4.69E+12	4.69E+12	4.69E+12	4.69E+12	4.69E+12	4.69E+12
Cracked									
I_{cr} (mm^4)	2.11E+08	1.46E+08	1.78E+08	1.42E+08	9.99E+07	2.09E+08	2.16E+08	2.43E+08	2.58E+08
$E_m I_{cr}$ (Nmm^2)	1.79E+12	1.24E+12	1.51E+12	1.21E+12	8.49E+11	1.78E+12	1.84E+12	2.07E+12	2.19E+12
Compression Block Dimension									
a =	22.9	13.7	19.4	15	10.4	22.7	23.7	28.6	33
Modified Gross									
I_g^f (mm^4)	3.15E+08	2.54E+08	3.15E+08	3.15E+08	3.15E+08	N/A	3.15E+08	3.15E+08	3.15E+08
$E_m I_g^f$ (Nmm^2)	2.68E+12	2.16E+12	2.68E+12	2.68E+12	2.68E+12	N/A	2.68E+12	2.68E+12	2.68E+12

where $E_m = 850\, f'_m = 8500$ MPa

Table 5.2 Properties used to Calculate the Neutral Axis "a"

Wall	Axial Load (kN)	GFRP Area (mm^2)	Steel Area (mm^2)	ε_{GFRP} (mm/mm)	a (mm)	M_r (kN-m)
1	28.61	650	200	0.00818	22.9	33.6
2	31.75	650	0	0.00695	13.7	22.9
3	30.13	344	200	0.01101	19.4	26.3
4	30.16	163	200	0.01219	15.0	17.7
5a	32.07	0	200	N/A	10.4	7.8
5b	30.81	650	200	0.00790	22.7	33.5
6	15.45	650	200	0.00940	23.7	38.4
7	46.54	650	200	0.01079	28.6	42.6
8	29.36	650	400	0.01098	33.0	48.3

$\sigma_{y\text{-}10M}$ = 434 MPa

$\sigma_{y\text{-}15M}$ = 441 MPa

E_{GFRP} = 27521 MPa

f'_m = 10 MPa

Table 5.3 Ratio of Test to Predicted Values for Moment and Deflection

	Moment			Deflection				
Wall	Test (kN-m)	Predicted (kN-m)	$^{Test}/_{Predicted}$	Test (East) (mm)	Test (West) (mm)	Test (Maximum) (mm)	Predicted (mm)	$^{Test}/_{Predicted}$
1	37.57	33.6	**1.12**	93.9	98.9	98.9	93.2	**1.06**
2	25.5	22.9	**1.11**	70.5	82.3	82.3	88.4	**0.93**
3	26.5	26.3	**1.01**	101.3	122.2	122.2	111.5	**1.10**
4	19.7	17.6	**1.12**	86.6	137.0	137.0	120.4	**1.14**
5a	10.8	7.8	**1.38**	56.5	58.9	** 58.9 **	41.0	**1.44**
5b	34.6	32.7	**1.06**	88.3	88.6	88.6	93.1	**0.95**
6	40.9	37.4	**1.09**	113.5	113.3	113.5	93.7	**1.21**
7	46.9	41.2	**1.14**	92.4	118.0	118.0	96.5	**1.22**
8	54.3	48.2	**1.13**	76.5	132.0	132.0	99.2	**1.33**

**Note: Wall 5a was not tested to ultimate failure

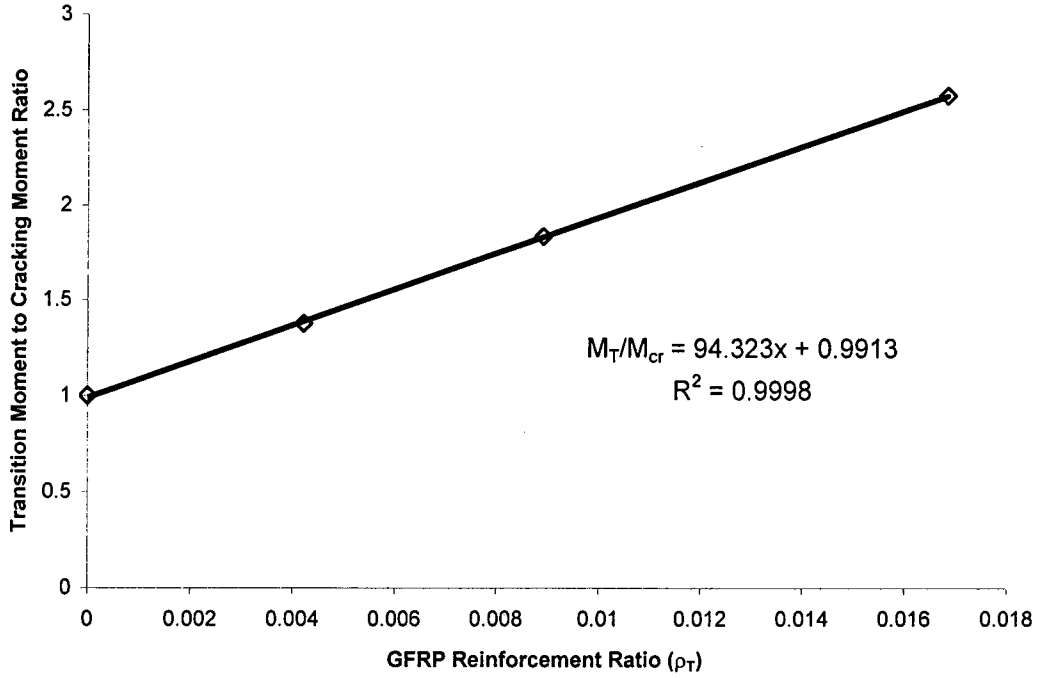

Figure 5.1 Regression Analysis for Transition Moment

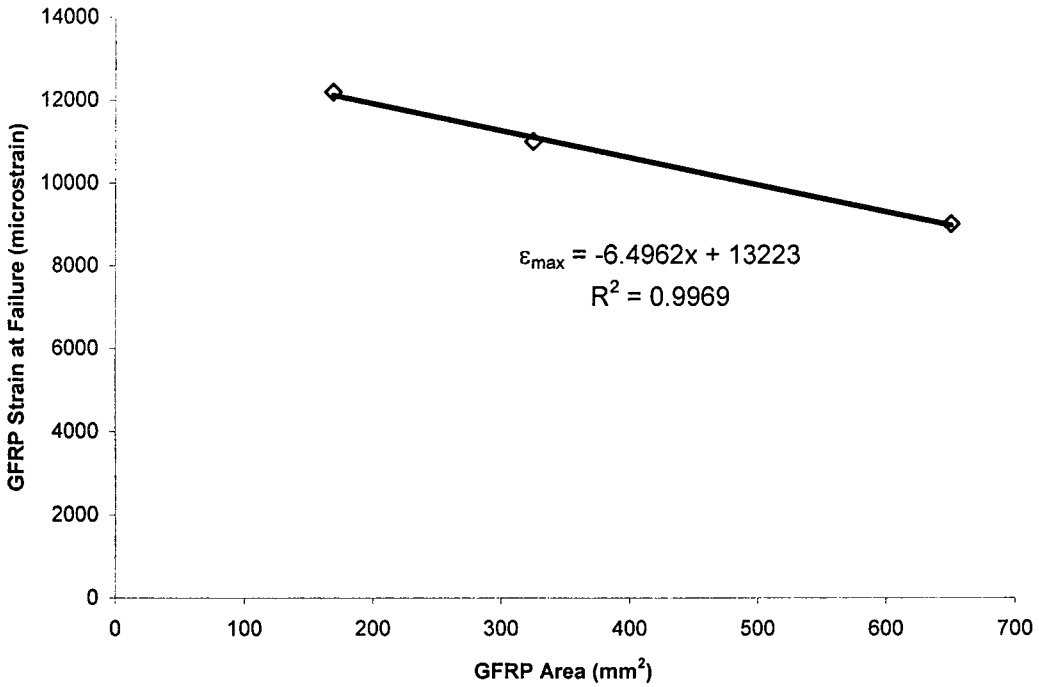

Figure 5.2 Failure Regression Analysis for Maximum GFRP Strain

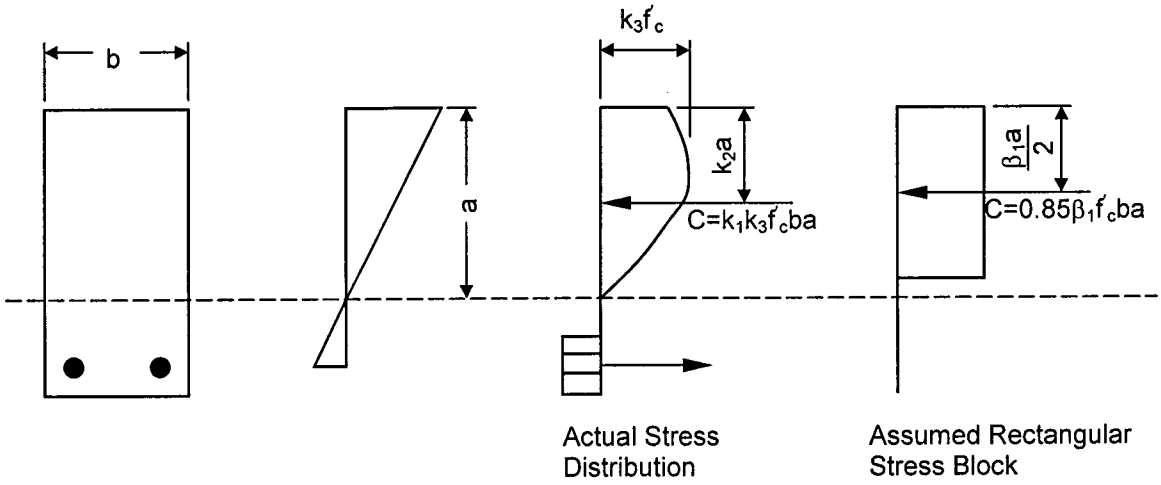

Figure 5.3 Concrete Stress Block at Ultimate Load

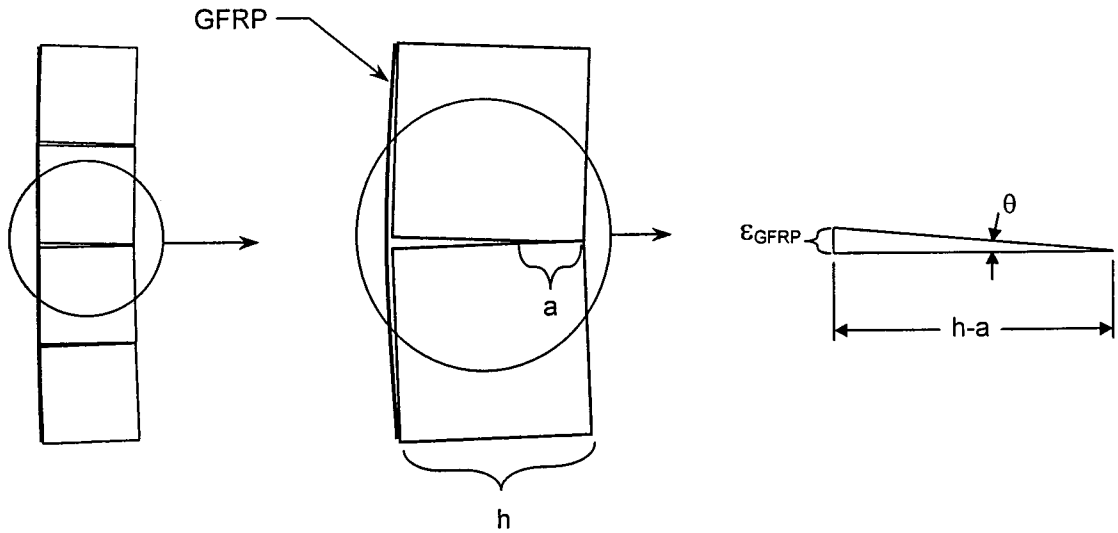

Figure 5.4 Geometric Components of Ultimate Curvature

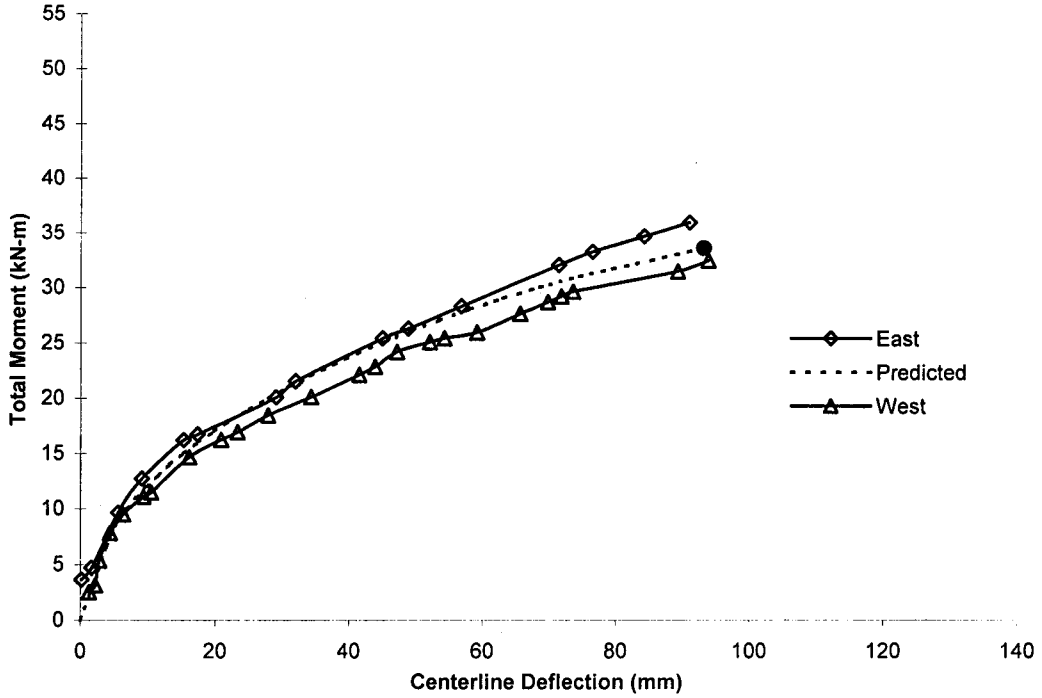

Figure 5.5 Wall 1 Moment versus Deflection: Predicted and Actual

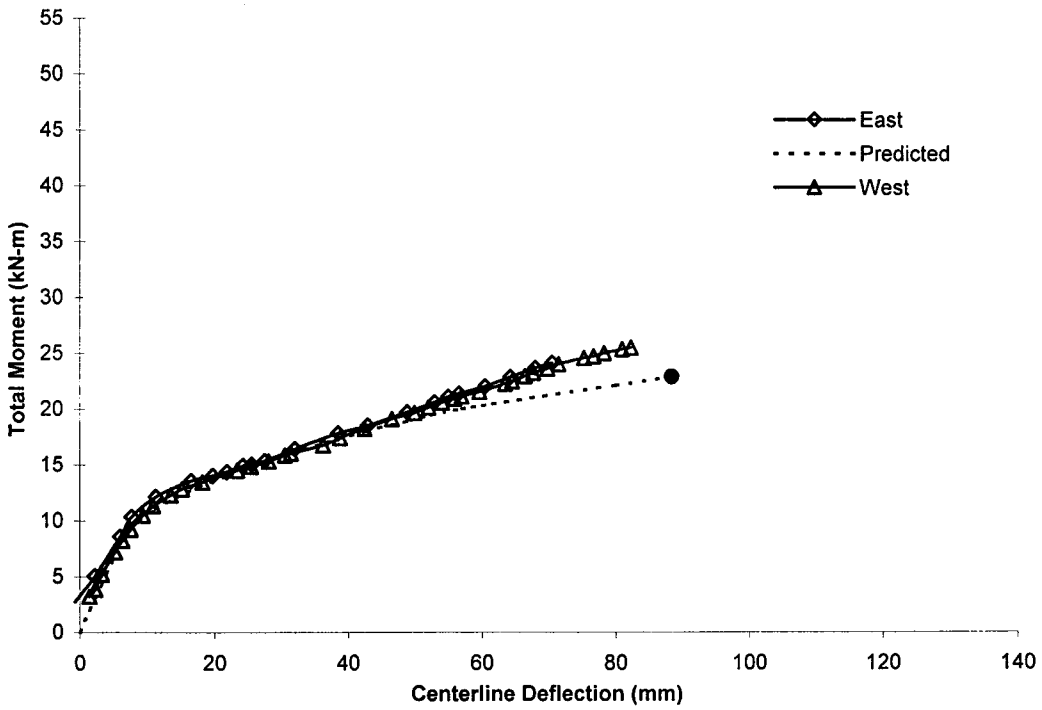

Figure 5.6 Wall 2 Moment versus Deflection: Predicted and Actual

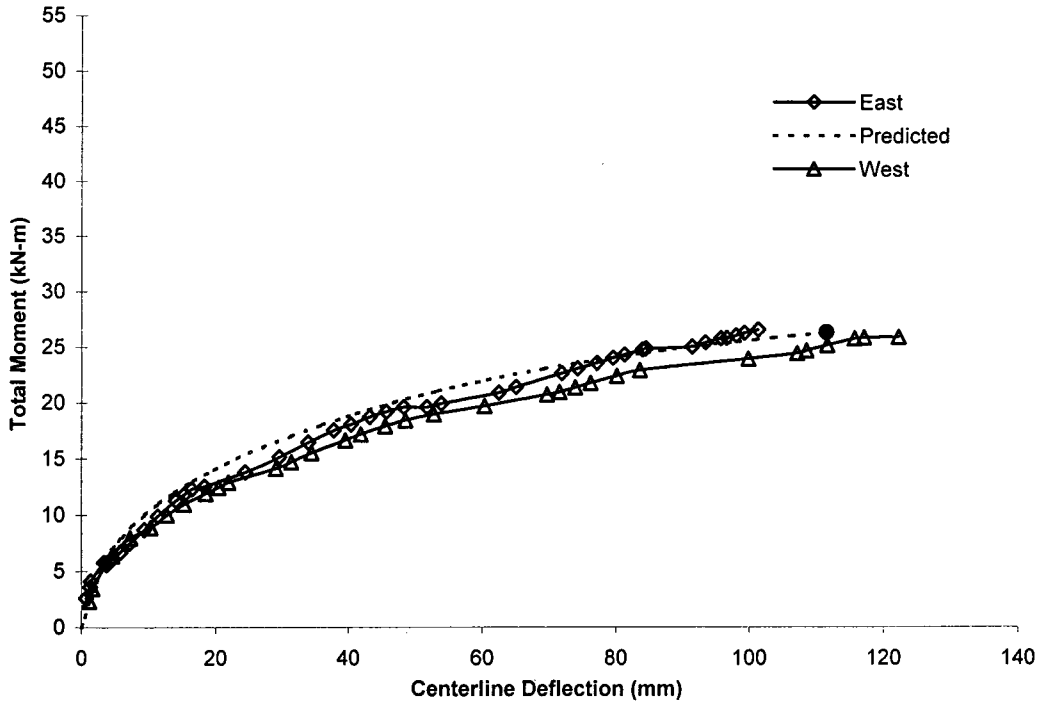

Figure 5.7 Wall 3 Moment versus Deflection: Predicted and Actual

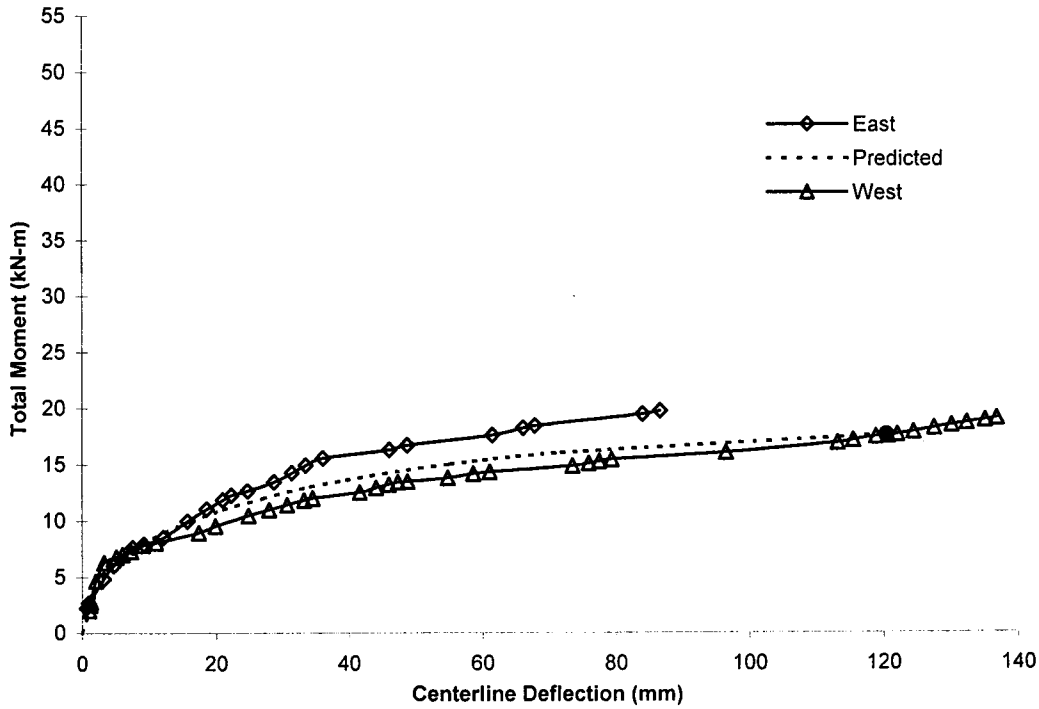

Figure 5.8 Wall 4 Moment versus Deflection: Predicted and Actual

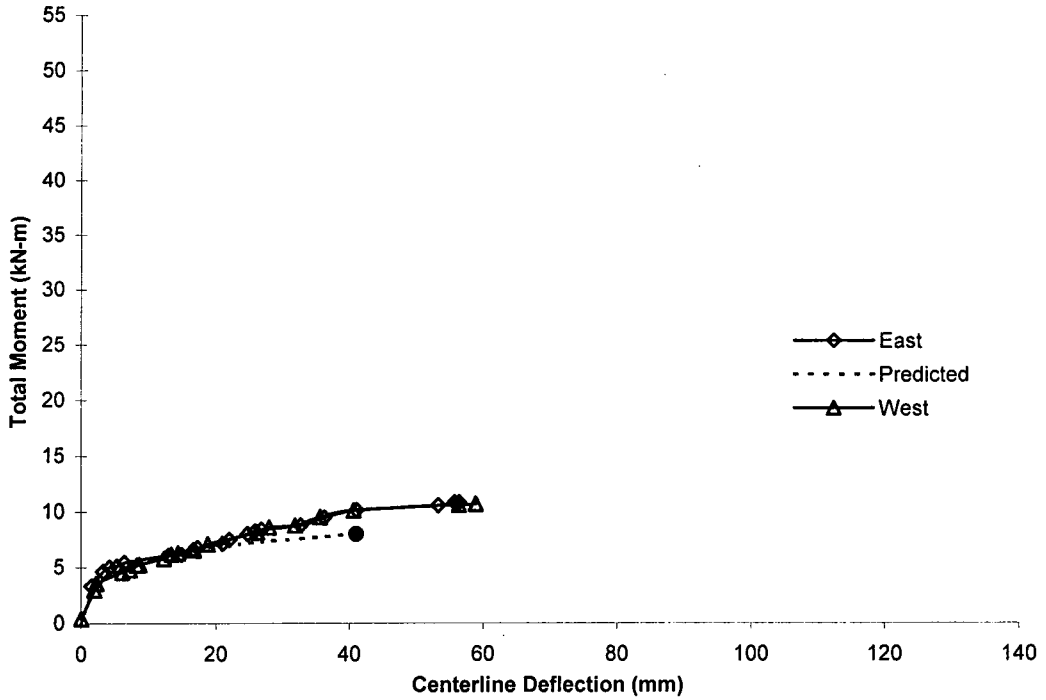

Figure 5.9 Wall 5a Moment versus Deflection: Predicted and Actual

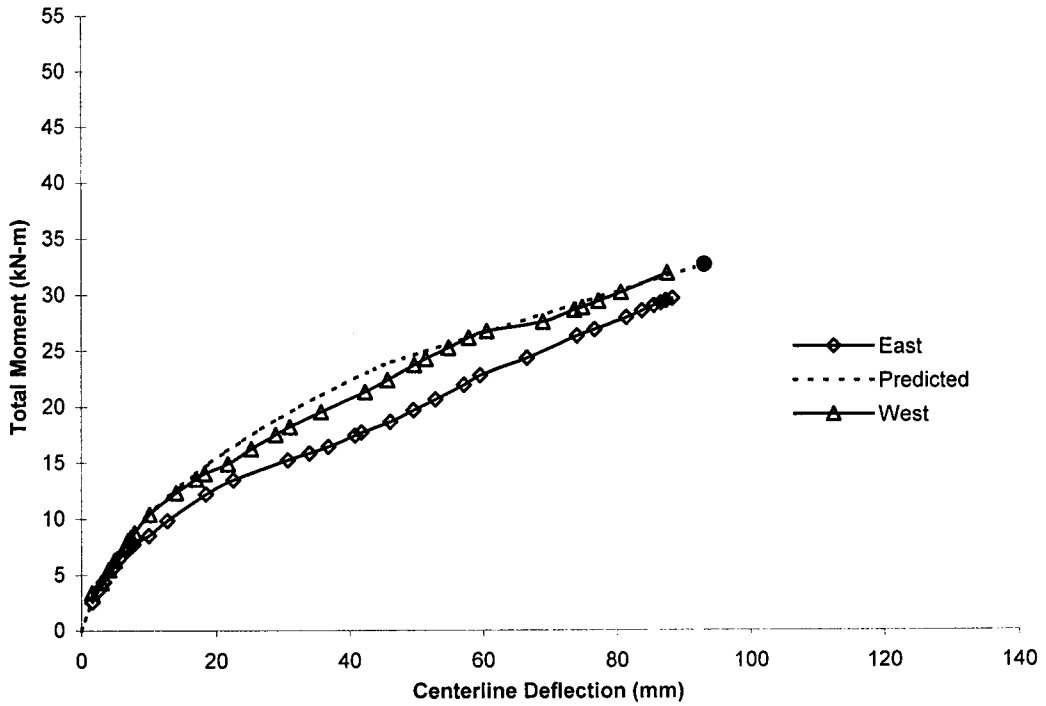

Figure 5.10 Wall 5b Moment versus Deflection: Predicted and Actual

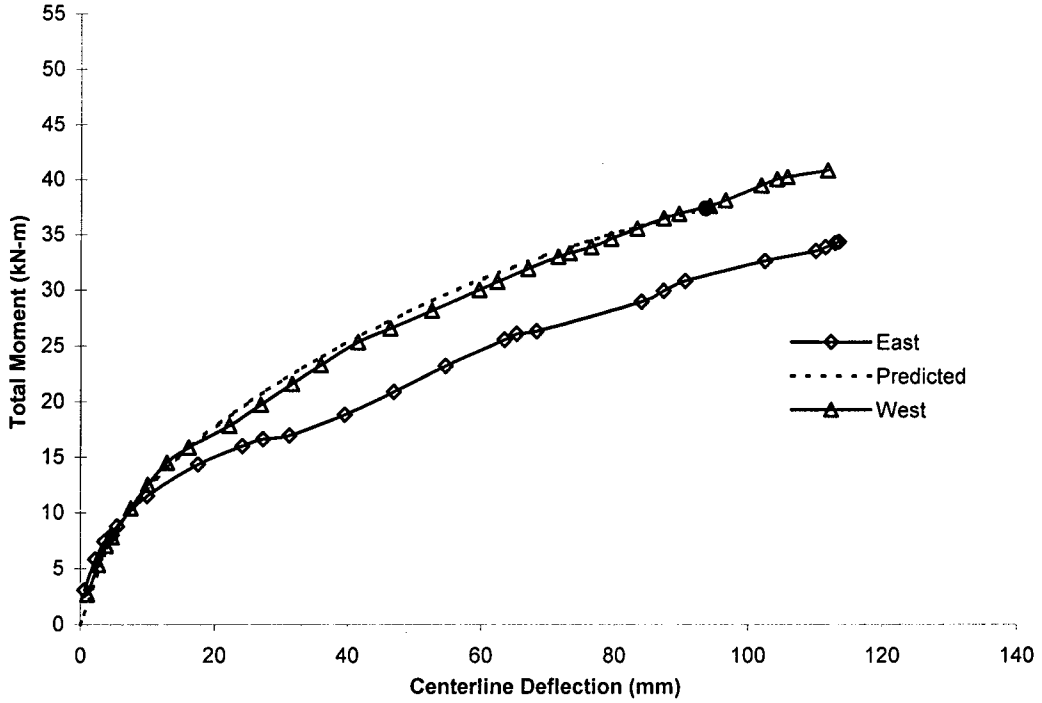

Figure 5.11 Wall 6 Moment versus Deflection: Predicted and Actual

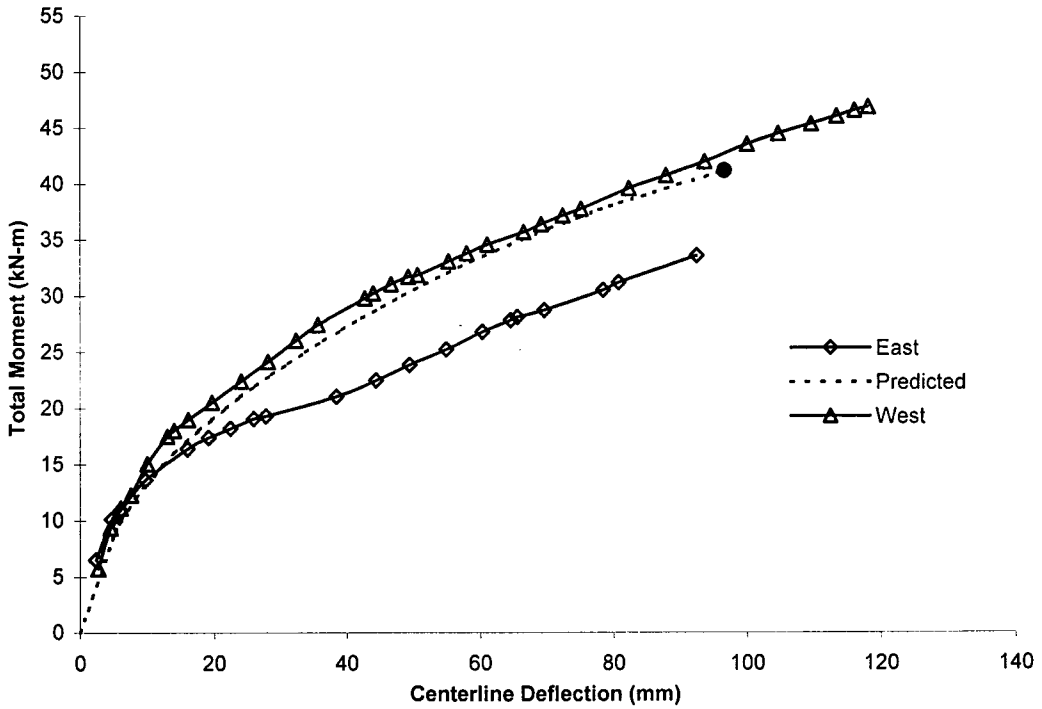

Figure 5.12 Wall 7 Moment versus Deflection: Predicted and Actual

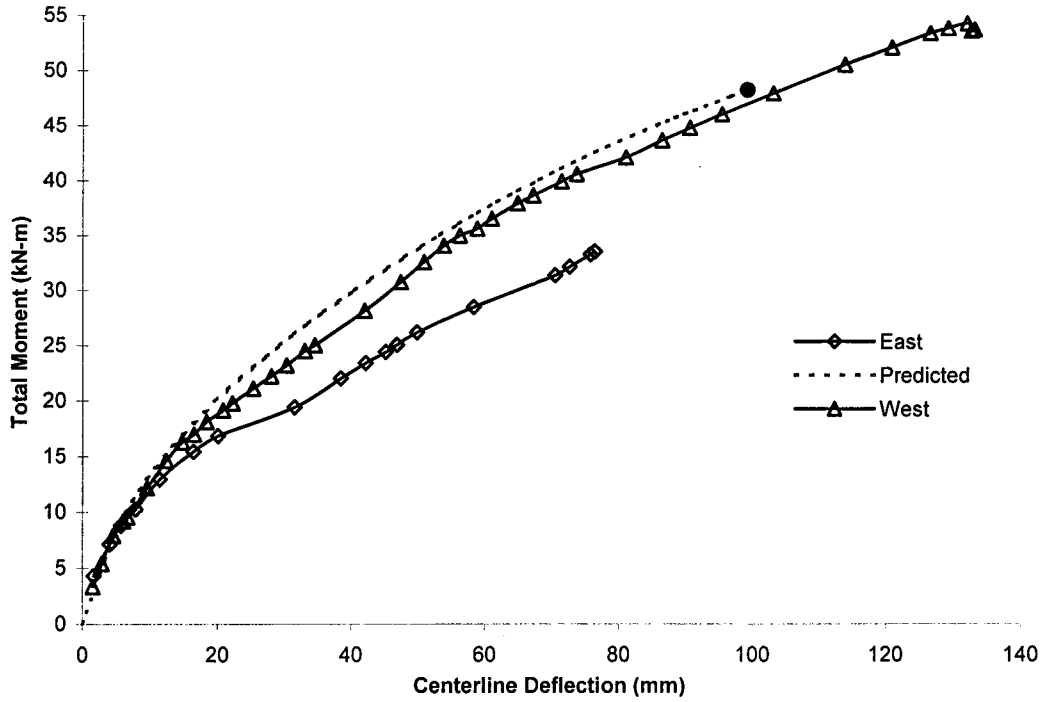

Figure 5.13 Wall 8 Moment versus Deflection: Predicted and Actual

6. SUMMARY, CONCLUSIONS AND RECOMMENDATIONS

6.1 Summary

The objective of this research was to study the out-of-plane behavior of masonry walls reinforced externally with GFRP. A load frame was built to provide both compressive axial loading and fully reversed, lateral cyclic loading. A full-scale testing program consisting of eight wall specimens was conducted in the I.F. Morrison Structural Engineering Laboratory at the University of Alberta. In total, nine tests were performed in which the effects of three parameter groups were studied. These parameters included: level of compressive axial load, amount of internal steel reinforcement, and amount of externally bonded GFRP.

From the data collected, the hysteretic behavior was analyzed and discussed from both a qualitative and quantitative perspective. Of significance, the strain data from both the GFRP and steel reinforcement was used extensively in assessing the behavior. A stiffness degradation model proposed by Abboud *et al.* (1995) was used as part of the numerical model proposed to predict the bending moment versus centerline deflection hysteresis. This mechanistic model includes the parameters of axial load, masonry properties, steel reinforcement properties, GFRP properties, and considers the limits of bond and development between the GFRP and masonry. From this model, a comparison between the predicted and actual hysteresis envelopes was performed. Finally, the data collected in this research program has expanded the database on the out-of-plane behavior of masonry walls with externally applied FRPs started by Albert *et al.* (1998).

6.2 Conclusions

The overall flexural performance of the masonry walls reinforced externally with GFRP was excellent. Except for visible cracks, the walls maintained their structural integrity throughout the out-of-plane cyclic loading. Quantitatively, the integrity of the GFRP/masonry wall system is maintained as shown through the load versus deflection hysteretic responses. The unloading/reloading paths for successive loading cycles was

similar indicating little degradation. In addition, all the unloading paths passed near the origin resulting in a pinching effect which again indicates little degradation of the wall system. Thus, the general behavior of the walls was very predictable. The system, therefore, could be used to advantageously rehabilitate older masonry structures that are inadequately reinforced to withstand seismic events.

The bending moment versus centerline deflection response was bound by an envelope with three distinct regions. The first region had a linear slope which began at the origin, passed through the point defining the cracking moment (M_{cr}), and terminated at the transition moment (M_T). This slope was determined using an effective stiffness calculated with the masonry modulus of Elasticity (E_m) and the modified gross section moment of inertia (I_g^f). The second region exhibited either a linear or bilinear path to failure. In specimens where the only tension reinforcement consisted of GFRP, this region was linear until failure. Whereas in specimens where both steel reinforcement and GFRP were used to resist the internal tensile forces, this region was bilinear; however, there was very little difference between the two slopes. The third region bound the unloading response which again followed a linear path. This path was simply obtained by connecting the point defining the ultimate moment (M_u) to the origin.

Individual hysteresis loops inscribe the envelope. At any given point on the loading envelope, an unloading path can be defined by simply connecting the said point to the origin. Upon reloading on the following cycle, the slope is equivalent to the slope defined by the previous unloading path.

Of the three parameters studied, varying the amount of GFRP was the only parameter which significantly affected the behavior of the walls. The linear response of the bending moment versus centerline deflection hysteresis was governed solely by the GFRP. Increasing or decreasing the amount of GFRP either increased or decreased both the wall stiffness and ultimate strength respectively.

The degradation in flexural stiffness beyond the transition moment was due to successive cracking within the masonry face shell directly adjacent to the bonded GFRP. This cracking resulted in a gradual longitudinal propagation of strain within the GFRP from the bed joint locations toward the center of the masonry units. The flexural stiffness of the wall specimens continued to reduce until the rate of increase in GFRP strain at the

bed joint and center-of-block locations were equal. The term "GFRP mobilization" was used to describe this phenomenon.

Walls which had internal steel reinforcement as well as GFRP exhibited a slight bilinear response beyond the transition moment. This effect was caused by the yielding of the steel reinforcement.

A rational numerical model was successfully developed to predict the bending moment versus centerline deflection response. Modeling of the strength was developed based on the internal force mechanics of the effective cross section. A curvature approach based on the maximum GFRP strains was developed to predict the ultimate wall deflection and the effective stiffness was modeled using a stiffness degradation model proposed by Abboud *et al.* (1995).

6.3 Recommendations

The use of advanced composite materials in structural engineering is a topic still in its infancy. Though many researchers have published test results of various systems reinforced with FRP, few have proposed quantitative procedures to predict the behavior.

Because the FRP dominates the flexural behavior of the externally reinforced masonry walls, a greater understanding of the interaction between the FRP and masonry is required. Specifically, a detailed study of the GFRP strain history in the region between the bed joints and the center-of-block is required for various widths of FRP strips. This should provide some insight into both the strain profile across the FRP sheet and the rate of strain propagation in the longitudinal direction. From this, a scheme could be proposed to optimize the width of the sheets to apply.

The size effects should also be studied by using both 150 mm and 250 mm masonry units. In reinforced concrete members, the tension steel is placed near the extreme tension face of the member. When these systems are retrofit with FRP, typically only about a 20 percent gain in flexural strength is observed. In masonry, the steel reinforcement is located near the geometric centroid and thus the externally applied FRP influences the behavior more. As the masonry units decrease in size, a reduction in the strength gain should be observed. This follows the logic that as the FRP is located closer

to the steel reinforcement, the FRP will have less influence on the behavior. The opposite should occur for larger masonry units.

Finally, very slender walls should be fit with GFRP and tested under high compressive axial loads applied at various degrees of eccentricity. Increasing the flexural stiffness of these walls should show a significant improvement on the compressive axial load capacity. Typically, inelastic instability, or buckling, is the governing load level which is proportional to the flexural stiffness. Also, the addition of external GFRP sheets should reduce localized inelastic behavior by forcing the wall to behave more like a continuous member rather than one composed of a series of rigid bodies.

REFERENCES

Abboud, B.E., Hamid, A.A., and Harris, H.G. (1996). "Flexural Behavior of Reinforced Concrete Masonry Walls under Out-of-Plane Monotonic Loads," ACI Structural Journal, Vol. 93, No. 3, pp.327-335.

Abboud, B.E., Lu, X., and Becica, I.J. (1995). "Deflection of Reinforced Masonry Wall under Out-of-Plane Loads," Proceedings of the Seventh Canadian Masonry Symposium, McMaster Univerisity, Hamilton, Ontario, Vol. 2, pp. 895-910.

Albert, M.L., Cheng, J.J.R., and Elwi, A.E. (1998). Rehabilitation of Uureinforced Masonry Walls with Externally Applied Fiber Reinforced Polymers, Structural Engineering Report No. 226, Department of Civil & Environmental Engineering, University of Alberta, Edmonton, T6G 2G7.

American Society for Testing and Materials Standard D3039M-95a (1995). "Standard Test Method for Tensile Properties of Polymer Matrix Composite Materials," American Society for Testing and Materials, West Conshohocken, Pennsylvania.

Bernardini, A., Giuffre, A., and Modena, C. (1984). "Reinforced Hollow Clay Brick Masonry Walls under Seismic Actions," Proceeding of the 8th World Conference on Earthquake Engineering, Prentice-Hall, Englewood Cliffs, N.J., Vol. 4, pp. 679-686.

Bizindavyi, L. and Neale, K.W. (1999). "Transfer Lengths and Bond Strengths for Composites Bonded to Concrete," Journal of Composites for Construction, ASCE, *in press*.

Buyukozturk, O. and Hearing, B. (1998). "Failure Behavior of Precracked Concrete Beams Retrofitted with FRP," Journal of Composites for Construction, ASCE, Vol. 2, No. 3, pp. 138-144.

Canadian Standards Association (1994). A23.3-94 Design of Concrete Structures with Explanatory Notes, Canadian Standards Association, Rexdale, Ontario.

Canadian Standards Association (1994). S304.1-94 Masonry Design for Buildings (Limit States Design), Canadian Standards Association, Rexdale, Ontario.

Chaallal, O., Nollet, M.-J., and Perraton, D. (1998). "Strengthening of Reinforced Concrete Beams with Externally Bonded Fibre-reinforced-plastic Plates: Design Guidelines for Shear and Flexure," Canadian Journal of Civil Engineering, Vol. 25, pp. 692-704.

Chajes, M.J., Finch, W.W., Januszka, T.F., Thomson, T.A. Jr. (1996). "Bond and Force Transfer of Composite Material Plates Bonded to Concrete," ACI Structural Journal, Vol. 93, No. 2, pp. 208-217.

Ehsani, M.R. (1995). "Seismic Retrofitting of Concrete and Masonry Structures with Composite Materials: Research and Field Applications," Proceedings of the Third National Concrete and Masonry Engineering Conference, San Francisco, California, June 15-17, pp. 19-31.

Ehsani, M.R. and Saadatmanesh, H. (1996). "Seismic Retrofit of URM Walls with Fiber Composites," TMS Journal, Vol. 14, No. 2, pp. 63-72.

Ehsani, M.R., Saadatmanesh, H., Abdelghany, I.H., and Elkafrawy, W. (1993). "Flexural Behavior of Masonry Walls Strengthened with Composite Fabrics," ACI International Symposium on FRP Reinforcement for Concrete Structures, Vancouver, Canada, ACI SP-138, pp. 497-507.

Hamid, A.A., Abboud, B.E., Farah, M., and Harris, H.G. (1989). "Flexural Behavior of Vertically Spanned Reinforced Concrete Block Masonry Walls," Proceedings of the 5th Canadian Masonry Symposium, June 5-7, University of British Columbia, Vancouver, Vol. 1, pp. 209-218.

Hamid, A.A., Hatem, M.K., Harris, H.G., and Abboud, B.E. (1990). "Hysteretic Response and Ductility of Reinforced Concrete Masonry Walls under Out-of-Plane Loading," Proceedings of the Fifth North American Masonry Conference, University of Illinois at Urbana-Champaign, Vol. I, pp. 397-405.

Hognestad, Eivind, Hanson, and McHenry (1955). "Concrete Stress Distribution in Ultimate Strength Design," Journal of the American Concrete Institute, Vol. 52, pp. 455-479.

Kaar, P.H., Hanson, N.W., and Capell, H.T. (1978). "Stress-Strain Charateristics of High Strength Concrete," Douglas McHenry International Symposium on Concrete and Concrete Structures, ACI Publication SP-55, American Concrete Institute, Detroit, pp. 161-185.

Kaiser, H.P. (1989). Bewehren von Stahlbeton mit kohlenstoffaserverstärkten Epoxidharzen, ETH-Dissertation No. 8918, ETH Zürich, Switzerland.

Kolsch, H. (1998). "Carbon Fiber Cement Matrix (CFCM) Overlay System for Masonry Strengthening," Journal of Composites for Construction, ASCE, Vol. 2, No. 2, pp. 105-109.

Kurtis, K.E. and Dharan, C.K.H. (1997). "Composite Fibers for External Reinforcement of Natural Stone," Journal of Composites for Construction, ASCE, Vol. 1, No. 3, pp. 116-119.

Ladner, M. and Weder, Ch. (1981). Geklebte Bewehrung im Stahlebetonbau, Report No. 206, EMPA Dübendorf, Switzerland.

Meier, U. (1987). "Brückensanierung mit Hochleistungs-Faserverbundwerkstoffen," Material und Technik, Vol. 15, pp. 125-128.

Meier, U. and Kaiser, H. (1991). "Strengthening Structures with CFRP Laminates," Proceedings of the Specialty Conference on Advanced Composite Materials in Civil Engineering, Las Vegas, Nev., January 31 – February 1, S.L. Iyer edition, ASCE, pp. 224-232.

Neale, K.W. (1999). "FRPs for Structural Rehabilitation: A survey of Recent Progress," Progress in Structural Engineering and Materials, *in press*.

Saadatmanesh, H. and Ehsani, M.R. (1991a). "RC Beams Strengthened with GFRP Plates. I: Experimental Study," Journal of Structural Engineering, ASCE, Vol. 117, No. 11, pp. 3417-3433.

Saadatmanesh, H. and Ehsani, M.R. (1991b). "RC Beams Strengthened with FRP Plates. II: Analysis and Parametric Study," Journal of Structural Engineering, ASCE, Vol. 117, No. 11, pp. 3434-3455.

Saiidi, M. (1982). "Hysteresis Models for Reinforced Concrete," Journal of the Structural Division, ASCE, Vol. 108, No. ST5, pp. 1077-1086.

Saiidi, M. and Sozen, M.A. (1979). Simple and Complex Models for Nonlinear Seismic Response of Reinforced Concrete Structures, Structural Research Series No. 465, Department of Civil Engineering, University of Illinois at Urbana, Illinois, 61801.

Schwegler, G. (1994). "Masonry Construction Strengthened with Fiber Composites in Seismically Endangered Zones," 10th European Conference on Earthquake Engineering, Vienna, Austria, pp. 2299-2303.

Seible, F. (1995). "Structural Rehabilitation with Advanced Composites," Proceedings of the IABSE Symposium—Extending the Lifespan of Structures, San Francisco, California, pp. 391-398.

Sharif, A., Al-Sulaimani, G.J., Basunbul, I.A., Baluch, M.H., and Ghaleb, B.N. (1994). "Strengthening of Initially Loaded Reinforced Concrete Beams Using FRP Plates," ACI Structural Journal, Vol. 91, No. 2, pp. 160-168.

Tassios, T. (1984). "Behavior of Walls Including Infilled Frames under Cyclic Loading," Proceedings of the CIB Symposium on Wall Structures, International Center for Building Systems, Research and Development, Warsaw, Poland.

Tomaževič, M. and Lutman, M. (1996). "Seismic Behavior of Masonry Walls: Modeling of Hysteretic Rules," Journal of Structural Engineering, ASCE, Vol. 122, No. 9, pp. 1048-1054.

Triantafillou, T.C. (1998). "Strengthening of Masonry Structures Using Epoxy-Bonded FRP Laminates," Journal of Composites for Construction, ASCE, Vol. 2, No. 2, pp. 96-104.

Uniform Building Code (1985). International Conference of Building Officials, Los Angeles, California.

Uniform Building Code (1958). International Conference of Building Officials, Los Angeles, California, Table No. 24-H.

Wakabayashi, M. and Nakamura, T. (1984). "Reinforcing Principle and Seismic Resistance of Brick Masonry Walls," Proceedings of the 8th World Conference on Earthquake Engineering, Prentice-Hall, Englewood Cliffs, N.J., Vol.5, pp. 661-667.

Appendix A

Polynomial Least Squares Fitting

Polynomial Least Squares Fitting

(Example: Fitting a parabola to 5 data points)

The function for the curvature is determined by finding the constants in the equation $f = a+bx+cx^2$. Three linear equations can be used to solve for the constants "a", "b", and "c". The second derivative of the function "f" is M/EI or the curvature. The stiffness can be determined by dividing the bending moment by the second derivative.

Start by defining the matrix "z" determined from the coordinates of the deflected shape within the constant bending moment region.

$$[z_{ij}] = \begin{vmatrix} 0 & 0 \\ 345 & 5 \\ 697 & 8 \\ 1047 & 3.5 \\ 1398 & 0 \end{vmatrix}$$

$$[A] = \begin{vmatrix} (z_{11})^0 & (z_{11})^1 & (z_{11})^2 \\ (z_{21})^0 & (z_{21})^1 & (z_{21})^2 \\ (z_{31})^0 & (z_{31})^1 & (z_{31})^2 \\ (z_{41})^0 & (z_{41})^1 & (z_{41})^2 \\ (z_{51})^0 & (z_{51})^1 & (z_{51})^2 \end{vmatrix}$$

$$[A] = \begin{vmatrix} 1 & 0 & 0 \\ 1 & 345 & 1.19E+05 \\ 1 & 697 & 4.86E+05 \\ 1 & 1047 & 1.10E+06 \\ 1 & 1398 & 1.95E+06 \end{vmatrix}$$

$$[A]^T = \begin{vmatrix} 1 & 1 & 1 & 1 & 1 \\ 0 & 345 & 697 & 1047 & 1398 \\ 0 & 1.19E+05 & 4.86E+05 & 1.10E+06 & 1.95E+06 \end{vmatrix}$$

$$[A^*] = [A]^T [A] = \begin{vmatrix} 5 & 3.49E+03 & 3.66E+06 \\ 3.49E+03 & 3.66E+06 & 4.26E+09 \\ 3.66E+06 & 4.26E+09 & 5.27E+12 \end{vmatrix}$$

$$[A]^T \{z\} = \begin{vmatrix} 16.5 \\ 1.10E+04 \\ 8.32E+06 \end{vmatrix}$$

Now Solve the system: $[A]^T [A] \{x\} = [A]^T \{z\}$

$$([A]T\ [A])^{-1} = \begin{vmatrix} 8.83E-01 & -2.20E-03 & 1.17E-06 \\ -2.20E-03 & 1.02E-05 & -6.71E-09 \\ 1.17E-06 & -6.71E-09 & 4.80E-12 \end{vmatrix}$$

$$\{x\} = \begin{vmatrix} 1.14E-01 \\ 1.96E-02 \\ -1.43E-05 \end{vmatrix} = \begin{vmatrix} a \\ b \\ c \end{vmatrix}$$

Recent Structural Engineering Reports

Department of Civil and Environmental Engineering

University of Alberta

199. *The Flexural Creep Behavior of OSB Panels Under Various Climatic Conditions* by N. Zhao, J.J. Roger Cheng and L. Bach, June 1994.

200. *High Performance Concrete Under High Sustained Compressive Stresses* by S. Iravani and J.G. MacGregor, June 1994.

201. *Strength and Installation Characteristics of Tension-Control Bolts* by S.T. Undershute and G.L. Kulak, August 1994.

202. *Deformational Behavior of Line Pipe* by M. Mohareb, A.E. Elwi, G.L. Kulak and D.W. Murray, September 1994.

203. *Behaviour of Girth-Welded Line Pipe* by N. Yoosef-Ghodsi, G.L. Kulak and D.W. Murray, September 1994.

204. *Numerical Investigation of Eccentrically Loaded Tied High Strength Concrete Columns* by Jueren Xie, Alaa E. Elwi and James G. MacGregor, October 1994.

205. *Shear Strengthening of Concrete Girders Using Carbon Fibre Reinforced Plastic Sheets* by Efrosini H. Drimoussis and J.J. Roger Cheng, October 1994.

206. *Shrinkage and Flexural Tests of a Full-Scale Composite Truss* by Michael B. Maurer and D.J.Laurie Kennedy, 1994.

207. *Analytical Investigation of the Compressive Behaviour and Strength of Steel Gusset Plate Connections* by Michael C.H. Yam and J.J. Roger Cheng, December 1994.

208. *The Effect of Tension Flange Movement on the Strength of Point Loaded–Beams* by Dean Mullin and J.J. Roger Cheng, January 1995.

209. *Experimental Study of Transversely Loaded Continuous Steel Plates* by Kurt P. Ratzlaff and D.J. Laurie Kennedy, May 1995.

210. *Fatigue Tests of Riveted Bridge Girders* by Daniel Adamson and Geoffrey L. Kulak, July 1995.

211. *Fatigue of Riveted Tension Members* by Jeffrey DiBattista and Geoffrey L. Kulak, November 1995.

212. *Behaviour of Masonry Cavity Walls Subjected to Vertical Eccentric Loads* by Ru Wang, Alaa E. Elwi, Michael A. Hatzinikolas and Joseph Warwaruk, February 1996.

213. *Thermal Ice Loads on Structure* by Azita Azarnejan and Terry M. Hrudey, November 1996.

214. *Transmission of High Strength Concrete Column Loads Through Concrete Slabs* by Carlos E. Ospina and Scott D.B. Alexander, January 1997.

215. *Seismic Behaviour of Steel Plate Shear Walls* by Robert G. Driver, Geoffrey L. Kulak, D.J.Laurie Kennedy and Alaa E. Elwi, February 1997.

216. *Extended End Plate Moment Connections under Cyclic Loading* by Bryan T. Adey, Gilbert Y. Grondin and J.J. Roger Cheng, June 1997.

217. *Connection of Infill Panels in Steel Plate Shear Walls* by Ann S. Schumacher, Gilbert Y. Grondin and Geoffrey L. Kulak, August 1997.

218. *Shear Rehabilitation of G-Girder Bridges using CFRP Sheets* by John G.S. Alexander and J.J. Roger Cheng, October 1997.

219. *Seismic Evaluation of Steel Buildings with Concentrically Braced Frames* by Manoj S. Medhekar and D.J. Laurie Kennedy, October 1997.

220. *Rational Design of Prestressed and Reinforced Concrete Tanks* by Abdelaziz A. Rashed, David M. Rogowsky and Alaa E. Elwi, December 1997.

221. *Repair of Cracked Steel Elements using Composite Fibre Patching* by Gaylene D. Kennedy and J.J. Roger Cheng, May 1998.

222. *Strength of Joints that Combine Bolts and Welds* by Thomas J. Manuel and Geoffrey L. Kulak, July *1998.*

223. *Strip Model for Capacity of Slab-Column Connections* by Shahab Afhami, Scott D.B. Alexander, and Sidney H. Simmonds, August 1998.

224. *Behaviour of Large Diameter Line Pipe under Combined Loading* by Patrick R. DelCol, Gilbert Y. Grondin, J.J. Roger Cheng and David W. Murray, September 1998.

225. *An Analysis of the Cyclic Behaviour of Steel Gusset Plate Connections* by Scott S. Walbridge, Gilbert Y. Grondin, and J.J. Roger Cheng, September 1998.

226. *Rehabilitation of Unreinforced Masonry Walls with Externally Applied Fiber Reinforced Polymers* by Michael L. Albert, J.J. Roger Cheng, and A.E. Elwi, October, 1998.

227. *Fatigue of Bearing-Type Shear Splices* by Georg Josi, G.Y. Grondin, and G.L. Kulak, April, 1999.

228. *Out-of-Plane Cyclic Behavior of Masonry Walls Reinforced Externally with GFRP* by Marc D. Kuzik, A.E. Elwi, and J.J. Roger Cheng, September 1999.